Doctoral Dissertation

Studies on Functional Films Using Biodegradable Poly(ethylene glycol)-Poly(L-lactide) Multiblock Copolymer

生分解性ポリエチレングリコール-ポリ(L-ラクチド)マルチブロック共重合体を用いた機能性フィルムに関する研究

Manjie He

July 2024

Graduate School of Engineering,

Osaka University

Contents

General Introduction

Background

Technological advancements have significantly improved human living standards, leading to diverse lifestyles. Various complex and multifunctional materials have been produced and utilized to meet the growing population and rising consumer demands. Thermoplastics, such as polyethylene (PE), polypropylene (PP), and polyvinyl chloride (PVC), have emerged as highly valuable materials due to their ease of processing, lightweight, and low cost. These commodity plastics are extensively used in various applications, from everyday household items to advanced industrial purposes, for example, food packaging, medical supplies, and construction materials, greatly enhancing the convenience and efficiency of modern life [1]. However, most of these materials are derived from non-renewable fossil resources, causing the depletion of limited reserves and substantial environmental consequences such as greenhouse gas emissions, habitat destruction, and pollution. Moreover, many of these materials are difficult to decompose after their utility ends, leading to waste accumulation in landfills and natural surroundings, which poses a serious threat to global ecosystems. Therefore, there is a pressing necessity to innovate and produce eco-friendly materials to replace conventional non-degradable materials. We must focus on biodegradability, renewable resources, and minimizing end-of-life environmental impact in designing these sustainable alternatives. By integrating the principles of green chemistry and the circular economy, we can create materials that meet functional requirements and promote environmental sustainability. (**Fig. 1**) [2].

Fig. 1. Schematic representation of the Reduce, Reuse and Recycle for sustainable development.

Bioplastics, derived from biomass, offer potential in various applications. The prefix “bio” signifies their carbon source or biodegradability [3]. Bioplastic monomers or polymers typically originate from renewable and biological sources and undergo either chemical polymerization or physical combination. While initially designed to be fully biodegradable and compostable,

plastics can also be produced from renewable resources or biomass, known as bio-based plastics. These bio-based plastics may not necessarily be more sustainable or biodegradable than fossil-based plastics and pose similar environmental risks. Examples include bio-PE, bio-PP, bio-PA (polyamide), and bio-PET (polyethylene terephthalate), which are not biodegradable. Specific classifications of polymers are present in **Fig. 2** [4,5].

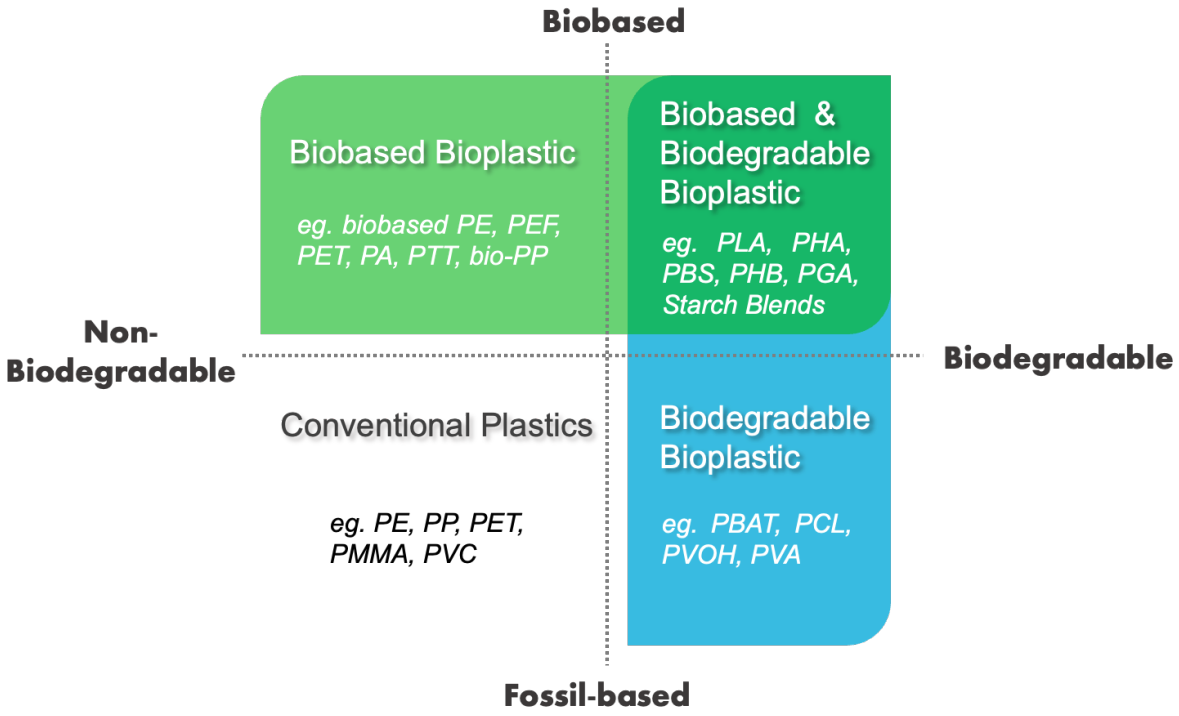

Fig. 2. Classification of polymers based on their bio-based or fossil-based origin and their biodegradability or non-biodegradability in environments such as compost, soil, and aquatic media.

Biodegradable polymers

Biodegradable polymer materials, with their unique advantages of renewability and recyclability, are considered ideal solutions to current environmental problems. Additionally, biodegradable polymers can further enhance their properties through molecular design, integrating intelligent functions to meet the needs of various special application situations, including agriculture, pharmaceuticals, biomedicine, and environmentally friendly fields [6]. Most commercially available biodegradable polymer materials are currently based on aliphatic polyesters. These materials are considered either biomass-based, such as poly(lactic acid)/poly(lactide) (PLA) [7], poly(hydroxyalkanoates) (PHAs) [8], and bio-based poly(butylene

succinate) (bio-PBS) [9]; or fossil-based, which includes polypropylene carbonate (PPC) [10], polybutylene adipate terephthalate (PBAT) [11], polyvinyl alcohol (PVA) [12], and polycaprolactone (PCL) [13]. When biodegraded by microorganisms, these materials can naturally decompose into environmentally acceptable substances such as water, carbon dioxide (CO_2), methane (CH_4), etc., achieving carbon neutrality, as depicted in **Fig. 3**.

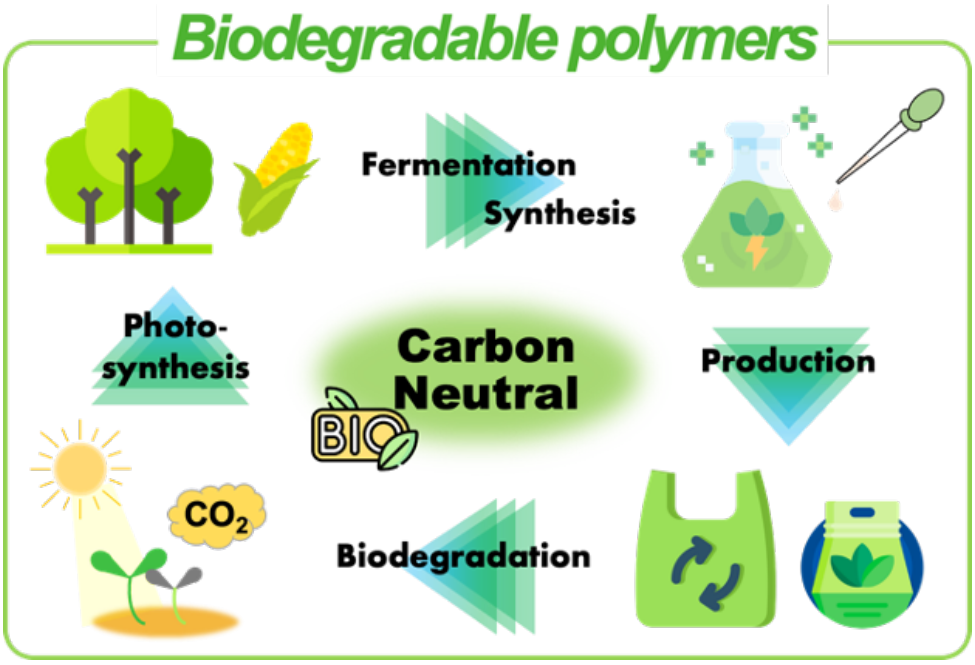

Fig. 3. The circular plastic economy based on biodegradable polymers.

PLA is a linear thermoplastic aliphatic polyester known for its excellent biodegradability, biocompatibility, high strength, and non-toxicity. These properties render it highly promising for various applications in packaging, textiles, electronics, biomedicine, construction, and automotive industries. The European Bioplastics Association reported that global PLA production capacity reached approximately 0.68 MT in 2023, nearly 31% of the total bioplastics production capacity. The PLA capacity is projected to increase to around 3.24 MT by 2028, accounting for over 43.6% of the total bioplastics production capacity. PLA has been acclaimed as the "polymer of the 21st century" due to its exceptional performance in various applications [14].

Lactic acid is a chiral molecule with a central carbon atom bonded to four different functional groups, leading to optical activity. It exists in two enantiomeric forms: L-lactic acid, D-lactic acid, and meso-lactide (**Fig. 4**). PLA derived from these lactides demonstrates three

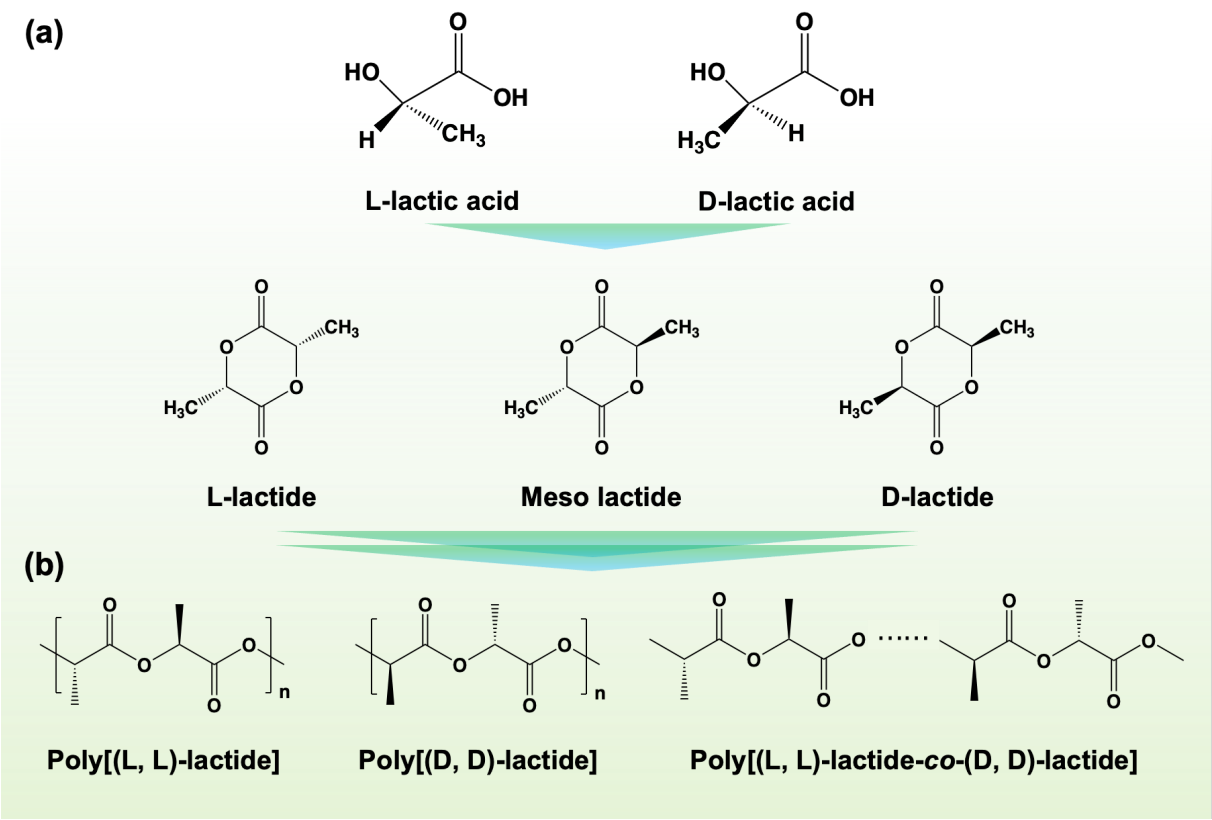

Fig. 4. (a) Stereochemical structures of lactides. (b) Chemical formulae of polylactides.

stereochemical configurations: poly(L-lactide) (PLLA), poly(D-lactide) (PDLA), and poly(D, L-lactide) (PDLLA) [15]. PLLA, produced from L-lactide, exhibits a melting temperature (T_m) of 207 °C and a glass transition temperature (T_g) of around 60 °C [16]. PDLA, synthesized from D-lactide, can create a stereocomplex with PLLA, resulting in a material with a higher melting point. Introducing stereochemical defects (D-lactide or meso-lactide) during PLLA polymerization reduces the T_m, crystallization rate, and crystallinity of the target PLA product [17]. When meso-lactide content reaches 15%, PLA loses its ability to crystallize. The optimal crystallization temperature range for PLA is 105–115 °C [18,19].

The biodegradability and biocompatibility of PLA have contributed to its increasing popularity. These attributes allow PLA to degrade naturally, reducing environmental impact and promoting sustainable development. Additionally, its biocompatibility makes PLA suitable for a range of medical applications, including sutures, implants, and drug delivery systems. Furthermore, its excellent physical properties make it versatile for various applications. In terms of mechanical properties, PLA shares similarities with polystyrene, exhibiting high strength and modulus but low toughness [20]. The properties of PLA largely depend on its crystallinity

behavior. Due to its slow crystallization rate, most PLA products have low crystallinity and limited heat resistance, with a heat distortion temperature of around 60 °C, close to its T_g. This results in poor impact resistance and flexibility, restricting its use in applications that require durable and flexible materials [19,21]. Enhancing the toughness of PLA toughness includes physical blending with flexible polymers and chemical modification.

Polyethylene glycol (PEG) has been extensively studied and developed, particularly in the biomedical field, due to its unique properties that vary with molecular weight (M_n). PEG exhibits excellent flexibility, hydrophilicity, and biocompatibility [22], making it an ideal candidate for enhancing the properties of PLA-based systems. The flexibility and hydrophilicity of PEG play a crucial role in improving the mechanical and physical properties of PLA. By incorporating PEG, the inherent brittleness of PLA can be reduced, resulting in a material with enhanced flexibility and toughness, essential for applications requiring resistance to mechanical stress and deformation [23]. Additionally, the PEG's versatility can be used in modifying PLA developing and expanding advanced functional materials. For example, PEG can introduce other functionalities, such as stimuli-responsive behavior, by incorporating responsive segments into the copolymer. This capability creates opportunities for designing innovative materials that respond to environmental changes, such as temperature, pH, or specific biomolecules [24].

Block copolymers

Block copolymers (BCPs), composed of two or more monomers linked in a specific sequence through covalent bonds, are important materials. They possess the ability to adjust morphology and properties by varying molecular weight, composition, and block sequence. The chain structure and morphology of block copolymers significantly influence their mechanical properties. Due to their inherent asymmetry, flexibility, and tunable interaction potentials, BCPs exhibit unique self-assembly behaviors [25]. This self-assembly capability allows for the formation of well-defined nanostructures, generating substantial interest in nanotechnology. Such a characteristic serves as a valuable tool for producing advanced materials, rendering linear multiblock copolymers highly beneficial across various fields such as electronics, optoelectronics, and catalysis [26–28].

Specialized polymerization techniques, such as ionic polymerization (anionic, cationic, and ring-opening) and controlled radical polymerization methods developed over the past two decades, have become essential for synthesizing monomers in different blocks along the same polymer chain. These techniques, including Atom Transfer Radical Polymerization (ATRP), Reversible Addition-Fragmentation Chain Transfer Polymerization (RAFT), and Nitroxide-Mediated Polymerization (NMP) [29,30], allow for the creation of various structures such as linear diblock, triblock, multiblock, star, and cyclic architectures (**Fig. 5**) [30].

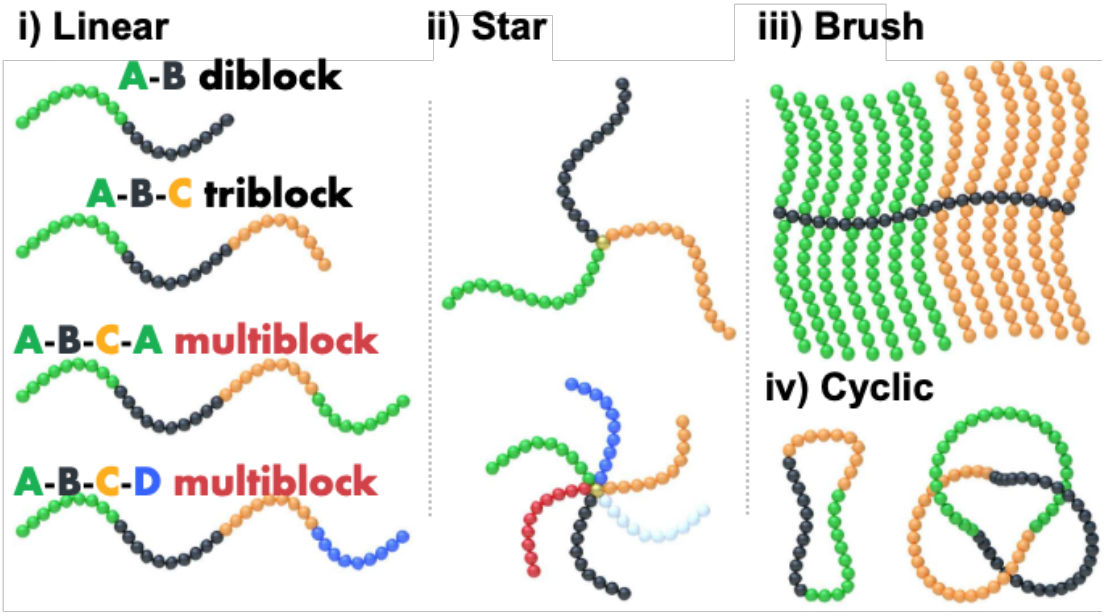

Fig. 5. Schematic representation of polymer architectures: i) linear sequence of diblock, triblock, and multiblock copolymers; ii) star polymers; iii) deblock polymer brushes; iv) cyclic triblock terpolymer and trefoil knot.

Linear multiblock copolymers

Linear multiblock copolymers (LBCPs) have garnered significant research attention due to their tunable physical properties [31]. The thermodynamic incompatibility between different blocks leads to microphase-separated structures (as shown in **Fig. 6**) [32]. By adjusting the composition and structure of these copolymers, their properties can be finely tuned for a wide array of applications [33]. For instance, brittle homopolymers such as PLA can be toughened by copolymerizing with elastic (low T_g) blocks [34]. A key toughening strategy involves the creation

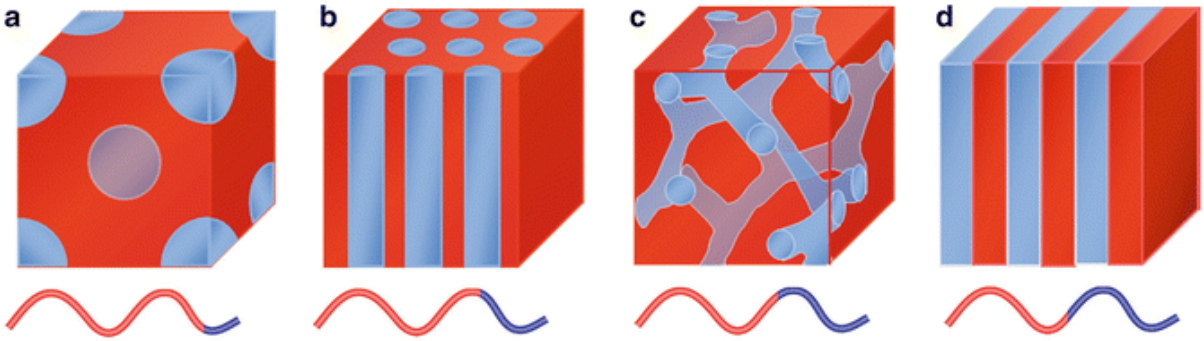

Fig. 6. Morphological transition of AB diblock copolymers with different compositions. (a) Spherical domains with bcc lattice in the matrix, (b) hexagonally packed cylinders in the matrix, (c) double-gyroid network, and (d) alternating lamellar structures.

of linear block copolymers where rubbery middle blocks are sandwiched between two glassy hard blocks. The resulting materials can exhibit either plastic or elastomeric properties depending on the polymer compositions selected to form microphase-separated morphologies. Except for PLA, many other sustainable block copolymers have demonstrated significantly enhanced morphology, thermal properties, and elasticity compared to their original homopolymer counterparts [35].

Precise control of monomer sequences is a fundamental challenge in polymer chemistry and can greatly influence the behavior of polymer materials [36–39]. The synthesis of sequence-controlled LBCPs enables the creation of intricate structures with diverse variations in chain length, composition, and encoded information, which is particularly suitable for high molecular weight polymers. In comparison to random-sequenced LBCPs of the same composition, alternating-sequenced LBCPs exhibit lower glass transition temperatures due to the lack of locally rigid structures, leading to increased flexibility in chain segment movement and impacting the final performance [40]. Therefore, controlling the synthesis sequence of LBCPs is a valuable approach to tailoring their ultimate properties. By incorporating different monomer units into the copolymer, specific functionalities can be achieved, such as responsiveness to stimuli (e.g., temperature, pH, or light), biocompatibility, and degradability, making them promising candidates for applications in drug delivery systems, tissue engineering scaffolds, and medical implants [41,42].

In short, LBCPs represent a versatile and highly tunable class of materials with significant

potential across multiple fields. Their unique self-assembly behavior and customizable properties make them invaluable tools for advancing technology and addressing challenges in electronics, optoelectronics, catalysis, and biomedicine. Continued research and development in this area will undoubtedly lead to further breakthroughs, contributing to innovative materials with enhanced performance and functionality.

Outline of this dissertation

In this dissertation, PLLA and PEG were employed as building blocks to design the multiblock copolymer backbone. Through facile, sequence-controlled, and systematic tailoring of the copolymer segment structure, composition, and topological architecture at the molecular level, the author has precisely tuned various properties, including hydrophilicity, crystallization behavior, biodegradability, mechanical properties, etc. This enables the materials to meet the demands of environments or applications. There are three chapters, each corresponding to the author's published research findings. Each Chapter presents a different set of conditions, demonstrating the potential for tuning the properties of PEG-PLA multiblock copolymers and their wide range of applications.

Chapter 1

In this Chapter, the novel PEG-PLA bioplastics were developed through a facile and low-energy-consuming approach. By sequence-controlling and finely modifying the molecular structure, the yield bioplastic maintains durability in wet environments yet biodegrades rapidly in seawater. This balance is critical to prevent marine pollution post-disposal. Comprehensive characterization was employed to understand their crystallization and mechanical properties and ensure their robust performance, making PEG-PLA an ideal material for packaging, medical, and agricultural uses against marine plastic pollution (**Fig. 7**).

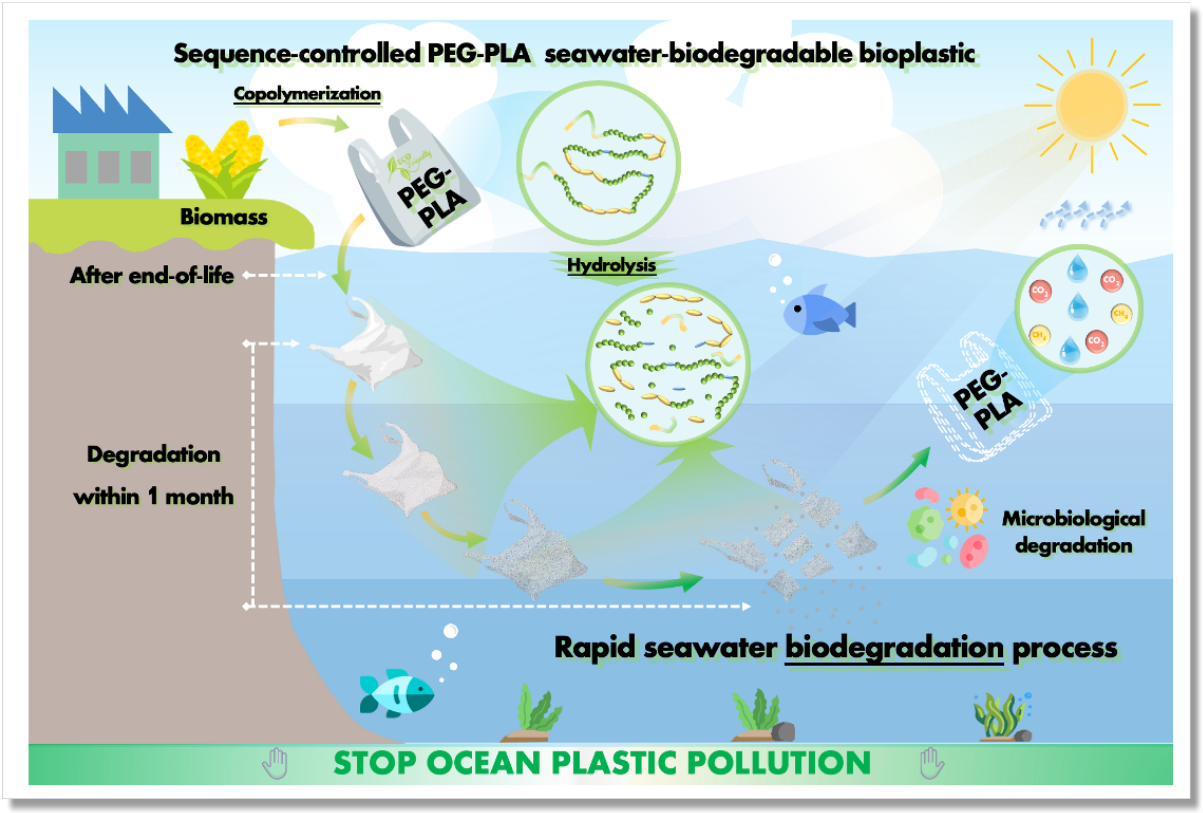

Fig. 7. Graphical abstract of Chapter 1.

Chapter 2

In this Chapter, a biodegradable shape memory PEG-PLA multiblock copolymer stent with precise control over transition temperatures and water was designed, which enables its suitability for in vivo applications. This research introduces an innovative approach that combines shape memory polymers with body temperature- and biofluid-responsive behavior, utilizing the inherent stimuli of human physiological conditions. The PEG-PLA stent exhibits excellent toughness, pH-dependent and gastrointestinal biodegradability, and thermo-/water-triggered dual shape memory effect (SME), offering the potential for localized and sustained drug delivery and addressing inflammation and tumor inhibition (**Fig. 8**).

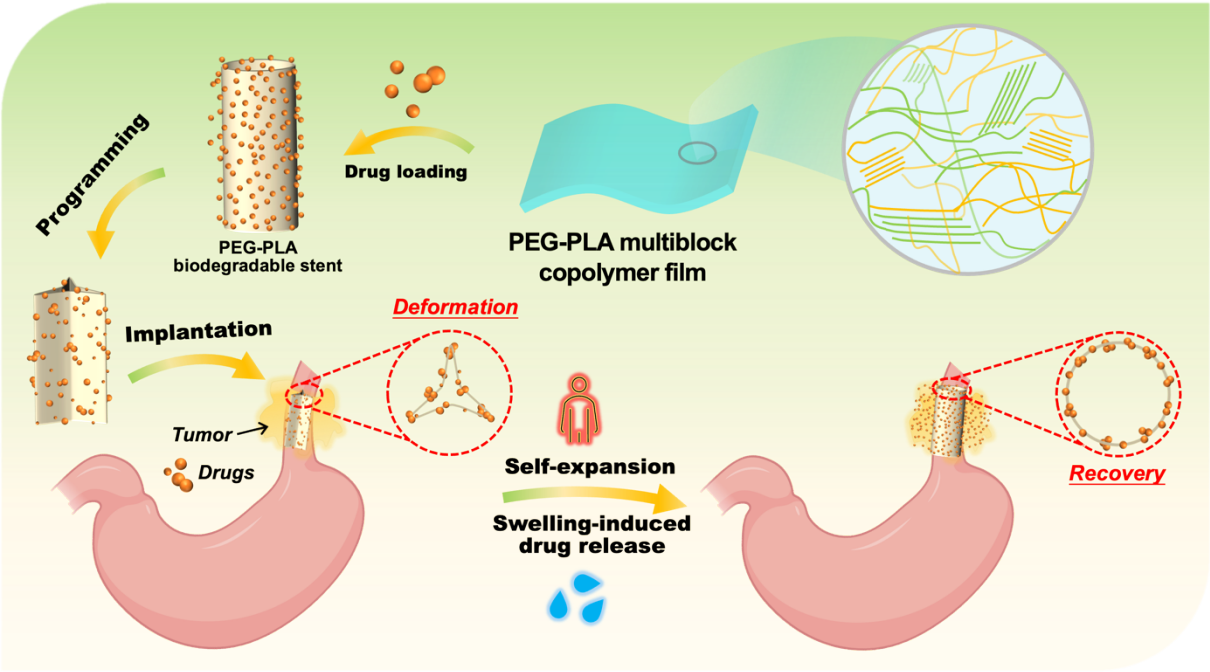

Fig. 8. Graphical abstract of Chapter 2.

Chapter 3

In this Chapter, a novel approach directly blends separate components in different solvents via evaporation-induced co-assembly by introducing water-insoluble PEG-PLA copolymers into CNCs to create a composite film with exceptional toughness and reversible structural color changes. This composite film responds rapidly to environmental humidity and solvent presence, proving ideal for methanol detection sensors. The elaboration of mechanical toughness and the potential for intricate encryption applications suggest a promising avenue for developing green, flexible CNC-based materials for multifaceted optical devices and color sensors. This research contributes a new perspective to the field of biodegradable photonic materials with controllable and multi-responsive structural colors (**Fig. 9**).

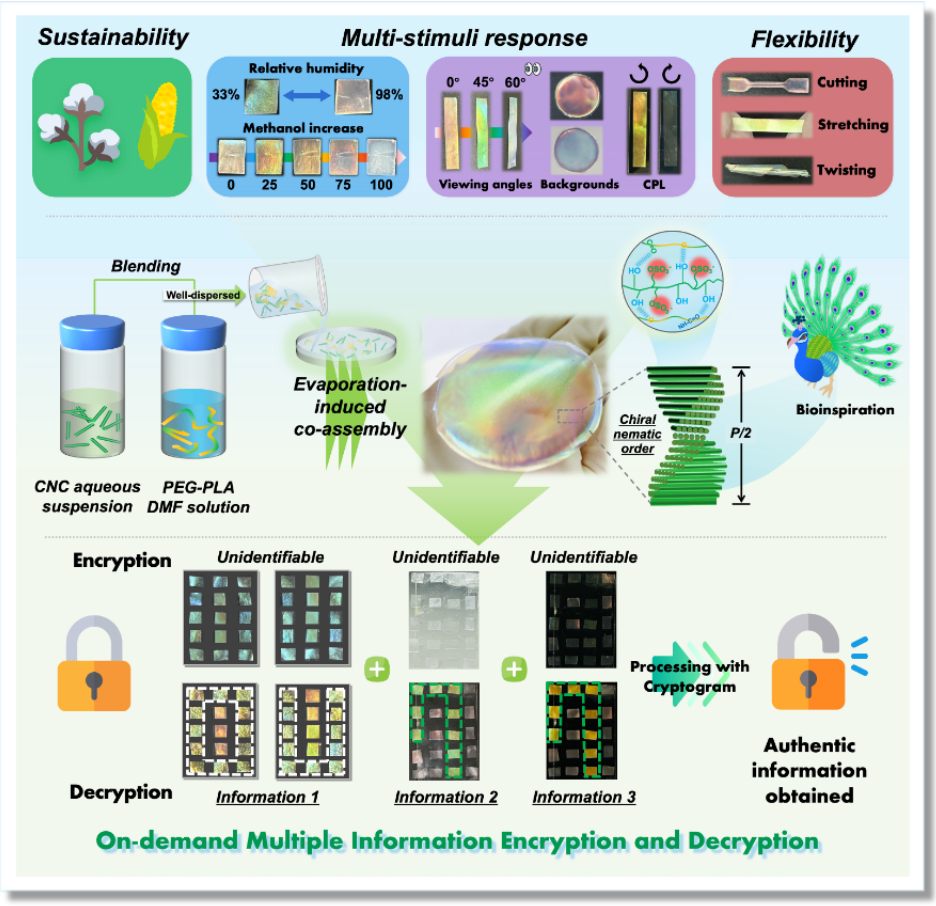

Fig. 9. Graphical abstract of Chapter 3.

References

[1] A. L. Andrady, M. A. Neal, *Philos. Trans. R. Soc. B Biol. Sci.* **2009**, *364*, 1977.

[2] L. Hultman, S. Mazur, C. Ankarcrona, A. Palmqvist, M. Abrahamsson, M. L. Antti, M. Baltzar, L. Bergström, P. de Laval, L. Edman, P. Erhart, L. Kloo, M. W. Lundberg, A. Mikkelsen, E. Moons, C. Persson, H. Rensmo, J. Rosén, C. Rudén, M. Selleby, J.-E. Sundgren, K. Dick Thelander, K. Tybrandt, P. Weihed, X. Zou, M. Åstrand, C. P. Björkman, J. M. Schneider, O. Eriksson, M. Berggren, *Nat. Mater.* **2024**, *23*, 160.

[3] J. G. Rosenboom, R. Langer, G. Traverso, *Nat. Rev. Mater.* **2022**, *7*, 117.

[4] M. H. Rahman, P. R. Bhoi, *J. Clean. Prod.* **2021**, *294*, 126218.

[5] T. D. Moshood, G. Nawanir, F. Mahmud, F. Mohamad, M. H. Ahmad, A. AbdulGhani, *Curr. Res. Green Sustain. Chem.* **2022**, *5*, 100273.

[6] M. S. Kim, H. Chang, L. Zheng, Q. Yan, B. F. Pfleger, J. Klier, K. Nelson, E. L. W. Majumder, G. W. Huber, *Chem. Rev.* **2023**, *123*, 9915.

[7] K. M. Nampoothiri, N. R. Nair, R. P. John, *Bioresou. Technol.* **2010**, *101*, 8493.

[8] S. Chanprateep, *J. Biosci. Bioeng.* **2010**, *110*, 621.

[9] J. Xu, B. H. Guo, *Biotechnol. J.* **2010**, *5*, 1149.

[10] Gerrit. A. Luinstra, E. Borchardt, In *Synthetic Biodegradable Polymers* (Eds.: Rieger, B.; Künkel, A.; Coates, G. W.; Reichardt, R.; Dinjus, E.; Zevaco, T. A.), Springer, Berlin, Heidelberg, **2012**, pp. 29–48.

[11] F. V. Ferreira, L. S. Cividanes, R. F. Gouveia, L. M. F. Lona, *Polym. Eng. Sci.* **2019**, *59*, E7.

[12] E. Chiellini, A. Corti, S. D'Antone, R. Solaro, *Prog. Polym. Sci.* **2003**, *28*, 963.

[13] M. Labet, W. Thielemans, *Chem. Soc. Rev.* **2009**, *38*, 3484.

[14] E. Balla, V. Daniilidis, G. Karlioti, T. Kalamas, M. Stefanidou, N. D. Bikiaris, A. Vlachopoulos, I. Koumentakou, D. N. Bikiaris, *Polymers* **2021**, *13*, 1822.

[15] H. Tsuji, F. Kondoh, *Polym. Degrad. Stab.* **2017**, *141*, 77.

[16] R. Vasanthakumari, A. J. Pennings, *Polymer* **1983**, *24*, 175.

[17] J. Huang, M. S. Lisowski, J. Runt, E. S. Hall, R. T. Kean, N. Buehler, J. S. Lin, *Macromolecules* **1998**, *31*, 2593.

[18] A. Löfgren, A.-C. Albertsson, P. Dubois, R. Jérôme, *J. Macromol. Sci.C* **1995**, *35*, 379.

[19] M. H. Hartmann, In *Biopolymers from Renewable Resources* (Ed.: Kaplan, D. L.), Springer, Berlin, Heidelberg, **1998**, pp. 367–411.

[20] D. Shahdan, N. A. Rosli, R. S. Chen, S. Ahmad, S. Gan, *Int. J. Biol. Macromol.* **2023**, *251*, 126214.

[21] J. O'Loughlin, D. Doherty, B. Herward, C. McGleenan, M. Mahmud, P. Bhagabati, A. N. Boland, B. Freeland, K. D. Rochfort, S. M. Kelleher, S. Fahy, J. Gaughran, *Sustainability* **2023**, *15*, 15312.

[22] A. A. D'souza, R. Shegokar, *Expert Opin. Drug Del.* **2016**, *13*, 1257.

[23] B. Wang, K. Hina, H. Zou, D. Zuo, C. Yi, *J. Vinyl. Addit. Techn.* **2018**, *24*, E154.
[24] S. Uredat, A. Gujare, J. Runge, D. Truzzolillo, J. Oberdisse, T. Hellweg, *Phys. Chem. Chem. Phys.* **2024**, *26*, 2732.
[25] H. Feng, X. Lu, W. Wang, N.-G. Kang, J. W. Mays, *Polymers (Basel)* **2017**, *9*, 494.
[26] Y. Liu, Y. Sun, W. Zhang, *Chinese J. Chem.* **2022**, *40*, 965.
[27] I. I. I. Thomas H. Epps, R. K. O'Reilly, *Chem. Sci.* **2016**, *7*, 1674.
[28] I. Botiz, S. B. Darling, *Mater. Today* **2010**, *13*, 42.
[29] X. Li, J. Iocozzia, Y. Chen, S. Zhao, X. Cui, W. Wang, H. Yu, S. Lin, Z. Lin, *Angew. Chem. Int. Ed.* **2018**, *57*, 2046.
[30] X. Qiang, R. Chakroun, N. Janoszka, A. H. Gröschel, *Isr. J. Chem.* **2019**, 59, 945.
[31] A.-V. Ruzette, L. Leibler, *Nat. Mater.* **2005**, *4*, 19.
[32] Y. Matsushita, In *Encyclopedia of Polymeric Nanomaterials* (Eds.: Kobayashi, S.; Müllen, K.), Springer, Berlin, Heidelberg, **2014**, pp. 1–6.
[33] F. S. Bates, M. A. Hillmyer, T. P. Lodge, C. M. Bates, K. T. Delaney, G. H. Fredrickson, *Science* **2012**, *336*, 434.
[34] A. L. Holmberg, K. H. Reno, R. P. Wool, I. I. I. Thomas H. Epps, *Soft Matter* **2014**, *10*, 7405.
[35] S. U. Tekale, Y. Rottenberg, R. D. Ingle, A. J. Domb, R. P. Pawar, *Polym. Adv. Technol.* **2021**, *32*, 3877.
[36] J. Li, S. N. Rothstein, S. R. Little, H. M. Edenborn, T. Y. Meyer, *J. Am. Chem. Soc.* **2012**, *134*, 16352.
[37] E. C. Davidson, A. M. Rosales, A. L. Patterson, B. Russ, B. Yu, R. N. Zuckermann, R. A. Segalman, *Macromolecules* **2018**, *51*, 2089.
[38] P. R. Judzewitsch, T. K. Nguyen, S. Shanmugam, E. H. H. Wong, C. Boyer, *Angew. Chem. Int. Ed.* **2018**, *57*, 4559.
[39] Y. Kametani, M. Sawamoto, M. Ouchi, *Angew. Chem. Int. Ed.* **2018**, *57*, 10905.
[40] C. C. Huang, M. X. Du, B. Q. Zhang, C. Y. Liu, *Macromolecules* **2022**, *55*, 3189.
[41] A. Rösler, G. W. M. Vandermeulen, H.-A. Klok, *Adv. Drug Deliv. Rev.* **2012**, *64*, 270.
[42] R. K. O'Reilly, C. J. Hawker, K. L. Wooley, *Chem. Soc. Rev.* **2006**, *35*, 1068.

Chapter 1. Superior sequence-controlled poly(L-lactide)-based bioplastic with enhanced seawater biodegradability

1.1 Introduction

Plastic production has surged since 1950 to reach 460 MT, with packaging waste accounting for 1.41 MT in 2019. About 50% of plastics are discarded after a single use, resulting in an annual average of 4.8 to 12.7 MT of plastic waste entering marine ecosystems [1,2]. This has significant implications for human health, as microplastics may accumulate in the human body through the food chain [3–5]. Unless practical innovations in global plastic production and waste management are implemented, approximately 53 MT of marine plastic waste will be generated by 2030 [6,7]. Thus, it is imperative to develop sustainable and marine-biodegradable alternatives [8].

Conventional biodegradable polymers, such as PLA [9,10], have garnered significant attention as biodegradable materials over the past half-century due to their desirable properties, including heat resistance, excellent mechanical strength, and high transparency compared to several common plastics. However, their biodegradation requires specific compost conditions, which means they cannot biodegrade in all natural environments [2]. The degradation rate of these polymers decreases significantly in seawater due to limited marine microbial community and low temperatures [11]. The weight loss of PLA is only approximately 1% after 400 d in seawater [12], attributed to its high T_g [9,13].

Given the presence of complicated and uncontrollable external factors, researchers have focused on the intrinsic degradation factors of polymers in marine environments [14–16]. A practical approach involves blending or copolymerizing hydrophilic materials with biodegradable plastics to achieve higher seawater degradability and avoid the formation of microplastics. Huang et al. [17] enhanced the degradation of PLA in seawater by introducing water-soluble PVA as a filler. Chen et al. utilized the readily degradable property of poly(lactic-co-glycolic acid) (PLGA) to improve the degradation efficiency of PLA in seawater by blending

PLGA with PLA [18]. In these composites, the hydrophilic domains degrade predominantly due to the incorporated material, while the matrix polymer remains stable. In addition, marine degradable polymers can be chemically modified to enhance their hydrolytic or enzymatic degradation rates, affecting their crystallinity and mechanical properties [13,19–21]. Rheinberger et al. introduced hydroxyethoxy side group phosphate esters to serve as "breaking points" in PLA through an RNA-like endoester exchange reaction to improve the degradation of PLA [22]. The integration of hydrophilic aliphatic units proved efficient in enhancing degradability. Polyhydroxyalkanoates (PHAs) are the most well-known marine biodegradable biopolymers, as they can be degraded by many bacteria and fungi, resulting in a relatively fast degradation rate. They are suitable for reducing the long-term impact of marine plastic waste [23]. However, PHAs are typically produced through bacterial fermentation, which leads to high production costs. Low heat distortion temperature and poor gas barrier properties limit their development [24]. Thus, improving the hydrophilicity and enzyme affinity of materials plays a crucial role in their seawater-biodegradability.

PEG is widely used for its hydrophilic, flexible, and biocompatible properties, and it has been approved by the FDA for use in biomedical applications [25]. Wolf et al. demonstrated that the degradation of poly(alkylphosphate) modified with PEG was accelerated under artificial seawater conditions [26]. Therefore, incorporating PEG may generate more potential "breaking points" in the backbone and increase the hydrophilicity of the copolymer, thus leading to a rapid seawater degradation rate. Also, it can help improve the inherent brittleness and low toughness of PLA [27]. Additionally, PEG-PLA amphiphilic block copolymer nanoparticles and multiblock systems have been extensively studied, such as drug carriers in biomedical fields, and have demonstrated their enzymatic biodegradability [28–30]. To the best of our knowledge, there are some studies about new seawater-degradable polymers, but few employ natural seawater for the microorganisms. Importantly, no research utilizes the features of PEG-PLA copolymers for marine biodegradability.

In this chapter, because the degradation of a material often compromises its mechanical properties, the primary goal was to enhance and tunable the biodegradability of PLA in seawater

and maintain their superior toughness even in deionized water. PEG-PLA copolymer bioplastics with sequence-controlled alternating or random structures and PLA homopolymer were synthesized with high yields and purity through a robust ring-opening polymerization (ROP) and coupling process comprising PLA and PEG as building blocks. The effect of the PEG content in the alternating and random molecular chain structures on the hydrophilic, thermal, and mechanical properties of PLA-based bioplastics was investigated. The dynamic degradation behavior of PEG-PLA in Tris-HCl buffer solution, proteinase K solution, and seawater was also carefully explored. A biodegradability of 72.63% was obtained through a quantitative biochemical oxygen demand (BOD) analysis [32]. This confirmed that the PEG incorporated in the PLA backbone accelerated the chain scission of the material in seawater within 28 d for the adjusted and readily biodegradation. The PEG-PLA alternating copolymers showed a balance between performance retention and marine biodegradability in practical applications. The biodegradation prioritized the PLA segments within the PEG-PLA copolymer, as evidenced by structural changes verified through comprehensive characterization techniques. The rapid seawater biodegradation rate and superior mechanical properties of PEG-PLA make it a prime candidate for seawater-biodegradable polymers, providing a new perspective for its use in the packaging, medical, and agricultural industries.

1.2 Experimental Section

1.2.1 Materials

Poly(ethylene glycol) (PEG, M_n = 4000 Da, GR grade), aniline (GR grade), proteinase K, diethyl ether (DE, GR grade), chloroform ($CHCl_3$, GR grade), toluene (super dehydrate, organic synthesis grade), and tin (II) 2-ethylhexanoate ($Sn(Oct)_2$, >95%) were supplied by Wako Pure Chemical Industries (Osaka, Japan). PLA-diol (M_n = 2000 Da, 3000 Da) was purchased from HighChem Co., Ltd. (Tokyo, Japan). 1,6-Hexamethylene diisocyanate (HDI, >98%) was obtained from the Tokyo Chemical Industry Co., Ltd. (Tokyo, Japan). A pH 8.5 buffer solution of 1 mol L^{-1} Tris hydrochloride (Tris-HCl) was provided by Sigma-Aldrich (Massachusetts, U.S.A.). All reagents were used as received unless otherwise stated. $Sn(Oct)_2$ was diluted in

dry toluene and stored in a glass volumetric flask under a nitrogen atmosphere before use. Deionized water (DIW) purified using a Milli-Q system (Millipore Inc., Milford, MA, USA) was used for all experiments.

1.2.2 Synthesis of PEG-PLA multiblock copolymers with alternating and random structures

A series of PEG-PLA alternating multiblock copolymers with various compositions were prepared via a facile bulk polymerization technique (*i.e.*, ROP and coupling process), as shown in **Scheme 1-1a**. Triblock PLA-PEG-PLA-diol prepolymers were synthesized via bulk ROP of L-Lactide with PEG-diol as an initiator. The process involved drying and stirring PEG-diol and L-Lactide, placing them in a three-neck round-bottom flask under vacuum, evacuating and purging with nitrogen, and then heating in an oil bath at 60 °C for 3 h. A toluene solution of

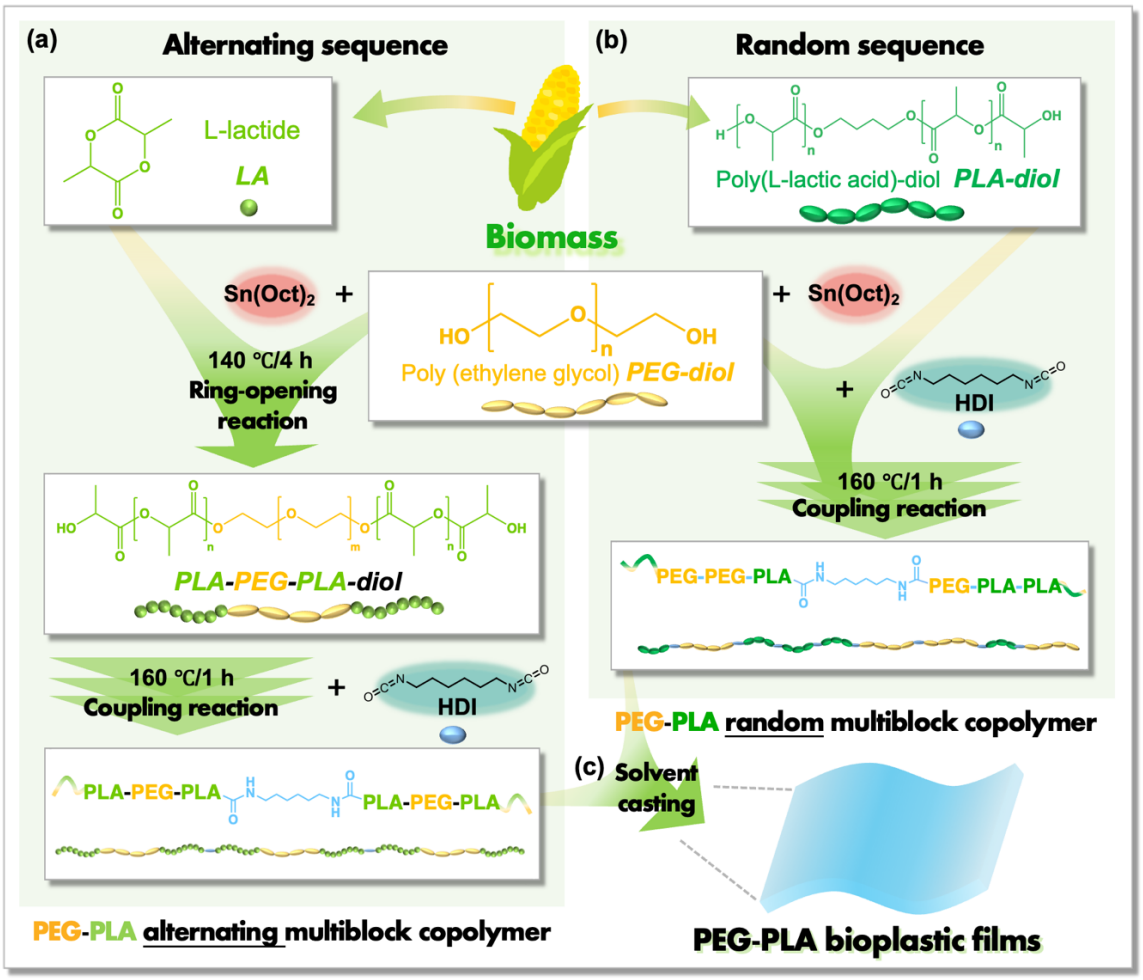

Scheme 1-1. Schematic representation of the synthesis of PEG-PLA (a) alternating and (b) random multiblock copolymers and (c) films created through solvent casting.

$Sn(Oct)_2$ was added, followed by stirring at room temperature and heating to 140 °C in a nitrogen atmosphere for 4 hours. A sample was taken post-copolymerization for conversion determination using ^1H NMR analysis. Subsequently, PEG-PLA alternating multiblock copolymers were created by combining PLA-PEG-PLA-diol with HDI in bulk under a nitrogen atmosphere, maintaining a constant molar ratio of diisocyanate/polyester-diols at 1.2/1. HDI was gradually added into the reactor at 160 °C, followed by intense mechanical stirring for 1 hour to ensure completion of the coupling reaction.

The synthesis procedure for the PEG-PLA random multiblock copolymers is shown in **Scheme 1-1b**. A 200 mL three-necked round-bottom flask was filled with PLA-diol and PEG-diol at a molar ratio of 2:1 under a nitrogen atmosphere. The mixture was stirred for 3 h at ambient temperature under a vacuum of less than 30 Pa to remove water and oxygen. Subsequently, a toluene solution containing $Sn(Oct)_2$ equivalent to the 1 mol% of the PEG-diol component was injected. The resultant system was then stirred under vacuum at ambient temperature for 1 h to ensure complete mixing, followed by heating to 160 °C. A fixed 1:1.2 molar ratio of total PLA-diol to PEG-diol was used, and HDI was added to the reaction system dropwise. Vigorous mechanical stirring was performed for 1 h to confirm that the coupling reaction was completed. Meanwhile, the procedure for the random sequence was also used to synthesize PLA homopolymers.

To purify the PEG-PLA alternating and random multiblock copolymers and PLA homopolymers, the crude products were first dissolved in $CHCl_3$, precipitated by DE, and dried under vacuum for 24 h at ambient temperature to remove residual solvents, and kept well for characterization. The nomenclature for all the synthesized copolymers and homopolymers is given as PEG*x*PLA*y*-*a*/*r*/*h*, where '*x*' and '*y*' represent the M_n of PEG and PLA chain segments, respectively; the suffixes '*a*', '*r*', and '*h*' denote alternating copolymers, random copolymers, and homopolymers, respectively.

1.2.3 Preparation of PEG-PLA multiblock copolymer films

PEG-PLA multiblock copolymer films with thicknesses of 0.3–0.4 mm were fabricated by solvent casting from the purified products in a horizontal Teflon mold using $CHCl_3$. In a fume hood, the solvent was evaporated naturally at ambient temperature for 2–3 d. The obtained films (**Scheme 1-1c**) were moved to an oven at 25 °C for 24 h and sealed for testing.

1.2.4 Water uptake ratio (WUR) of PEG-PLA multiblock copolymer films

The water uptake ratio (WUR) was evaluated using Milli-Q water. Dry film samples (2 × 2 cm) were prepared in quintuplicate, and their initial dry weights (W_d) were recorded. The samples were fully immersed in water at 25 °C. After a predetermined period, the samples were carefully extracted using tweezers. The extra surface water was gently blotted off with tissue paper, and the wet weights of the samples (W_s) were promptly measured. The WUR was calculated based on the initial dry weight of the film samples using **Eq. (1-1)**:

$$\mathbf{WUR\ (\%)} = \frac{W_s - W_d}{W_d} \times 100\% \qquad \mathbf{(1\text{-}1)}$$

Based on **Eq. (1-1)**, the WUR was calculated for the five samples and averaged. This approach ensured quantification of the water durability of materials, facilitating a comparison of the hydrophilic properties of different films.

1.2.5 Degradation of PEG-PLA multiblock copolymer films in different conditions

1.2.5.1 Hydrolytic degradation and enzymatic biodegradation

The degradation of PLA is facilitated by proteinase K [33,34]. Thus, the enzymatic degradation behavior of PEG-PLA films was characterized by proteinase K. The initial weights of the films were recorded (W_0), and the films were then immersed in 25 mL of 0.05 mol L^{-1} Tris-HCl buffer solution (pH 8.5) containing proteinase K. The procedure was carried out over 120 h at 37 °C to evaluate the degradation behavior comprehensively. After incubation, the films were carefully removed from the solution and gently rinsed with DIW to remove any residual enzyme solution. The films were then lyophilized and weighed (W_t). The enzymatic biodegradability of the multiblock copolymers was quantitatively assessed using **Eq. (1-2)**:

$$\textbf{Residue weight (\%)} = \frac{W_t}{W_0} \times 100\% \qquad \textbf{(1-2)}$$

Degradation tests were conducted in quintuplicate to ensure statistical relevance, and the results are presented as mean values.

1.2.5.2 Marine biodegradation in seawater based on BOD analysis

A natural seawater sample was collected near Koshien Hama in Osaka Bay (N34°42′20.36″, E135°21′12.44″) on October 29, 2023; the seawater temperature was 21.7 °C. The water was then transferred to a cleaned 5 L plastic jerry can wrapped in aluminum foil to keep out light and delivered to the Uyama laboratory at the Suita campus of Osaka University within 4 h.

Closed-bottle tests were performed in a temperature-controlled BOD reactor (Velp Scientifica™ RESPIROMETRIC Sensor System 6, Italy) according to the Organization for Economic Cooperation and Development Marine biodegradation test guideline (OECD 306) [35]. This technique quantifies the aerobic biodegradation capability of organic substances by tracking the oxygen uptake of microorganisms at 20 °C in the dark, which was achieved by covering the reactors with aluminum foil for 28 d under constant stirring. Automatic pressure results from conversion in BOD data. The RESPIROMETRIC Sensor transmits data directly to the PC, enabling real-time monitoring of the analysis curve.

Each film sample and an aniline reference (approximately 10 mg each) were weighed (W_0) and placed separately in a 300 mL BOD reactor, and test water (100 mL) was poured into the reactor as an inoculum. Subsequently, mineral supplements of 25 mg NH_4Cl, 5 mg $NaHPO_4$, 0.5 mg N-allylthiourea, and 0.1 mL of a buffer solution were added to the test water. The buffer solution comprised 33.30 g of $NaHPO_4{\cdot}2H_2O$, 21.75 g of K_2HPO_4, 8.50 g of KH_2PO_4, and 0.50 g of NH_4Cl per liter. Then, BOD data were recorded using a computer system at regular intervals (day). The BOD biodegradability of the films was calculated using **Eq. (1-3)** [36]:

$$\textbf{BOD Biodegradability (\%)} = \frac{BOD_t - BOD_b}{ThOD} \times 100\% \qquad \textbf{(1-3)}$$

where BOD_t is the BOD of the test solution, BOD_b is the BOD of the control blank, and *ThOD* represents the theoretical oxygen demand. An organic microelemental analyzer (MT-6, Yanaco Co., Ltd., Kyoto, Japan) was used to determine the C, H, N, and O contents of the samples. The results were then used to calculate the *ThOD*. Two samples were evaluated in each BOD test.

The BOD biodegradability of each sample was calculated by the average of the three results. After incubation for 28 d, the films were carefully removed from the solution and gently washed with DIW to remove residual seawater. The films were then lyophilized and weighed again (W_t). After seawater degradation, the residual weights of the dried samples were calculated using **Eq. (1-2)**. Moreover, the M_n, chemical structure, composition, and thermal properties were evaluated using corresponding methodologies.

1.2.6 Characterization and Measurements

The molecular structure and chemical composition of samples were confirmed by Proton Nuclear Magnetic Resonance Hydrogen Spectrum (^{1}H NMR) using a JNM-ECS400 (400 Hz, JEOL, Japan) spectrometer at room temperature. All samples were dissolved in deuterated chloroform ($CDCl_3$) as an internal reference (δ = 7.26 ppm).

The chemical functional group of samples within the Attenuated Total Reflection Fourier Transform Infrared (ATR-FT-IR) spectrum over a wavenumber range of 4000–500 cm^{-1} was recorded, and each sample was scanned 32 times at RT utilizing a Nicolet iS5 spectrometer (Thermo Fisher Scientific, MA, USA.).

The number of average M_n, weight average molecular weight (M_w), and distribution ($Đ$) of samples were performed by Gel Permeation Chromatography (GPC) using a JASCO (Tokyo, Japan) HLC system (composed of a PU-4180 pump, an AS-4050 auto-sampler, a RI-4030 refractive-index detector, and a CO-4060 column oven) at 40 °C, and a polystyrene standard ($5.89 \times 10^2 - 1.09 \times 10^6$ g mol^{-1}) was used for calibrating the molecular weights. *N*, *N*-Dimethylformamide was used as the eluent at a flowing rate of 0.75 mL min^{-1}, and a sample concentration of 10 mg mL^{-1} and an injection volume of 50 μL were employed.

The light transmittance of the samples was evaluated on a UV–Vis spectrophotometer (U-2810, Hitachi, Tokyo, Japan) and scanned in the range of 400–800 nm.

The thermal transition properties were performed by Differential Scanning Calorimetry (DSC) (DSC200 instrument, Hitachi, Tokyo, Japan) under an N_2 atmosphere at a flow rate of

50 mL min^{-1}, with empty aluminum as the reference. The samples (*ca*. 6 mg) were first heated to 190 °C and kept for 2 min to erase the thermal history. They were subsequently cooled to –80 °C at 10 °C min^{-1} and held for 2 min before being reheated to 190 °C at the same rate. The melting temperature (T_m), crystallization temperature (T_c), glass transition temperature (T_g), and corresponding entropy (ΔH_m or ΔH_c) were recorded.

X-ray Diffraction (XRD) patterns were recorded using a SmartLab (In-plane) (Rigaku Corporation, Japan) with Cu-Kα radiation (λ = 1.541 Å) at RT. The scanning speed was 5° min^{-1} over a 2θ range of 5° to 60°. The generator voltage and current were 45 kV and 200 mA, respectively. The samples were prepared by solvent casting, and each thickness was approximately 0.3–0.4 mm. They were stored for 1 week before the test.

Wide-angle X-ray Scattering (WAXS) measurements were performed at the BL40B2 beamline at the Spring-8 synchrotron radiation facility (Hyogo, Japan), which used a highly monochromatic beam with low divergence and a small cross-section, and 2D images were recorded using the detectors. A flat panel (C9728DK–10; Hamamatsu Photonics KK, Shizuoka, Japan) was used as the WAXS detector. The sample-to-detector lengths of the WAXS profiles were 58.3 mm. The as-prepared sample, the same as XRD, was stored in a sealed bag 1 day before the test.

The crystalline morphology and growth rate of PEG-PLA multiblock copolymers were studied on-site using a Polarized Optical Microscope (POM) (RX-100, Hirox, Tokyo, Japan) with an MHS-2000 hot-stage accessory (Imoto machinery, Kyoto, Japan). To prepare the sample, the copolymer was placed between two glass slides on the hot stage set at 150 °C and then cooled to room temperature to form a thin film for observation. The samples were initially heated to 150 °C and maintained at this temperature for 3 min to ensure complete melting and eliminate any previous thermal effects. Subsequently, rapid cooling was applied to achieve the ideal temperature for observing crystal morphology. By meticulously recording the entire crystallization process, a comprehensive understanding of crystal morphology and growth rates at various temperatures was attained.

The thermal stability and weight fractions of samples were determined by Thermogravimetric Analysis (TGA) with STA 200RV (Hitachi, Tokyo, Japan) in the temperature range of 30–800 °C at a heating rate of 20 °C min^{-1} under N_2 atmosphere at a flow rate of 50 mL min^{-1}.

Dynamic viscoelastic properties were measured using Haake Rheostress 6000 (Thermo Fisher Scientific, MA, USA) with a 20 mm parallel plate geometry. The strain sweep test identified the linear viscoelastic region of samples (0.1–100% oscillatory strain at an angular frequency of 10.0 rad s^{-1}). To analyze storage and loss modulus, 1% oscillatory strain and a frequency range from 0.1 to 100% rad s^{-1} were applied. Time-oscillatory scanning method (20 min) was executed at 1 rad s^{-1} and 1% strain.

Dynamic Mechanical Analysis (DMA) was employed to evaluate the thermo-mechanical properties of the sample with a dynamic mechanical analyzer (DMA 7100, TA Instruments, USA) in a tensile mode. Tests with liquid nitrogen control were performed from –90 °C to 100 °C at a heating ramp of 3 °C min^{-1} and an amplitude of 0.2 % at a frequency of 1 Hz.

The water contact angle (WCA) was obtained on a Drop Master DM300 (Kyowa Interface Science, Japan) with 1.0 μL water drops at room temperature. The results were measured in triplicate to ensure statistical relevance and were presented as mean values.

The mechanical performance of the samples was assessed using a Universal testing machine (Shimadzu EZ Graph, Kyoto, Japan) equipped with a 100 N load cell and operated at a tensile speed of 20 mm min^{-1} in ambient conditions. For testing specimens in the wet state, they were typically immersed in water at room temperature for a duration of 72 h before the test. Quintuplicate samples with dimensions of 2.2 mm in width and 0.3–0.4 mm in thickness were prepared using a dumbbell-shaped cutter to evaluate their mechanical properties. Tensile strain (ε) was defined as the relative elongation of a specimen and quantified by the ratio of the length change (Δl) to the initial gauge length (l_0). Tensile strength (σ) was calculated as the force (F) applied on the specimen per unit cross-sectional area. Young's modulus (E) was

derived from the initial linear portion of the stress-strain (σ–ε) curve, specifically within the 5–15% strain interval. Toughness was determined using the area underneath the stress-strain curve.

The morphologies of the films before and after the degradation test were characterized by a Scanning Electron Microscope (SEM) using the SU3500 device (Hitachi) operated at 10 kV. The films were freeze-dried and sputtered with gold using the MSP-1S magnetron sputter (Vacuum Device Inc., Osaka, Japan).

1.3 Results and Discussion

PEG has been utilized for the synthesis of PLA-PEG-PLA triblock copolymers via ROP, and it is showing rapid progress. However, research on the reaction between short-chain segments of PLA-PEG-PLA (with PLA units < 50) and isocyanate to produce polyurethane is scarce. **Scheme 1-1** depicts the development of PEG-PLA multiblock copolymers with short PLA chain segments, aiming to enhance abrasion resistance and durability under daily use and wet conditions while promoting rapid degradation in marine environments. By adjusting the copolymer's structure and composition, the goal was to achieve a balance between mechanical properties, durability in DIW, and controlled biodegradability in seawater. This study aims to design a PLA-based bioplastic that can biodegrade rapidly in marine environments while maintaining excellent durability in DIW for a variety of daily applications. The key is to strike a balance between toughness, flexibility, and hydrophilicity. This was achieved by incorporating hydrophilic and flexible PEG into PLA by adjusting the PEG/PLA feed ratio. The flexible PEG improved the copolymer's hydrophilicity and toughness. Moreover, a specific crystallization ability was necessary to enhance mechanical properties, leading to the selection of PEG-diol with a M_n of 4000 g mol^{-1} to meet these design criteria.

1.3.1 Chemical structures of PEG-PLA multiblock copolymers

The different constitutive repeating units of the PEG-PLA copolymers are depicted in **Fig. 1-1a**, illustrating alternating (i) and random (ii) blocks. ^{1}H NMR spectroscopy was used to verify the chemical structures and segment compositions. **Table 1-1** lists the corresponding L-

lactide conversion, M_n, and weight fractions (F). Typical ^{1}H NMR spectra of PEG-PLA and PLA are shown in **Fig. 1-1b**, where several signals can be distinguished. The strong proton peaks appearing at ***a*** **(CH, δ_m = 5.10–5.20 ppm)** and ***b*** **(CH$_3$, δ_d = 1.45–1.60 ppm)** are attributed to the methine and methyl protons of PLA, respectively. The chemical shift of ***d*** **(CH$_2$, δ_t = 3.60–3.70 ppm)** is assigned to the methylene protons on the backbone of PEG. Peak ***f*** **(CH$_2$-CH$_2$-<u>CH$_2$</u>-NH-CO, δ_q = 3.10–3.20 ppm)** is related to the methylene in the isocyanate after the coupling reaction, which implies the formation of a urethane linkage in the PEG-PLA and PLA. In addition, it is apparent in **Fig. 1-1c** that distinct chemical shifts of corresponding samples are observable in the magnified ^{1}H NMR spectra. Specifically, peaks **i+*j*** **(-O-<u>CH$_2$</u>-CH$_2$-CH$_2$-CH$_2$-O-, δ_t = 4.13–4.17 ppm)** are exclusively present in the random-structure PEG-PLA copolymers and PLA homopolymer. This specificity is attributed to the PLA segments, which undergo direct ROP initiated by 1,4-butanediol and are subsequently terminated with butanediol [37].

Table 1-1 The characteristics of PLA-PEG-PLA-diol prepolymers, PEG-PLA multiblock copolymers, and PLA homopolymers

Samples	Ring-opening–Prepolymer				Coupling–PEG-PLA copolymer					
	PEG/ L-Lactide (wt/wt)	L-Lactide conversion (%)	M_n (g/mol) (theo.)	M_n (g/mol) (NMR)	PEG/ PLA (wt/wt)	F^b (wt%)			$M_n \times 10^4$ (g/mol) (GPC)	M_w/M_n $Đ$ (GPC)
						F_{PEG}	F_{PLA}	F_{HDI}		
PEG$_{4k}$PLA$_{0.5k}$-*a*	1.0/0.25	92.65	5000	4632	-[a]	83.15	13.46	3.39	10.38	1.76
PEG$_{4k}$PLA$_{1k}$-*a*	1.0/0.50	91.96	6000	5518	-[a]	70.31	26.79	2.90	5.39	1.86
PEG$_{4k}$PLA$_{1.5k}$-*a*	1.0/0.75	92.82	7000	6497	-[a]	59.98	37.45	2.57	4.84	1.95
PEG$_{4k}$PLA$_{2k}$-*a*	1.0/1.0	94.69	8000	7575	-[a]	51.66	46.18	2.16	9.14	1.56
PEG$_{4k}$PLA$_{3k}$-*a*	1.0/1.5	94.37	10000	9437	-[a]	41.62	55.63	2.75	5.38	1.48
PEG$_{4k}$PLA$_{4k}$-*a*	1.0/2.0	93.41	12000	11125	-[a]	35.13	63.24	1.63	6.63	2.16
PEG$_{4k}$PLA$_{2k}$-*r*	-[a]	-[a]	-[a]	-[a]	1.0/1.0	51.05	42.01	6.94	7.17	1.58
PEG$_{4k}$PLA$_{3k}$-*r*	-[a]	-[a]	-[a]	-[a]	1.0/1.5	40.97	53.72	5.31	6.13	1.51
PLA$_{2k}$-*h*	-[a]	-[a]	-[a]	-[a]	-[a]	-[a]	94.35	5.65	6.92	1.56
PLA$_{3k}$-*h*	-[a]	-[a]	-[a]	-[a]	-[a]	-[a]	93.42	6.58	5.63	1.44

[a] Indicates that it is unable to obtain or not happen in this procedure.

[b] Indicates that it is calculated from ^{1}H NMR.

Conversely, the presence of the ***c***, ***a'***, and ***e*** signals are associated with the alternating PEG-

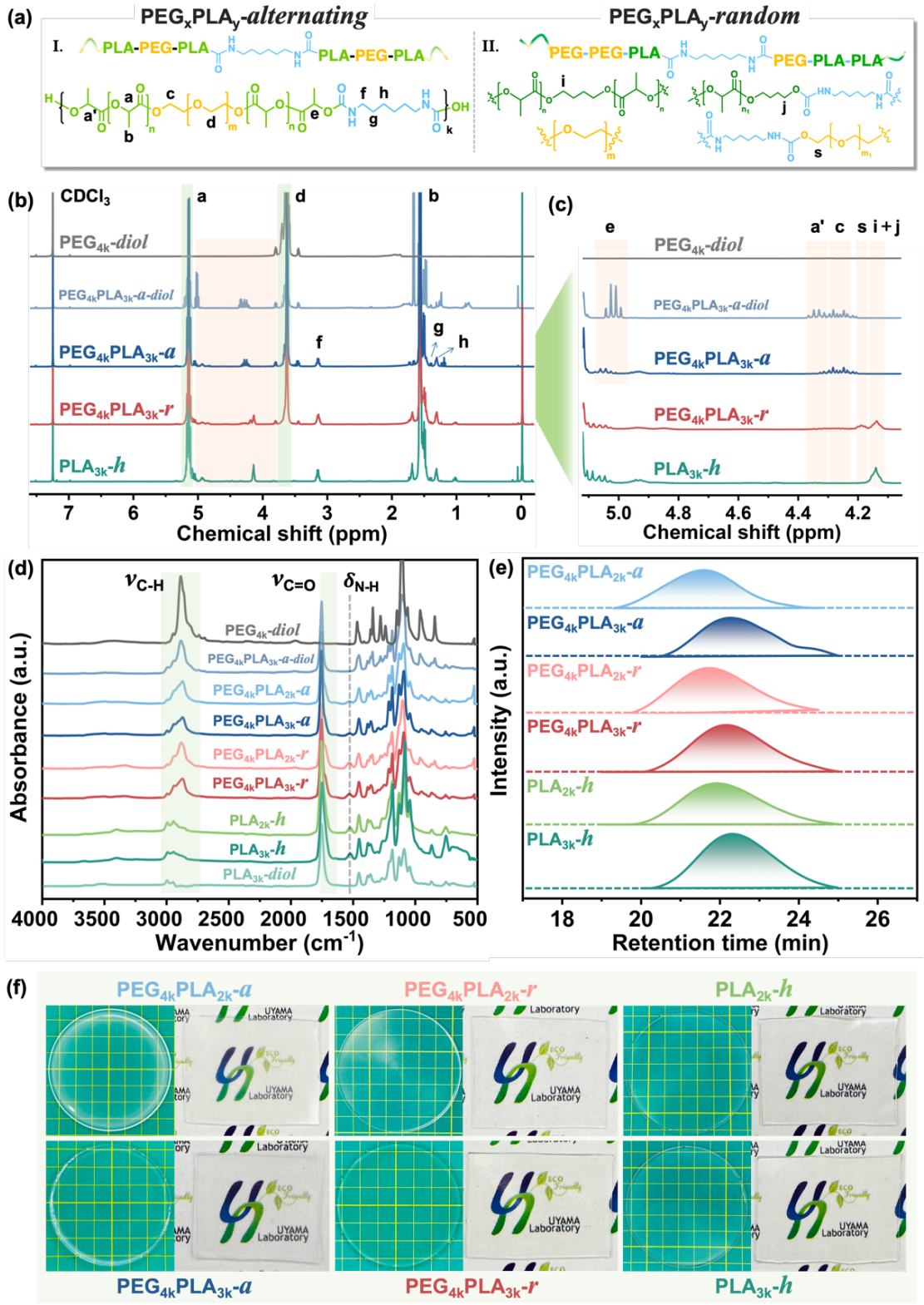

Fig. 1-1. (a) Chemical structural units of PEG-PLA multiblock copolymers with alternating (i) and random (ii) structures. Original (b) and enlarged (c) ^{1}H NMR spectra of PEG-PLA copolymers and PLA homopolymers. (d) FTIR spectra of PEG-PLA copolymers and PLA homopolymers. (e) GPC profiles of PEG-PLA copolymers and PLA homopolymers. (f) Corresponding macro appearance.

PLA copolymer structures. Typical ^{1}H NMR spectra of PEG-PLA and PLA are shown in **Fig. 1-1b**, where several signals can be distinguished. The strong proton peaks appearing at ***a*** **(CH, δ_m = 5.10–5.20 ppm)** and ***b*** **(CH_3, δ_d = 1.45–1.60 ppm)** are attributed to the methine and methyl protons of PLA, respectively. The chemical shift of ***d*** **(CH_2, δ_t = 3.60–3.70 ppm)** is assigned to the methylene protons on the backbone of PEG. Peak ***f*** **(CH_2-CH_2-$\underline{CH_2}$-NH-CO, δ_q = 3.10–3.20 ppm)** is related to the methylene in the isocyanate after the coupling reaction, which implies the formation of a urethane linkage in the PEG-PLA and PLA. In addition, it is apparent in **Fig. 1-1c** that distinct chemical shifts of samples are observable in the magnified ^{1}H NMR spectra. Specifically, peaks **i+*j*** **(-O-$\underline{CH_2}$-CH_2-CH_2-CH_2-O-, δ_t = 4.13–4.17 ppm)** are exclusively present in the random-structure PEG-PLA copolymers and PLA homopolymer. This specificity is attributed to the PLA segments, which undergo direct ROP initiated by 1,4-butanediol and are subsequently terminated with butanediol [37]. Conversely, the presence of the ***c***, ***a′,*** and ***e*** signals are associated with the alternating PEG-PLA copolymer structures.

The chemical structures of PEG-PLA and PLA were further elucidated using FT-IR analysis (**Fig. 1-1d)**. The resulting spectra displayed all the characteristic absorption bands associated with the PLA and PEG components, such as the $\nu_{C\text{-}H}$ of the PEG block at 2876–2882 cm^{-1} and the $\nu_{C=O}$ of the PLA block at 1729 cm^{-1}. Essentially, the amide bond of the polymers was confirmed by distinct peaks at 3500 cm^{-1} and 1529 cm^{-1}, which correspond to the $\nu_{N\text{-}H}$ and $\delta_{N\text{-}H}$ of the –NH group, respectively. Moreover, the signals at 3350–3450 cm^{-1} almost disappeared, implying a positive reaction between the terminal -OH and -NCO of the HDI. These results support the successful synthesis of PEG-PLA and PLA, consistent with the ^{1}H NMR results. The M_n, M_w, and $Đ$ of all resulting samples were determined by GPC, with M_n ranging from 56,300–91,400 g mol^{-1} and $Đ$ of approximately 1.6, confirming the successful synthesis of high M_n PEG-PLA and PLA bioplastics. The controlled composition was efficiently tailored by altering the feed ratio, and as shown in **Fig. 1-1e**, the retention time of each copolymer and homopolymer was recorded by GPC as only a single narrow retention peak in the uniform GPC retention time profiles. Combined with the ^{1}H NMR and FT-IR spectra, PEG-PLA copolymers with sequence-controlled alternating and random structures and different compositions were confirmed, and a series of designed copolymers and

homopolymers were fabricated as expected. The macroscopic appearance of the specimens is shown in **Fig. 1-1f**. Random PEG-PLA copolymers and PLA homopolymers showed better transparency.

1.3.2 Water durability of PEG-PLA multiblock copolymer films

Water and microorganisms predominantly attack hydrophilic molecular chains [38]. Therefore, increasing hydrophilicity can accelerate polymer biodegradation in marine environments by enhancing water absorption. PEG is crucial in the molecular design of PLA-based copolymers to transition from hydrophobic to hydrophilic, increasing potential "breaking points" [22]. To ensure PEG-PLA copolymers remain stable and durable in DIW, their behavior affected by hydrophilic components should be prioritized. This chapter explored the effects of alternating and random structures of PEG-PLA copolymers on their performance.

Table 1-2 The compositions and molecular weight changes of PEG-PLA copolymers, and PLA homopolymers before and after 6 months of DIW soaking

Samples	Original state		DIW 6 months later	
	M_n (g/mol) (GPC)	M_w/M_n $Đ$ (GPC)	M_n (g/mol) (GPC)	M_w/M_n $Đ$ (GPC)
$PEG_{4k}PLA_{2k}$-*a*	91380	1.56	16434	1.71
$PEG_{4k}PLA_{3k}$-*a*	53765	1.48	26643	1.10
$PEG_{4k}PLA_{2k}$-*r*	71684	1.58	*10958*	*1.17*
			6462	*1.24*
$PEG_{4k}PLA_{3k}$-*r*	61342	1.51	*28463*	*1.38*
			12720	*1.33*
PLA_{2k}-*h*	69166	1.56	50063	1.71
PLA_{3k}-*h*	56276	1.44	49087	1.80

Fig. 1-2b shows that copolymers with random structures and shorter PLA chain lengths show more rapid and higher water absorption, suggesting that the irregular arrangement of random chains and lower content of hydrophobic PLA facilitates water molecule diffusion. In contrast to PLA-*h*, PEG-PLA increased the water sensitivity, absorption rate, and capacity (**Fig. 1-2c**). The WCA measurements (**Fig. 1-2d**) aligned with these results. The addition of PEG increased the density of polar ether bonds in the molecular chain compared with neat PLA-*h*. The oxygen atoms are highly electrophilic and can interact with water molecules through

hydrogen bonding, improving the hydrophilicity of the PEG-PLA copolymer, resulting in a

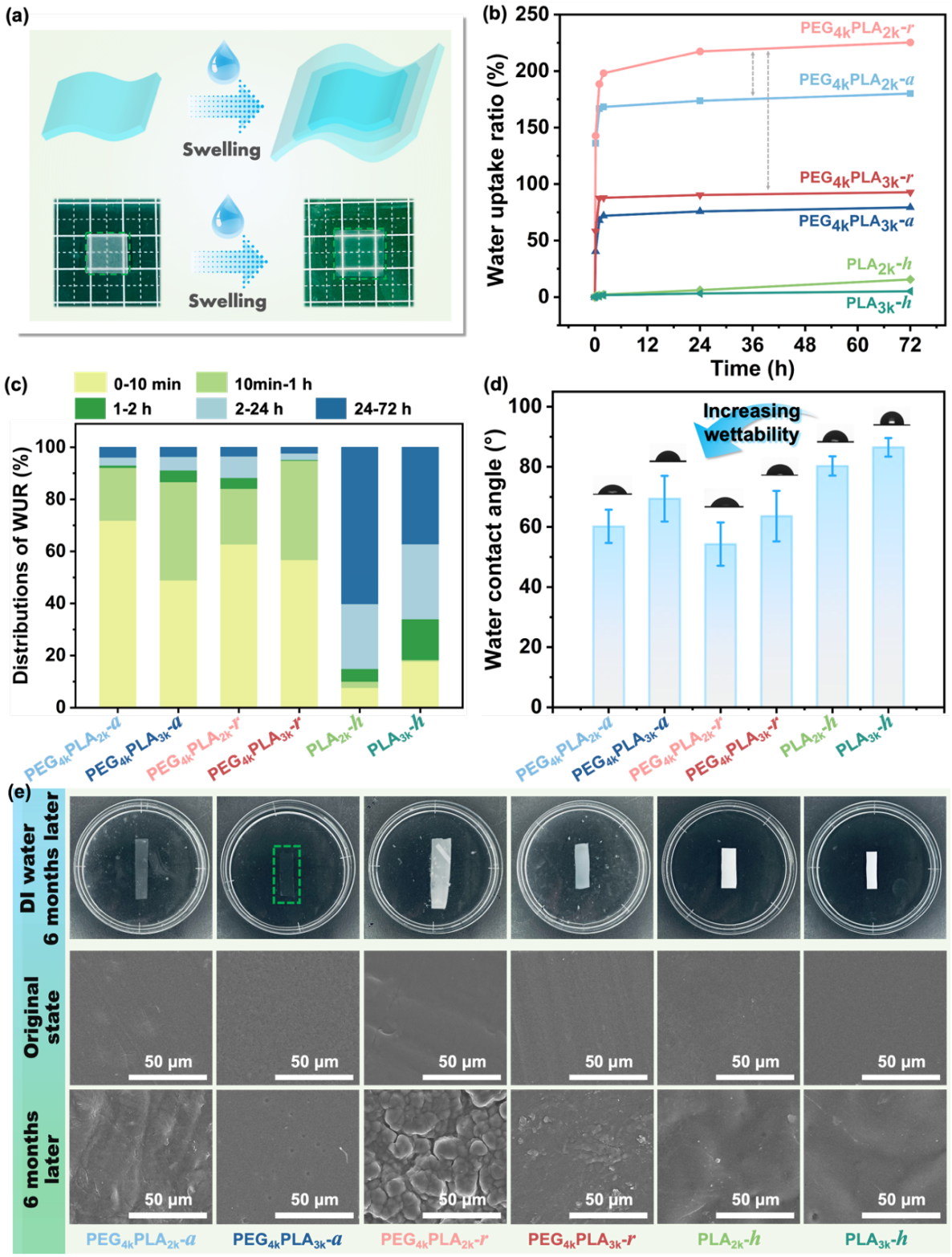

Fig. 1-2. (a) Schematic illustration of the water uptake process of PEG-PLA and PLA films. (b) WUR profile of PEG-PLA and PLA films within 72 h. (c) WUR distributions of all samples after different immersion periods. (d) Water contact angles of PEG-PLA and PLA films. (e) Appearance and microstructures of PEG-PLA and PLA films after 6 months DIW soaking.

significant decrease in the WCA from 80.9° ± 2.3° (PLA_{3k}-*h*) to 38.3° ± 7.2° ($PEG_{4k}PLA_{2k}$-*r*).

Further, I studied the materials after soaking them in DIW at 22 ± 0.5 °C for 6 months. The macroscopic appearance and microscopic morphology, as shown in **Fig. 1-2e**, indicate that all films remained almost complete. The chemical structure and M_n changes of the materials were further characterized using ^{1}H NMR, FT-IR, and GPC (**Fig. 1-3, Table 1-2**), and except for $PEG_{4k}PLA_{2k}$-*r*, the M_n of PLA-*h* decreased very small, while the remaining PEG-PLA copolymers maintained the M_n above 15,000 g mol^{-1}. The characteristic $\delta_{N\text{-}H}$ in FT-IR revealed that amide bonds were still present. Other results also confirmed that the stability of the materials in DIW is considerable.

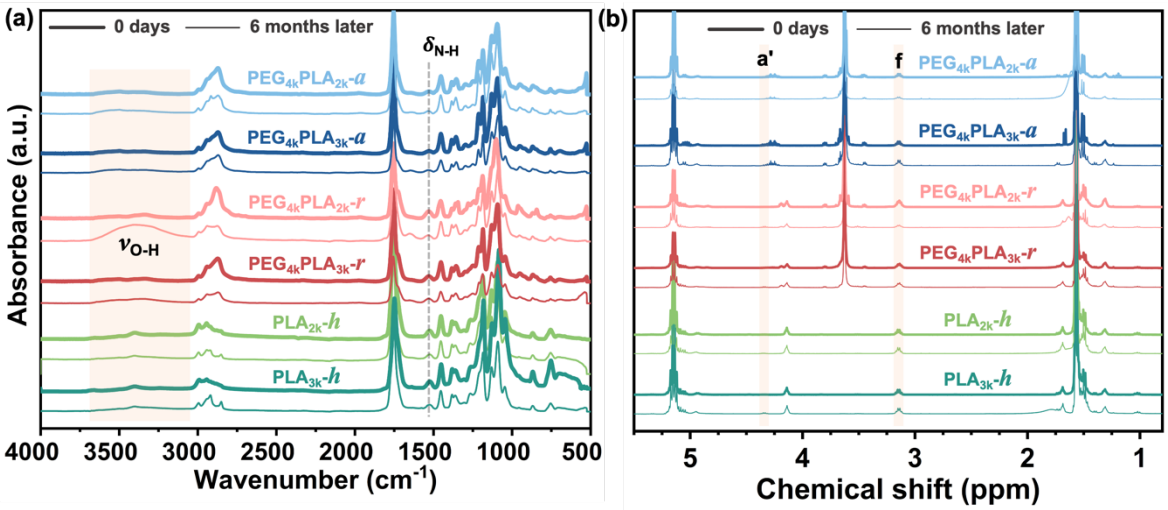

Fig. 1-3. The FT-IR (a), and ^{1}H NMR (b) spectra of PEG-PLA copolymers and PLA homopolymers with different PLA contents.

1.3.3 Thermal properties and crystallinity of PEG-PLA multiblock copolymer films

The thermal and crystallization properties of the PEG-PLA copolymers and PLA homopolymers were investigated by DSC and XRD, respectively. The corresponding data are presented in **Table 1-3**. The integration of PEG into PLA decreased the rigidity of the copolymer because of the flexible ether bond and lower steric hindrance of PEG compared with the ester bonds and -CH_3 group of PLA, enhancing the mobility and arrangement of the molecular chains for increased crystallinity. Copolymers with alternating structures exhibited stronger crystallization, which is attributed to their high regularity and homogeneity. As displayed in **Fig. 1-4a,b**, PEG-PLA with an alternating structure showed a clear crystallization–

melting transition compared with the amorphous thermal behavior of PLA-*h*, which showed no

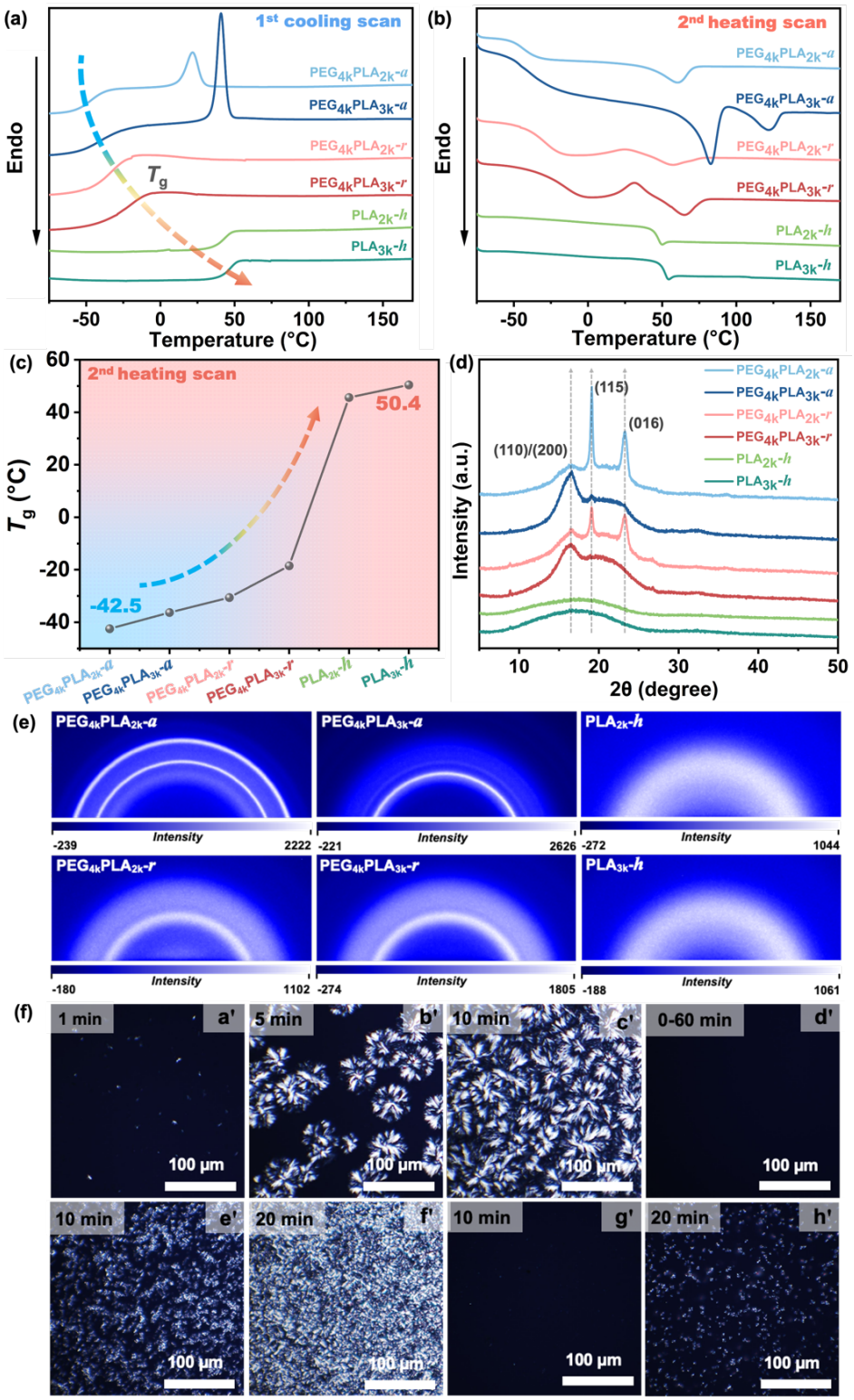

Fig. 1-4. DSC curves of PEG-PCL and PLA during the (a) first cooling and (b) second heating scan. (c) T_g profiles with various structures and PLA contents. (d) 1D XRD and (e) 2D WAXS patterns of PEG-PLA and PLA. (f) POM images of $PEG_{4k}PLA_{3k}$-*a* (a'-c') and $PEG_{4k}PLA_{2k}$-*a* (d') crystallized isothermally at 100 °C; $PEG_{4k}PLA_{3k}$-*a* (e', f') and $PEG_{4k}PLA_{2k}$-*a* (g', h') crystallized isothermally at 55 °C.

corresponding crystallization–melting transition, different from the amorphous thermal behavior of PLA-h. Introducing PEG units disrupts the PLA arrangements, with longer PLA units promoting better copolymer crystallization [39]. This effect increased the crystallization temperature (T_c), melting temperature (T_m), and enthalpy (ΔH) of the copolymers, especially with PLA3000. In addition, polymers with random structures showed lower T_c, T_m, and ΔH than those with alternating structures, with crystallization occurring during heating due to insufficient chain flexibility for crystalline stacking during the cooling process. This suggests that the random copolymer segments have poorer mobility and crystallization rates. As shown in **Fig. 1-4c**, the T_g of copolymers gradually decreased from 50.4 °C to –42.5 °C with increasing PEG, allowing flexibility and low-temperature resistance. The crystallinity of biodegradable polyesters with relatively low T_g enables their development as thermoplastics. Blends of immiscible polymers showed two T_g values, while miscible polymers exhibited a single, composition-dependent T_g, indicating compatibility in amorphous regions [40]. These features suggest that short PLA chains could reduce PEG crystallinity while maintaining compatibility in the amorphous areas.

The XRD patterns in **Fig. 1-4d** show the diffraction peaks of the crystal structure of the samples with different compositions, further verifying the effect of PEG on the crystal structure of the copolymers. For PLA_{2k}-*h* and PLA_{3k}-*h*, broad diffraction peaks are present at 10°–25° because of the scattering of molecular chains. In contrast, the PEG-PLA copolymers show sharp diffraction peaks typical of PLA at 16.60°, corresponding to the (110) or (200) planes of the orthorhombic crystals of the α-crystalline phase of PLA [41]. The intensity of the peaks indicates the introduced PEG induced an α-crystalline structure and improved the crystallinity of PLA. In contrast to $PEG_{4k}PLA_{3k}$, characteristic diffraction peaks of the PEG phases appear at 19.10° and 23.25° in $PEG_{4k}PLA_{2k}$ owing to the increase in the relative content of PEG; these peaks are attributed to the lattice planes of (115) and (016), respectively [42,43]. In conclusion, the diffraction peak locations did not change with the introduction of PEG, and the copolymers exhibited features of semi-crystalline polymers with similar crystal structures. The intensity of the corresponding peaks decreased, demonstrating that the alternating structure had stronger crystallizability than the random structure. Moreover, 2D WAXS analysis was utilized to

illustrate the difference between the alternating and random structures of the copolymers (**Fig. 1-4e**), and the results were consistent with the XRD results. Considering the above DSC analysis, copolymers with random structures presented crystallization peaks during the second heating scan because a weaker crystallization capacity is required for a slower cooling rate. This supported the conclusions drawn from the XRD patterns.

To fully understand the crystallinity growth and spherulite size of PEG-PLA and PLA, POM was employed to monitor in situ crystal growth during the isothermal process. Optical micrographs were obtained after melting specimens and rapidly cooling them. **Fig. 1-4f(a'-c')** shows the isothermal crystallization of $PEG_{4k}PLA_{3k}$-*a* at 100 °C, where only PLA spherulites can grow. Initially, PLA nucleation occurred, forming tiny spherical crystals [**Fig. 1-4f(a',b')**]. Over time, these crystals grew, but most remained imperfect at the end of crystallization [**Fig. 1-4f(c')**]. In $PEG_{4k}PLA_{2k}$-*a* [**Fig. 1-4f(d')**], no crystals formed due to shorter PLA chains and higher PEG content. $PEG_{4k}PLA_{3k}$-*r* and $PEG_{4k}PLA_{2k}$-*r* showed similar results due to random chain segment arrangements [**Fig. 1-5(a-c)**]. At 55 °C, $PEG_{4k}PLA_{3k}$-*a* showed smaller and arranged densely spherulite nuclei [**Fig. 1-4f(e',f')**]. This rigidity promoted PEG nucleation but restricted the rate. Initial crystallization was attributable to PEG, with separate crystallization of PEG and PLA chains observed [**Fig. 1-4f(f')**]. This indicates that the crystallization of the PEG and PLA chains occurred separately, which is consistent with the

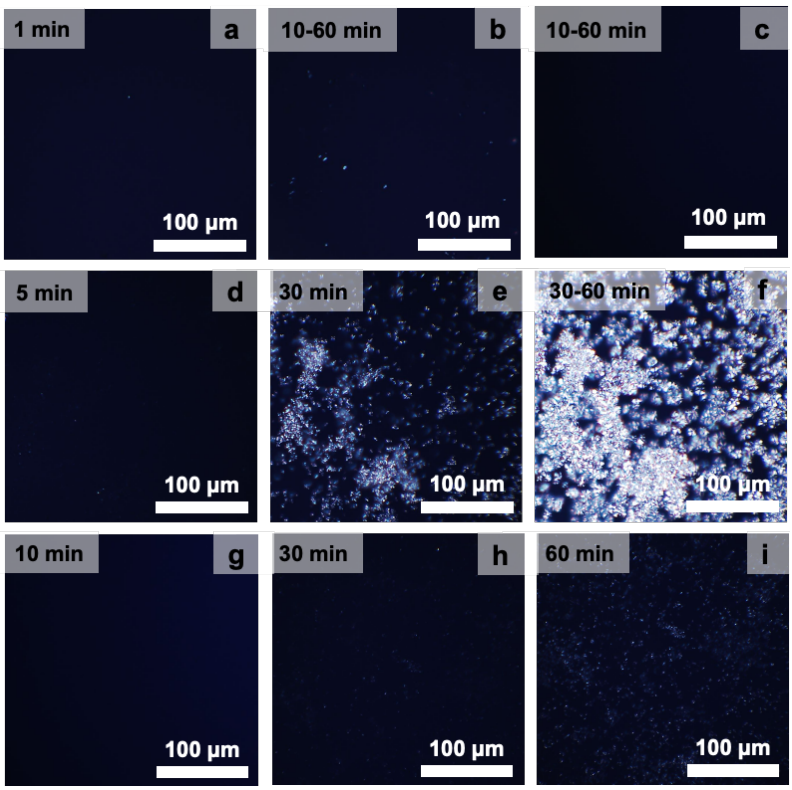

Fig. 1-5. POM images of $PEG_{4k}PLA_{3k}$-*r* (a-b) and $PEG_{4k}PLA_{2k}$-*r* (c) crystallized isothermally at 100 °C; $PEG_{4k}PLA_{3k}$-*r* (d-f) and $PEG_{4k}PLA_{2k}$-*r* (g-i) crystallized isothermally at 55 °C.

findings on diblock copolymers reported by Arnal et al. [44]. $PEG_{4k}PLA_{3k}$-*a* displayed the most rapid spherulitic growth, superior to that of $PEG_{4k}PLA_{2k}$-*a* [**Fig. 1-4f(g',h')**], $PEG_{4k}PLA_{3k}$-*r* [**Fig. 1-5(d-f)**], and $PEG_{4k}PLA_{2k}$-*r* [**Fig. 1-5(g-i)**], consistent with DSC results.

As a result, $PEG_{4k}PLA_{2k}$-*a* and $PEG_{4k}PLA_{3k}$-*a* displayed noticeable crystallization behaviors. The compatibility in the amorphous region and mutual restriction during crystallization were verified; alternating structures led to a lower WUR and superior mechanical properties, which were attributed to their strong crystallization ability and uniform molecular structure. Moreover, their crystallization behavior was strongly affected by the chain segment length, chain sequence distribution, and copolymer composition during the adjusted transition from amorphous to semi-crystalline structures, ultimately affecting their WUR ability and mechanical properties. The microstructure can be precisely controlled by tailoring the feed ratio and synthesis procedures, striking a balance between mechanical properties and biodegradability for DIW durability and tunable rapid biodegradability in seawater.

Table 1-3 Characteristic data of conventional DSC analysis

Samples	T_g [a] (°C)	T_c (°C)	ΔH_c (J g^{-1})	T_m (°C)	ΔH_m (J g^{-1})	X_c (%)
$PEG_{4k}PLA_{2k}$-*a*	– 42.5	22.1	9.23	61.1	10.94	10.76 [c]
$PEG_{4k}PLA_{3k}$-*a*	– 36.3	42.9	16.40	82.3 122.2	15.92 4.87	40.18 [d]
$PEG_{4k}PLA_{2k}$-*r*	– 30.6	25.1 [b]	3.82 [b]	57.5	3.85	3.83 [c]
$PEG_{4k}PLA_{3k}$-*r*	– 18.5	31.8 [b]	6.16 [b]	65.6	6.53	13.07 [d]
PLA_{2k}-*h*	45.6	- [e]	- [e]	- [e]	- [e]	- [e]
PLA_{3k}-*h*	50.4	- [e]	- [e]	- [e]	- [e]	- [e]

[a] Obtained from the second heating scan.

[b] Cold crystallization temperature and enthalpy obtained from the heating scan.

[c] The X_c was calculated by $\Delta H^0_{m,\,PEG}$ of 196.8 J g^{-1} [45].

[d] The X_c was calculated by $\Delta H^0_{m,\,PLA}$ of 93 J g^{-1} [46].

[e] No thermal transition was detected in the cooling or heating process.

1.3.4 Thermal stability and dynamic viscoelastic properties of PEG-PLA multiblock copolymer films

The thermal stability of the PEG-PLA copolymers under a nitrogen atmosphere was

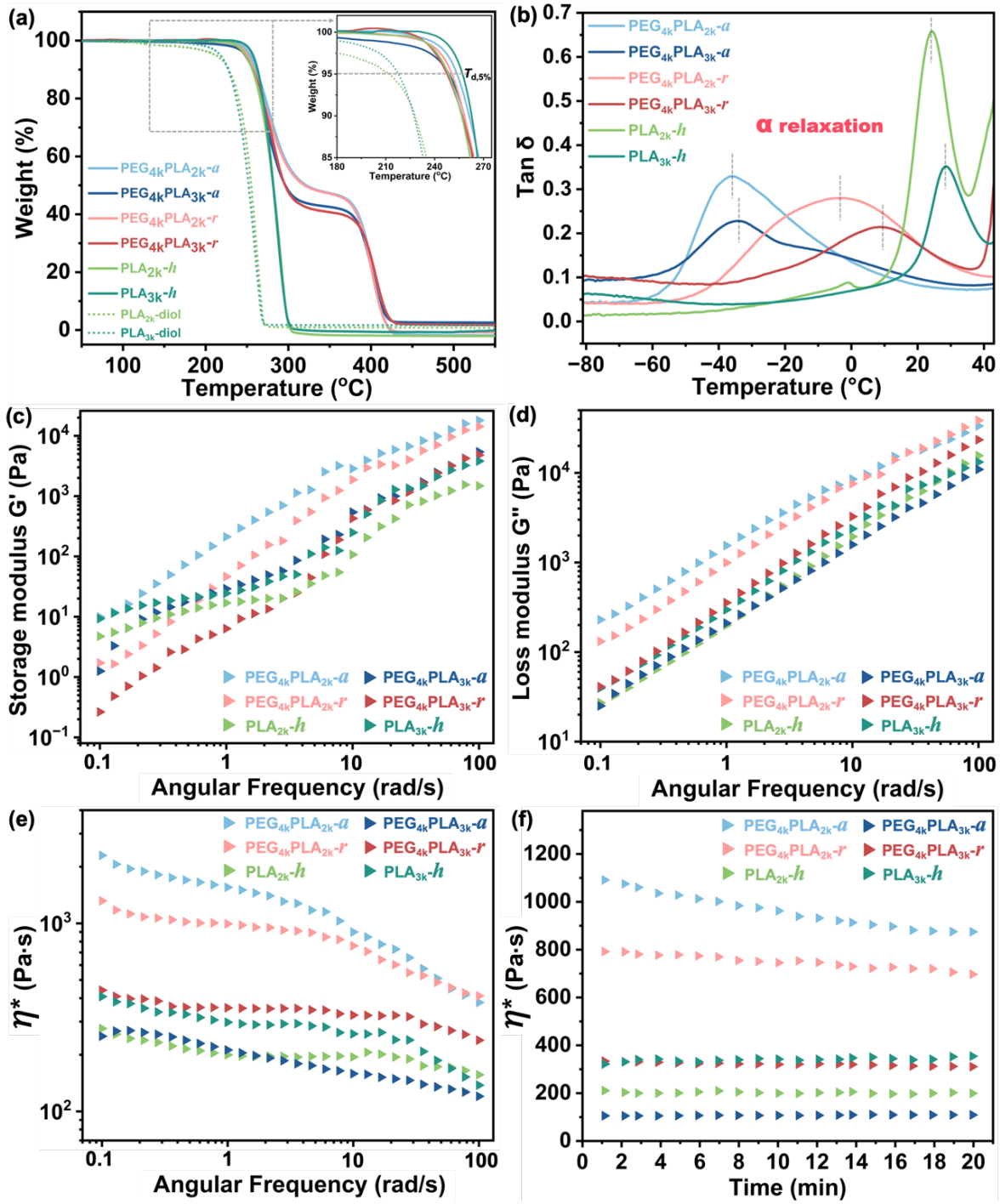

Fig. 1-6. (a) TGA curves of PEG-PLA and PLA. (b) Tan δ as a function of temperature for PEG-PLA and PLA recorded by DMA. (c) Dynamic storage modulus, (d) dynamic loss modulus, (e) complex viscosity, and (f) time-oscillation scanning curves of PEG-PLA and PLA at T_r = 130 °C.

evaluated using TGA, as shown in **Fig. 1-6a**. The corresponding data, such as the temperature of 5% weight loss ($T_{d,\,5\%}$) and maximum decomposition temperature ($T_{d,\,max}$), are listed in **Table 1-4**. The thermal decomposition profiles of the PEG-PLA copolymers and PLA homopolymers displayed $T_{d,\,max}$ values comparable to those of the prepolymers. With PEG incorporation, the

curves showed a dual-stage thermal degradation corresponding to the distinct components. A slight decrease in $T_{d\ and\ max\text{-}PLA}$ compared with that of PLA-*h* was observed with longer PLA chain segments. In contrast, the PEG component remained stable and unaffected by the presence of PLA. The $T_{d\ max}$ values of the random copolymers were slightly higher than those of the alternating copolymers, possibly owing to longer chain segments in the random copolymers. All the copolymers demonstrated thermal stability up to 240 °C, with $T_{d,\ max}$ surpassing 400 °C, providing enhanced thermal stability for a wider processing window.

Table 1-4 The thermal degradation temperature of PEG-PLA copolymers, and PLA homopolymers and their prepolymers

Samples	$T_{d,\ 5\%}$ (°C)	$T_{d,\ max}$-PLA (°C)	$T_{d,\ max}$-PEG (°C)
$PEG_{4k}PLA_{2k}$-*a*	253.8	276.5	403.4
$PEG_{4k}PLA_{3k}$-*a*	248.9	270.9	400.8
$PEG_{4k}PLA_{2k}$-*r*	250.7	279.3	405.1
$PEG_{4k}PLA_{3k}$-*r*	247.6	282.3	406.2
PLA_{2k}-*h*	248.5	289.6	-
PLA_{3k}-*h*	257.2	292.8	-
PLA_{2k}-diol	212.2	261.6	-
PLA_{3k}-diol	217.8	264.2	-

The variation in tan δ with temperature for the PEG-PLA and PLA was evaluated using DMA. In **Fig. 1-6b**, only a single relaxation peak on each tan δ curve was observed in the temperature range of –80 °C to 40 °C, which was related to the T_g in the amorphous region of polymers. The introduction of PEG improved the mobility of PLA, and the α relaxation peak shifted to lower temperatures. In contrast to the alternating structures, the random structures presented higher T_g, corresponding to the DSC analysis results.

Dynamic viscoelastic parameters are essential for polymer processing techniques like melt spinning, injection, and extrusion molding [47]. The complex viscosity (η^*), dynamic storage modulus (G'), and dynamic loss modulus (G'') curves were measured using a rotational

rheometer at 130 °C. As shown in **Fig. 1-6(c-f)**, all samples exhibited pseudoplasticity shear thinning behavior. The rheological properties varied with composition, with the low-frequency region reacting to large-scale rearrangements of the chain conformations and the high-frequency region reacting to limited chain segments [48]. The incorporated PEG may moderate shear thinning at high shear rates by reinforcing intermolecular interactions within the copolymer matrix. The minimal decrease in complex viscosity over time demonstrated good PEG-PLA and PLA thermal stability during early shear stages, which is crucial for processing applications (**Fig. 1-6f**).

1.3.5 Mechanical properties of PEG-PLA multiblock copolymer films

The mechanical performance of PEG-PLA copolymers is crucial for their practical application. Therefore, it is essential to understand their mechanical behavior under both dry and wet conditions based on the need for DIW durability. Similarly, I compared PEG-PLA with alternating structures and varying PLA chain lengths to tailor the PEG content. Copolymers with PLA chain lengths of 2000 and 3000 g mol^{-1} were selected to study the differences in alternating and random structures for a trade-off between biodegradability and mechanical properties. As illustrated in **Fig. 1-7a,b,** and data in **Table 1-5**, all PEG-PLA copolymers exhibited substantially improved flexibility and toughness compared to PLA-*h*. Despite a reduction in Young's modulus (E), the mechanical requirements of various applications were satisfied. Detailed mechanical characteristics describing the mechanical attributes of copolymers in both dry and wet conditions, including the elongation at break (ε_b), maximum stress (σ_m), E, and toughness, are presented in **Fig. 1-7(c-f),** respectively. An increase in PLA chain length produced a transition in the copolymer from rubber-like to plastic-like, with a corresponding rise in E, possibly attributable to enhanced crystallization ability.

In the dry state, alternating copolymers tend to have a more regular structure, leading to better crystallinity. This results in well-defined crystalline regions for the lower T_g that enhance mechanical strength and toughness [49]. However, in the wet state, the alternating-structure copolymers retained considerable mechanical properties, presenting increased ε_b and toughness,

while the strength did not decrease significantly. This reinforcement might be due to water

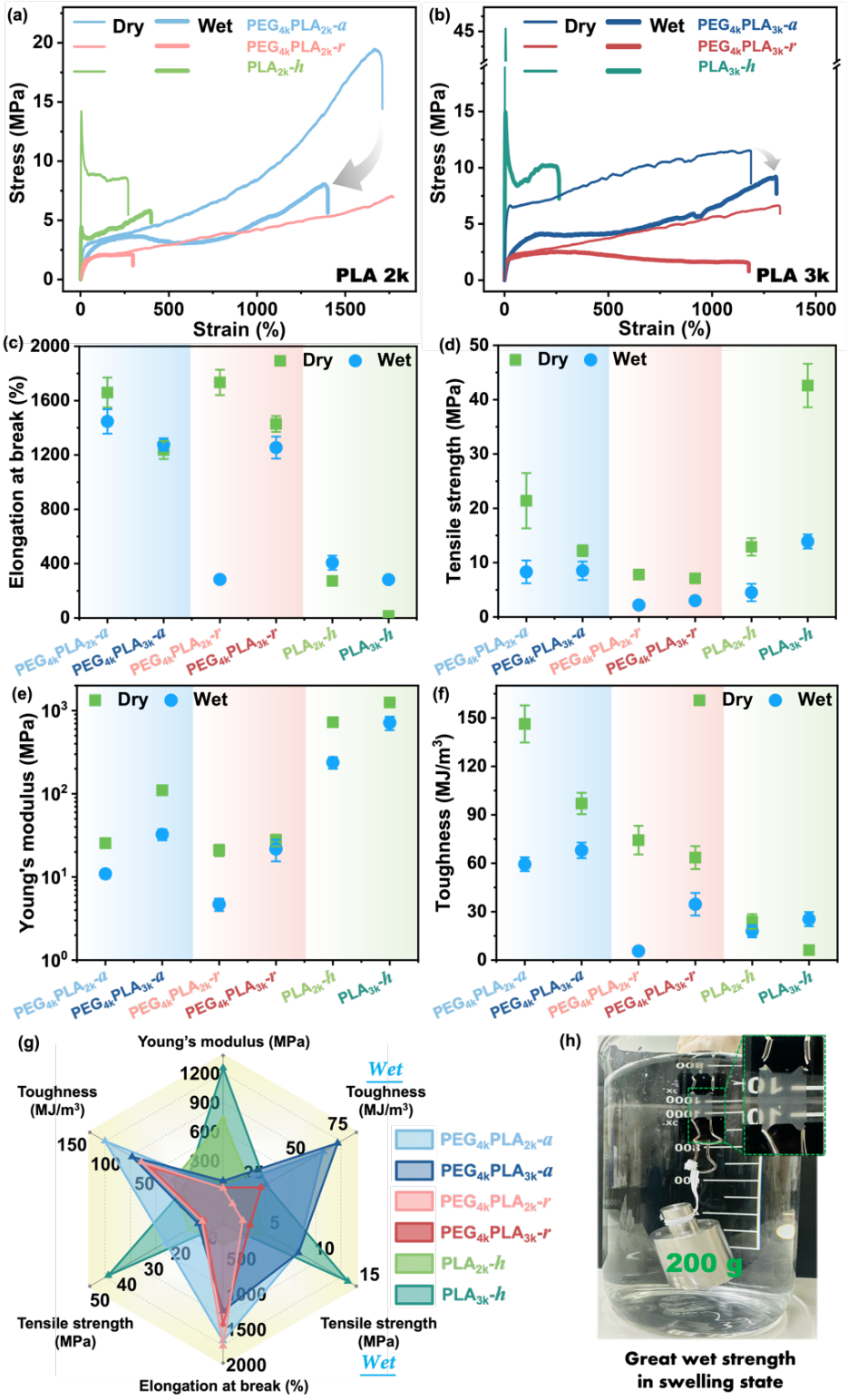

Fig. 1-7. Typical engineering stress–strain curves of PEG-PLA copolymers and PLA homopolymers with PLA 2k (a) and PLA 3k (b) chain segments in dry and wet states. (c) ε_b, (d) σ_m, (e) E, and (f) toughness of PEG-PLA and PLA in dry and wet states. (g) Comparative totalization of the mechanical properties of whole systems. (h) $PEG_{4k}PLA_{3k}$-*a* immersed in DIW at ambient atmosphere for 2 months and utilized for wet strength tests, as indicated by the green dotted line.

diffusion, resulting in an amorphous state of the PEG and PLA segments, which exhibit excellent compatibility and mobility, particularly for shorter PLA chain segments. This uniform dispersion of the chains prevents stress concentration, thereby enhancing the stretchability of the copolymers. This is also attributed to the regularity of crystallization and the formation of hydrogen bonds between water and the PEG in the chain segment, thus strengthening the intermolecular chain forces and supporting the mechanical strength.

A comprehensive summary of the mechanical behavior in various states is depicted in **Fig. 1-7g**, demonstrating the alternating structure with superior properties, and the introduction of PEG into PLA allows the bioplastic to develop sufficient potential for applications even in moist environments. As shown in **Fig. 1-7h**, $PEG_{4k}PLA_{3k}$-*a* was immersed in DIW at room temperature (22 ± 0.5 °C) for 2 months and still displayed exceptional wet strength.

Table 1-5 Mechanical properties of PEG-PLA copolymers under different conditions

Samples	Films state	Young's Modulus *E* (MPa)	Toughness (MJ/m^3)	Tensile Strength σ_m (MPa)	Elongation at break ε_b (%)
$PEG_{4k}PLA_{2k}$-*a*	Dry	21.5 ± 1.8	125.3 ± 11.5	21.4 ± 5.1	1659.3 ± 110.4
$PEG_{4k}PLA_{3k}$-*a*	Dry	91.9 ± 5.7	85.0 ± 6.6	9.2 ± 1.0	1236.7 ± 66.5
$PEG_{4k}PLA_{2k}$-*r*	Dry	17.2 ± 2.3	71.3 ± 8.3	7.8 ± 0.8	1734.0 ± 93.2
$PEG_{4k}PLA_{3k}$-*r*	Dry	23.2 ± 4.5	57.7 ± 7.1	7.1 ± 0.5	1428.6 ± 58.2
PLA_{2k}-*h*	Dry	726.2 ± 47.6	23.9 ± 4.6	12.9 ± 1.6	272.7 ± 4.4
PLA_{3k}-*h*	Dry	1253.1 ± 102.0	6.2 ± 2.1	42.6 ± 4.0	15.1 ± 3.7
$PEG_{4k}PLA_{2k}$-*a*	Wet	9.2 ± 1.2	59.4 ± 4.3	8.3 ± 2.1	1446.8 ± 89.8
$PEG_{4k}PLA_{3k}$-*a*	Wet	16.5 ± 2.9	68.0 ± 4.8	8.4 ± 1.7	1277.3 ± 45.6
$PEG_{4k}PLA_{2k}$-*r*	Wet	6.0 ± 0.8	5.6 ± 1.6	2.2 ± 0.2	283.8 ± 21.9
$PEG_{4k}PLA_{3k}$-*r*	Wet	21.8 ± 6.3	22.6 ± 7.0	3.0 ± 0.5	1254.2 ± 80.5
PLA_{2k}-*h*	Wet	238.5 ± 38.6	17.9 ± 3.8	4.5 ± 1.6	406.8 ± 52.3
PLA_{3k}-*h*	Wet	715.0 ± 133.4	25.4 ± 4.4	13.9 ± 1.3	282.5 ± 23.5

1.3.6 Hydrolytic and enzymatic degradation of PEG-PLA multiblock copolymer films

Since this research aims to enhance the biodegradability of copolymers in marine environments, the low microbial concentrations in seawater should be addressed carefully. If

the PEG-PLA copolymer can undergo enzymatic biodegradation at lower enzyme (or microorganisms) concentrations, the possibility of marine biodegradation will significantly increase. Therefore, enzymatic degradation experiments with proteinase K were investigated before conducting marine biodegradation experiments. Because of its serine protease activity and broad substrate specificity, proteinase K effectively catalyzes PLA hydrolysis, similar to peptide bond cleavage in alanine-like PLA monomers. This enzymatic degradation, which is influenced by pH and temperature, occurs primarily through the interaction of nucleophilic residues of serine with ester bonds [50,51]. Such interactions lead to rapid and random ester bond cleavage in PLA. Given the similarity of the ester and amide bonds in PEG-PLA and PLA to peptide bonds, they are likewise susceptible to degradation, particularly in alkalescent marine environments. Consequently, I conducted hydrolytic (as a blank control group) and enzymatic degradation experiments of PEG-PLA and PLA without proteinase K in Tris-HCl buffer (pH = 8.5) at 37 °C for 120 h. The degradation tests in Tris-HCl buffer without proteinase K showed noticeable weight loss (<5%), except for the $PEG_{4k}PLA_{2k}$ copolymer. **Fig. 1-8b** shows the corresponding microscopic results. As polyurethanes are recognized to possess the structural characteristics of polyesters and polyamides, their sensitivity to hydrolytic degradation is identical to that of polyesters and polyamides. The urethane bond is also hydrolyzed with the facile hydrolysis of the ester group, but it is less susceptible, resulting in organic fragments (carboxylic acids, amines, or alcohols) [52,53].

0.2 mg mL^{-1} of proteinase K is typically used for enzymatic degradation reactions [54]. I first observed the behavior of the samples under this enzymatic degradation condition; however, all the samples dissolved in this condition within 24 h. Hence, I adjusted the proteinase K concentration to an optimal concentration of 0.0125 mg mL^{-1}, considering the hydrophilic nature of the samples. This optimization was crucial because higher concentrations led to complete dissolution within 24 h, which overwhelmed the comparative analysis. As shown in **Fig. 1-8a** and **Fig. 1-9a**, except for PLA-*h*, only $PEG_{4k}PLA_{3k}$-*a* retained a minor residual weight. As a semi-crystalline copolymer, the reduced crystallinity and crystal size caused by the random structure promotes penetration of water molecules into the molecular chain to contact the ester and amide bonds, facilitating proteinase K access. Moreover, the WAC of PEG-PLA gradually decreased with shorter PLA chains, causing stronger interaction forces between the molecular

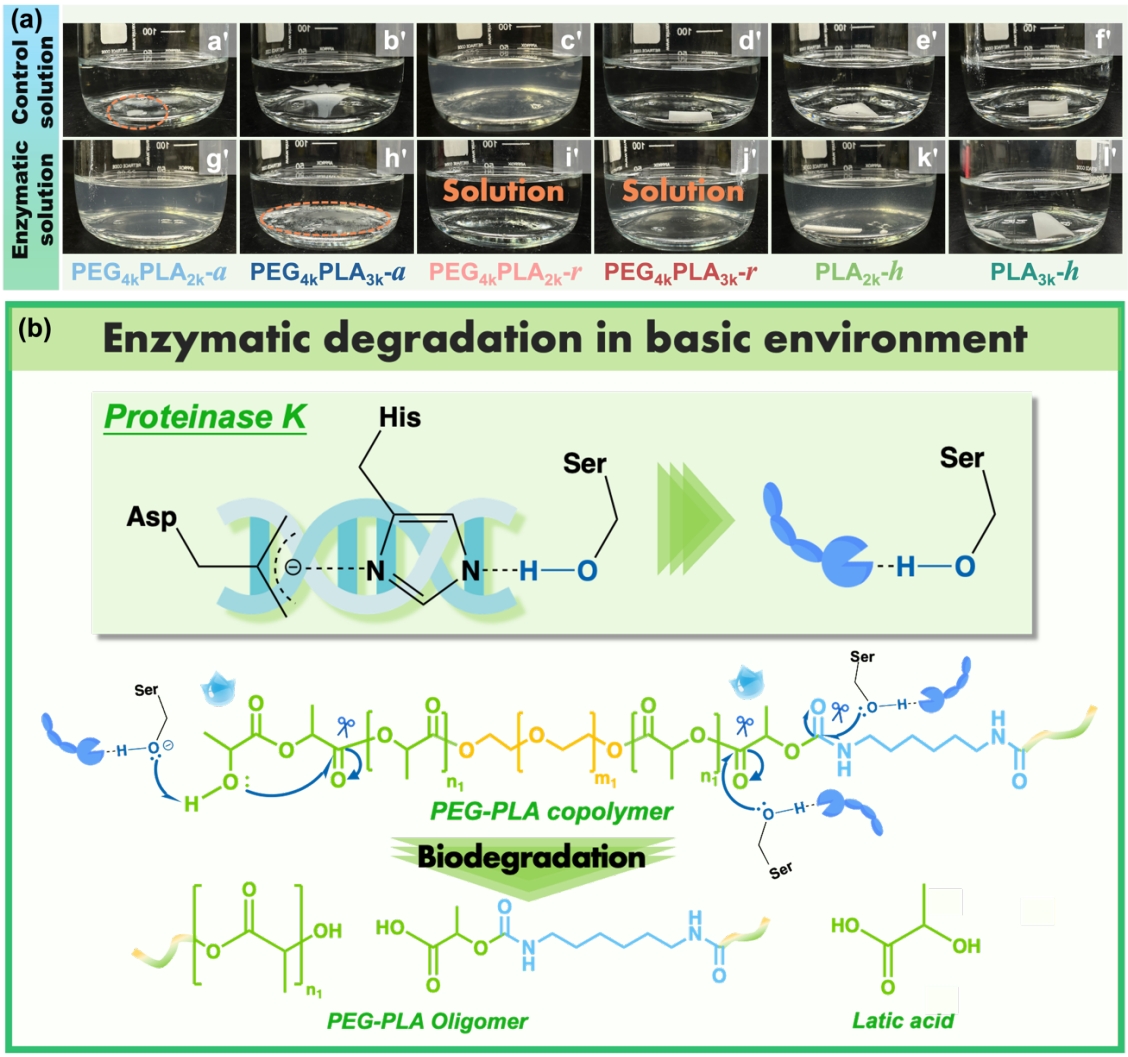

Fig. 1-9. (a) Enzymatic biodegradation of samples in proteinase K solution at 37 °C for 120 h. (b) Mechanism of proteinase K action on the PEG-PLA copolymer.

chains and water. Consequently, $PEG_{4k}PLA_{2k}$ copolymers were degraded entirely within 72 h, resulting in a transparent solution. In contrast, PLA_{2k}-*h* showed a weight loss of approximately 30% compared to PLA_{3k}-*h*, attributed to its amorphous nature, increased WCA, and hydrophilicity. **Fig. 1-8b** shows the microstructure changes of materials after enzymatic degradation, consistent with the residue weight results. **Fig. 1-9b** shows a possible enzymatic degradation mechanism. Overall, enzymatic degradation by proteinase K was significantly faster than the slower hydrolytic degradation in the Tris-HCl buffer solution. The PEG units enhanced the hydrophilicity and promoted the biodegradability of the PEG-PLA copolymers.

1.3.7 Marine biodegradation of PEG-PLA multiblock copolymer films with seawater based on the BOD analysis

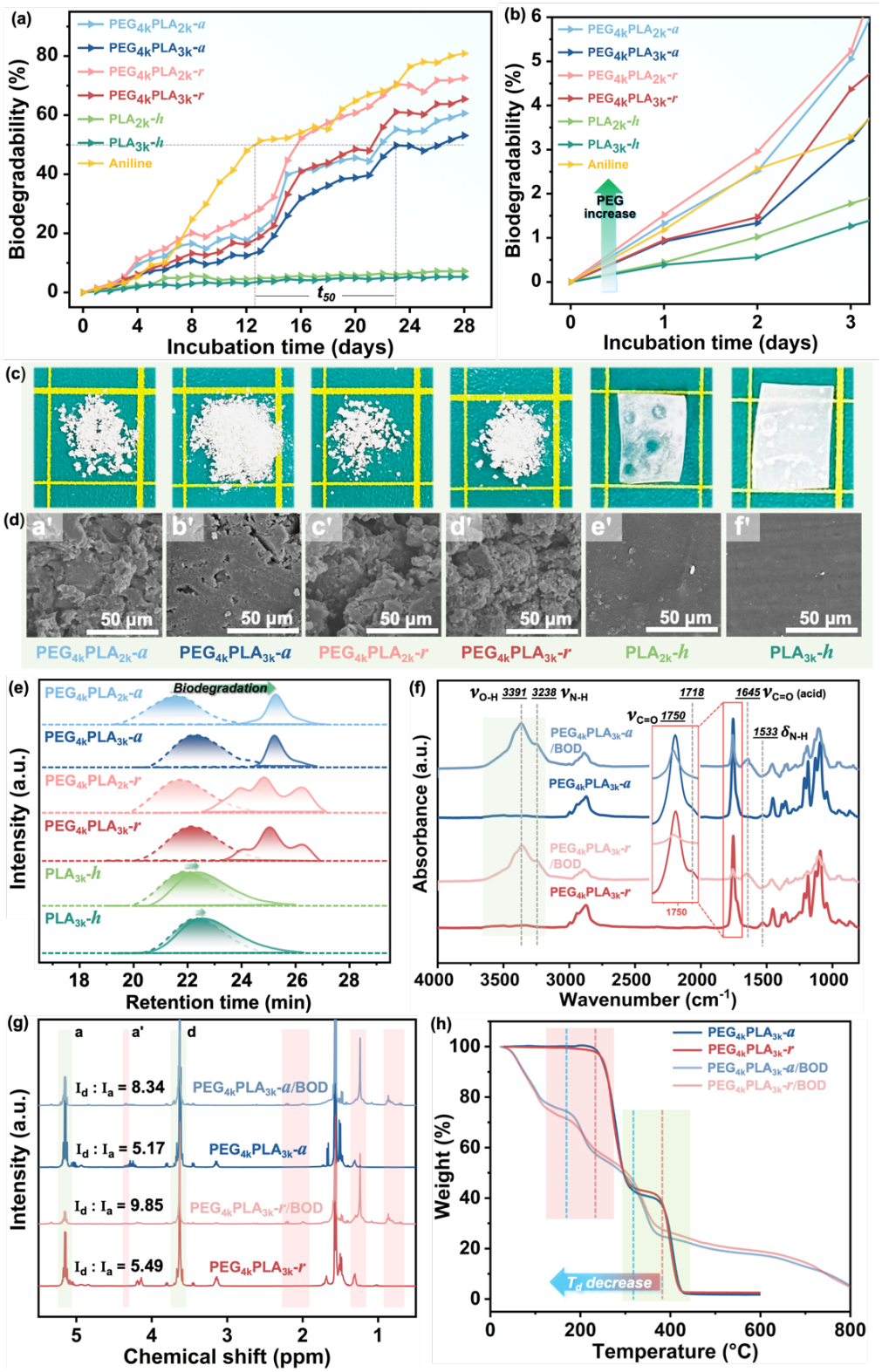

Fig. 1-10. (a) Comparison of the biodegradability of all samples after 28 d of seawater degradation. (b) Biodegradability of all samples in the initial stage of seawater degradation. After 28 d of seawater degradation, (c) macroscopic morphological changes of PEG-PLA and PLA films; (d) microscopic morphological changes of PEG-PLA and PLA films. recorded by SEM; (e) the retention time of all samples, the changes in the chemical structures and thermal stability of $PEG_{4k}PLA_{3k}$-*a* and $PEG_{4k}PLA_{3k}$-*r* demonstrated by (f) FT-IR, (g) ^{1}H NMR and (h) TGA, respectively.

Inspired by the above results of the hydrolysis and rapid enzymatic degradation of PEG-PLA, the biodegradability of the PEG-PLA copolymer and PLA homopolymers were further evaluated in seawater collected from Osaka Bay using the BOD analysis. In the standardized test set-up, aniline was used as a reference owing to its well-characterized biodegradation profile. The validity of the experimental approach against the OECD 306 [55] and ISO 18830:2016 [56] would be confirmed when the biodegradation tests conducted under these conditions yielded a half-life (t_{50}) of aniline of approximately 2–12 d and a final degradation rate of approximately 80%, which is direct evidence of the biodegradability level of the target materials [57,58]. As shown in the curve for aniline degradation shown in **Fig. 1-10a**, the validity of the test results was verified based on the above theoretical considerations.

The corresponding test results are also shown in **Fig. 1-10a**. After 3 d, in addition to neat PLA-*h*, the consumption of O_2 started to increase gradually. Further, the biodegradation rate increased significantly after approximately 13 d. After 28 d, the biodegradation rates of $PEG_{4k}PLA_{2k}$-*r*, $PEG_{4k}PLA_{3k}$-*r*, $PEG_{4k}PLA_{2k}$-*a,* and $PEG_{4k}PLA_{3k}$-*a* were 72.63%, 65.47%, 60.61%, and 53.11%, respectively, which revealed that PEG-PLA was readily biodegradable in marine environments [59]; these results also markedly exceeded that of neat PLA-*h*. PEG-PLA, with a disordered structure and shorter PLA chain segments, showed a faster degradation t_{50} and higher biodegradation performance, which could be attributed to its lower crystallinity and higher hydrophilicity. The $PEG_{4k}PLA_{2k}$ copolymer with higher hydrophilicity also showed higher sensitivity in the initial stage of the degradation test (**Fig. 1-10b**). The degradation behavior was related to the Tris-HCl buffer and enzyme solutions, as described above. In addition, I compared the losses before and after degradation for all samples (**Fig. 1-11**). These results were consistent with the biodegradation performance,

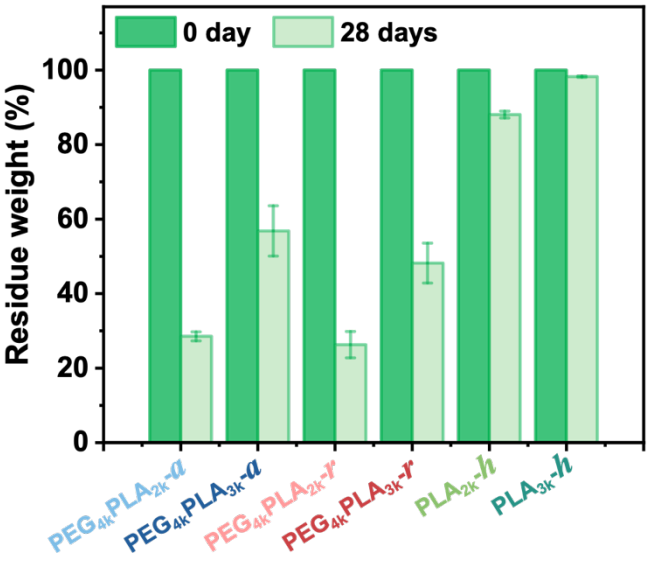

Fig. 1-11. Residue weight of all samples after 28 days of seawater biodegradation.

especially the weight loss of $PEG_{4k}PLA_{2k}$-*a*, which was 71.5%. **Fig. 1-10(c,d)** show the corresponding macroscopic and microscopic changes before and after the degradation of the samples, respectively. These results are consistent with the weight loss results, indicating that the improvement in the seawater biodegradation of PLA by the introduction of PEG was significant. Regarding the changes in M_n, it is evident from **Fig. 1-10e** that the retention time of PEG-PLA drastically increased with low M_n after 28 d of biodegradation in seawater. The signal of the random structure changed from a single peak to a triple peak because of the less regularity of the chain segments caused by the random copolymerization. The corresponding data are listed in **Table 1-6**. For example, the M_n of $PEG_{4k}PLA_{3k}$-*a* was reduced from 53,765 to 8733 g mol^{-1}, while *Đ* decreased from 1.48 to 1.11. This further demonstrates that introducing PEG as a hydrophilic group into the backbone of PLA can improve its seawater biodegradability.

Table 1-6 The compositions and molecular weight changes of PEG-PLA copolymers, and PLA homopolymers before and after seawater degradation

Samples	Original state					Seawater biodegradation 28 days later				
	F^a (wt%)			M_n (g/mol) (GPC)	M_w/M_n *Đ* (GPC)	F^a (wt%)			M_n (g/mol) (GPC)	M_w/M_n *Đ* (GPC)
	F_{PEG}	F_{PLA}	F_{HDI}			F_{PEG}	F_{PLA}	F_{HDI}		
$PEG_{4k}PLA_{2k}$-*a*	51.66	46.18	2.16	91380	1.56	91.95	8.05	0	6917	1.12
$PEG_{4k}PLA_{3k}$-*a*	41.62	55.63	2.75	53765	1.48	56.62	43.38	0	8733	1.11
$PEG_{4k}PLA_{2k}$-*r*	51.05	42.01	6.94	71684	1.58	73.2	22.72	4.48	*23642*	*1.06*
									9970	*1.06*
									3718	*1.09*
$PEG_{4k}PLA_{3k}$-*r*	40.97	53.72	5.31	61342	1.51	53.31	43.57	3.12	*20156*	*1.08*
									8944	*1.03*
									3451	*1.03*
PLA_{2k}-*h*	-	94.35	5.65	69166	1.56	-	92.28	7.72	37408	1.65
PLA_{3k}-*h*	-	93.42	6.58	56276	1.44	-	93.01	6.99	41050	1.81

a Indicates that it is calculated from ^{1}H NMR.

To understand the structure and composition, thermal properties, changes in thermal stability after degradation, and degradation mechanism of PEG-PLA, $PEG_{4k}PLA_{3k}$-*a,* and $PEG_{4k}PLA_{3k}$-*r* are considered as examples, FT-IR and ^{1}H NMR were carried out, and the detailed data are summarized in **Table 1-6**. In addition, there was a higher weight loss in the

PLA component, causing severe degradation of the PLA chain segment from the side in seawater. Further, FT-IR was used to characterize changes in the functional groups of PEG-PLA (**Fig. 1-10f**). A distinct terminal hydroxyl peak appeared at 3391 cm^{-1} (the end and intramolecular ester exchange reaction of PLA resulted in increased -OH end groups) [52]. An overlapping peak corresponding to the stretching vibration of the amino group was observed at 3238 cm^{-1}. The carbonyl peak at 1750 cm^{-1} split into two stretching vibration peaks, and a new peak appeared at 1645 cm^{-1}, confirming the presence of free carboxyl groups after degradation. The disappearance of the bending vibration peak corresponding to the amide bond at 1533 cm^{-1} indicates that the ester and amide bonds that serve as the attack sites of water molecules were destroyed during the seawater degradation process, and the PEG-PLA bioplastic was rapidly degraded. In addition, as shown in **Fig. 1-10g**, the protons on the PEG methylene groups in the copolymer (***d***) were used as a reference to observe the change in the proton content of the PLA methine groups (***a***). The intensity ratio $\boldsymbol{I_d/I_a}$ of EG/LA changes from 5.17 to 8.34 and 5.49 to 9.85, respectively, implying that the PLA chain segments preferentially hydrolyzed in seawater. In contrast, the higher increase in the random copolymer suggested that it was readily degraded, consistent with the results comparing the biodegradation properties and residual weight described above. This is consistent with the report by Feng et al. that during the degradation of poly(3-hydroxybutyrate-co-3-hydroxyvalerate), the amorphous region of the copolymer began to degrade first, followed by the crystalline region [60]. It can be seen in **Fig. 1-10h** that both alternating and random PEG-PLA had a sharp drop in their thermal stability after suffering from seawater degradation. The $T_{d,\ max}$ of the PLA segment decreased by approximately 80 °C. Numata et al. identified that altering the ratios of the incorporated components in the copolymer chain affected their crystallinity and degradation rate [61]. Similarly, for $PEG_{4k}PLA_{3k}$-*a*, the PLA crystallization peak appeared in the DSC cooling curve after degradation, and the ΔH_m corresponding to the melting peak increased from 4.87 to 19.75 J g^{-1}. While both the T_c and T_m of the PEG decreased, ΔH_c and ΔH_m increased, which suggests that after degradation, the molecular chains of the residue product were shorter. The mutual restriction between PEG and PLA weakened, allowing the latter to rearrange to increase the crystallinity. This implies that the degradation of seawater destroyed the chemical structure of PEG-PLA and modified its crystallization behavior.

Table 1-7 presents comprehensive data on the thermal properties. Combining the stability of the chemical structure, microstructure, and M_n changes after soaking the material in DIW at 22 ± 0.5 °C for 6 months further demonstrates that incorporating PEG enhances the biodegradability of PLA in marine environments. **Fig. 1-12a** presents a schematic of the

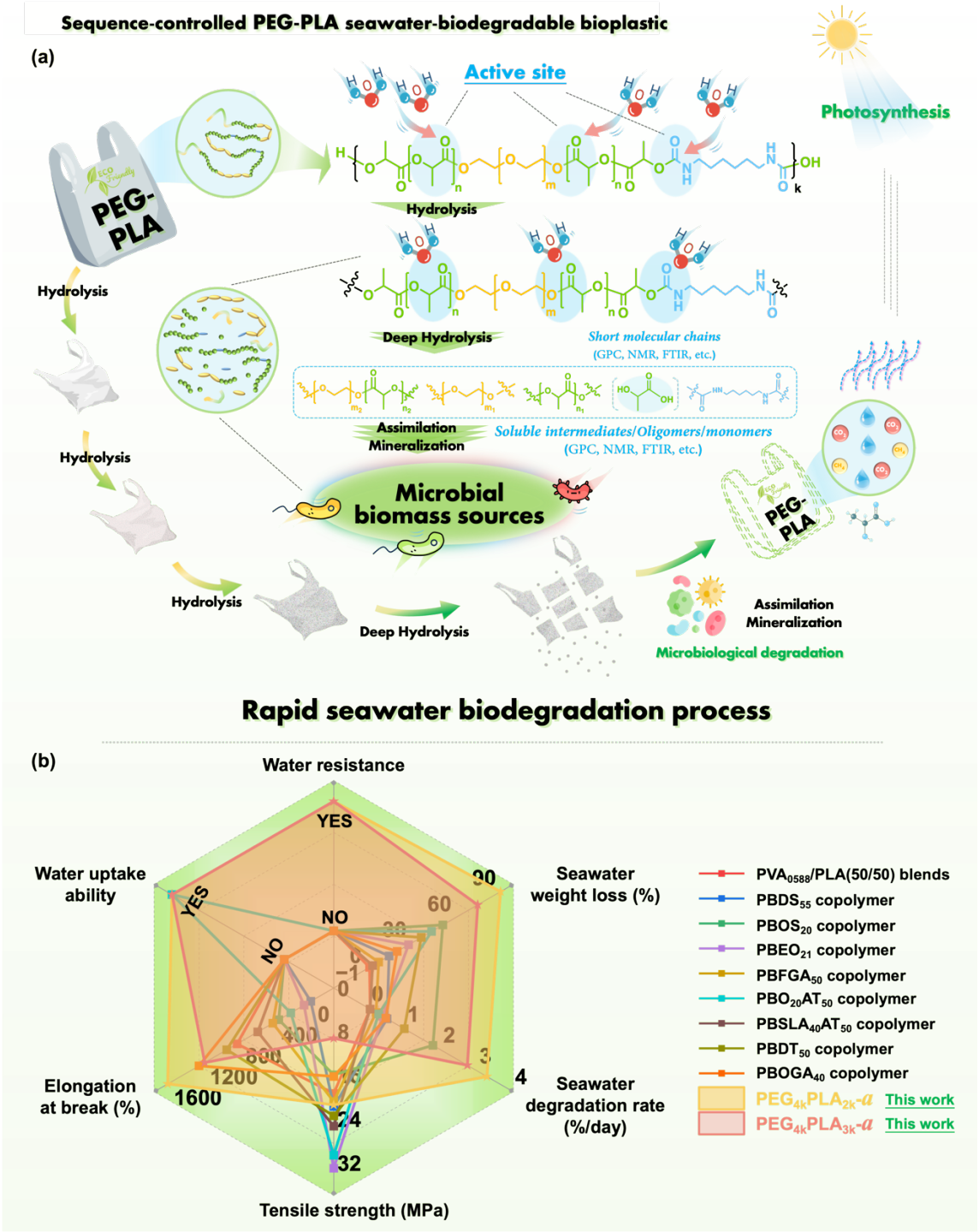

Fig. 1-12. (a) The proposal schematic illustration of the seawater degradation mechanism of PEG-PLA copolymers. (b) Comparison of the toughness, strain, water uptake ability, water durability, seawater weight loss, and seawater degradation rate with current research.

hypothesized marine biodegradation mechanism for PEG-PLA copolymers [62,63]. The added PEG units in the PLA chain expand the interaction area between the ester and amide bonds and water molecules. This promotes the hydrogen bonding that accelerates the nucleophilic attack of water in marine environments with low temperatures, limited microorganisms, and high salinity. Consequently, this leads to an effectively tunable biodegradation rate of PEG-PLA containing varying EG/LA ratios. The superior overall performance of the PEG-PLA copolymers with elaborate alternating structures is demonstrated compared to reported marine-degradable polyesters [17,64–71] shown as radar plots (**Fig. 1-12b)**. The alternating PEG-PLA structure provides an outstanding marine biodegradation rate, has excellent stretchability both in wet and dry states, and shows simple, cost-effective manufacturing processes suitable for scaling up, making it a favorable alternative for marine-biodegradable polymers

Table 1-7 The thermal parameters of PEG-PLA copolymers after seawater biodegradation

Samples	Seawater biodegradation 28 days later												
	DSC											TGA (°C)	
		PEG					PLA						
	T_g[a] (°C)	T_c (°C)	ΔH_c (J g^{-1})	T_m (°C)	ΔH_m (J g^{-1})	X_c[c] (%)	T_c (°C)	ΔH_c (J g^{-1})	T_m (°C)	ΔH_m (J g^{-1})	X_c (%)	PLA	PEG
PEG$_{4k}$PLA$_{2k}$-*a*	–12.1	34.4[b]	6.84[b]	52.5	6.73	3.72	82.8	4.82	103.3	3.98	53.16	194.3	356.8
PEG$_{4k}$PLA$_{3k}$-*a*	-[d]	12.1[b]	28.70[b]	68.6	29.81	26.75	35.3	19.24	121.4	19.75	48.95	204.9	346.1
PEG$_{4k}$PLA$_{2k}$-*r*	3.4	-[d]	-[d]	-[d]	-[d]	-[d]	91.5	1.97	112.6	2.24	10.60	203.1	377.4
PEG$_{4k}$PLA$_{3k}$-*r*	2.2	50.1[b]	0.88[b]	69.7	0.91	0.9	87.8	5.33	109.2	6.09	15.03	208.9	341.6
PLA$_{2k}$-*h*	-[d]	-[d]	-[d]	-[d]	-[d]	-[d]	-[d]	-[d]	-[d]	-[d]	-[d]	-[d]	-[d]
PLA$_{3k}$-*h*	-[d]	-[d]	-[d]	-[d]	-[d]	-[d]	-[d]	-[d]	-[d]	-[d]	-[d]	-[d]	-[d]

[a] Obtained from the second heating scan.

[b] Cold crystallization temperature and enthalpy obtained from the heating scan.

[c] X_c was calculated by the $\Delta H^0_{m,\,PEG,}$ and $\Delta H^0_{m,\,PLA}$ of 196.8 J g^{-1} and 93.0 J g^{-1}, respectively.

[d] No thermal transition was detected.

1.4 Conclusions

This chapter proposed the design of sequence-controlled PEG-PLA copolymer bioplastics with exceptional durability in DIW and rapid, tunable biodegradability in marine environments. The PEG-PLA copolymers were synthesized by ROP and coupling techniques with PLA and PEG as building blocks, achieving M_n exceeding 5.3×10^4 g mol^{-1}. The impact of the PEG content on the properties of PLA-based bioplastics was investigated. PEG-PLA exhibited tunable hydrophilicity (WAC from 80.9° ± 2.3° to 38.3° ± 7.2°) and water absorption (180.22% ± 0.21% to 5.11% ± 0.17%). $PEG_{4k}PLA_{2k}$-*a* presented excellent mechanical properties in both wet and dry states, with a maximum elongation at break and strength of 1446.8% ± 89.9% and 8.3 ± 2.1 MPa, respectively. The introduction of PEG increased the flexibility of the PLA molecular chain, reducing T_g from 50.4 °C to –42.5 °C. With its well-organized chain structure, the alternating structure exhibited a lower T_g and stable rheological properties suitable for processing. In addition, PEG-PLA showed enhanced biodegradability with the incorporated PEG; $PEG_{4k}PLA_{2k}$ was biodegraded entirely in 120 h, even at a low proteinase K concentration of 0.0125 g mol^{-1}. The degradation mechanism prioritized the PLA segments within the PEG-PLA copolymer, as confirmed by comprehensive characterization techniques, including FT-IR, ^{1}H NMR, SEM, and GPC. The biodegradability by the OECD 306 reached 72.63%, as verified by quantitative 28-day BOD analysis. This proves that bioplastic has the potential for rapid chain scission in marine environments. Consequently, this chapter illustrated the trade-offs between PEG as a building unit in modifying PLA regarding thermal behavior, mechanical properties, DIW durability, and marine biodegradability. Elaborate PEG-PLA bioplastics can shed light on developing the next generation of tunable, fast marine-biodegradable, and renewable high-performance green materials for packaging, medical, and agricultural applications and address marine plastic pollution.

1.5 References

[1] J. R. Jambeck, R. Geyer, C. Wilcox, T. R. Siegler, M. Perryman, A. Andrady, R. Narayan, K. L. Law, *Science* **2015**, *347*, 768.

[2] A. C. Albertsson, M. Hakkarainen, *Science* **2017**, *358*, 872.

[3] X. Lim, *Nature* **2021**, *593*, 22.

[4] W. Huang, B. Song, J. Liang, Q. Niu, G. Zeng, M. Shen, J. Deng, Y. Luo, X. Wen, Y. Zhang, *J. Hazard. Mater.* **2021**, *405*, 124187.

[5] D. Luo, X. Chu, Y. Wu, Z. Wang, Z. Liao, X. Ji, J. Ju, B. Yang, Z. Chen, R. Dahlgren, M. Zhang, X. Shang, *J. Hazard. Mater.* **2024**, *465*, 133412.

[6] B. Worm, H. K. Lotze, I. Jubinville, C. Wilcox, J. Jambeck, *Annu. Rev. Environ. Resour.* **2017**, *42*, 1.

[7] M. Haward, *Nat. Commun.* **2018**, *9*, 667.

[8] L. Manfra, V. Marengo, G. Libralato, M. Costantini, F. De Falco, M. Cocca, *J. Hazard. Mater.* **2021**, *416*, 125763.

[9] M. Karamanlioglu, R. Preziosi, G. D. Robson, *Polym. Degrad. Stab.* **2017**, *137*, 122.

[10] J. Yu, S. Xu, B. Liu, H. Wang, F. Qiao, X. Ren, Q. Wei, *Eur. Polym. J.* **2023**, *193*, 112076.

[11] G. X. Wang, D. Huang, J. H. Ji, C. Völker, F. R. Wurm, *Adv. Sci.* **2021**, *8*, 2001121.

[12] A. R. Bagheri, C. Laforsch, A. Greiner, S. Agarwal, *Global Challenges* **2017**, *1*, 1700048.

[13] T. P. Haider, C. Völker, J. Kramm, K. Landfester, F. R. Wurm, *Angew. Chem., Int. Ed.* **2019**, *58*, 50.

[14] H. Sun, Y. Liang, M. P. Thompson, N. C. Gianneschi, *Prog. Polym. Sci.* **2021**, *120*, 101427.

[15] C. J. Stubbs, J. C. Worch, H. Prydderch, Z. Wang, R. T. Mathers, A. V. Dobrynin, M. L. Becker, A. P. Dove, *J. Am. Chem. Soc.* **2022**, *144*, 1243.

[16] C. Hu, X. Pang, X. Chen, *Macromolecules* **2022**, *55*, 1879.

[17] D. Huang, Z. D. Hu, T. Y. Liu, B. Lu, Z. C. Zhen, G. X. Wang, J. H. Ji, *e-Polymers* **2020**, *20*, 759.

[18] G. Chen, L. Xu, P. Zhang, B. Chen, G. Wang, J. Ji, X. Pu, Z. L. Wang, *Adv. Mater. Technol.* **2020**, *5*, 2000455.

[19] H. J. Kim, M. A. Hillmyer, C. J. Ellison, *J. Am. Chem. Soc.* **2021**, *143*, 15784.

[20] W. Xu, C. Ma, J. Ma, T. Gan, G. Zhang, *ACS Appl. Mater. Interfaces* **2014**, *6*, 4017.

[21] S. Wang, K. A. Lydon, E. M. White, J. B. I. Grubbs, E. K. Lipp, J. Locklin, J. R. Jambeck, *Environ. Sci. Technol.* **2018**, *52*, 5700.

[22] T. Rheinberger, J. Wolfs, A. Paneth, F. Wurm et al., *J. Am. Chem. Soc.* **2021**, *143*, 15673.

[23] K. W. Meereboer, M. Misra, A. K. Mohanty, *Green Chem.* **2020**, *22*, 5519.

[24] K. Saravanan, M. Umesh, P. Kathirvel, *J. Polym. Environ.* **2022**, *30*, 4903.

[25] A. A. D'souza, R. Shegokar, *Expert Opin. Drug Deliv.***2016**, *13*, 1257.

[26] T. Wolf, T. Steinbach, F. Wurm, *Macromolecules* **2015**, *48*, 3853.

[27] J. G. Rosenboom, R. Langer, G. Traverso, *Nat. Rev. Mater.* **2022**, *7*, 117.

[28] R. Z. Xiao, Z. W. Zeng, G. L. Zhou, J. J. Wang, F. Z. Li, A. M. Wang, *Int. J. Nanomedicine* **2010**, *5*, 1057.
[29] K. Ulbrich, K. Holá, V. Šubr, A. Bakandritsos, J. Tuček, R. Zbořil, *Chem. Rev.* **2016**, *116*, 5338.
[30] S. B. Shabat, N. Kumar, A. J. Domb, *Macromol. Biosci.* **2006**, *6*, 1019.
[31] M. He, Y. I. Hsu, H. Uyama, *Appl. Mater. Today* **2024**, *36*, 102057.
[32] J. Liu, B. Mattiasson, *Water Res.* **2002**, *36*, 3786.
[33] D. F. Williams, *Eng. Med.* **1981**, *10*, 5.
[34] M. S. Reeve, S. P. McCarthy, M. J. Downey, R. A. Gross, *Macromolecules* **1994**, *27*, 825.
[35] E. M. Garland; P. Tozzolino; E. Dutrieux, SPE Int. Conf. Heal. Saf. Environ. Oil Gas Explor. Prod. **1998**.
[36] K. Kasuya, K. Takagi, S. Ishiwatari, Y. Yoshida, Y. Doi, *Polym. Degrad. Stab.* **1998**, *59*, 327.
[37] M. J. He, W. X. Xiao, H. Xie, C. J. Fan, L. Du, X. Y. Deng, K. K. Yang, Y. Z. Wang, *Mater. Chem. Front.* **2017**, *1*, 343.
[38] Y. Du, X. Liu, X. Dong, Z. Yin, *Comput. Struct. Biotechnol. J.* **2022**, *20*, 975.
[39] S. Saeidlou, M. A. Huneault, H. Li, C. B. Park, *Prog. Polym. Sci.* **2012**, *37*, 1657.
[40] B. Imre, B. Pukánszky, *Eur. Polym. J.* **2013**, *49*, 1215.
[41] L. Jia, W. C. Zhang, B. Tong, R. J. Yang, *Chin. J. Polym. Sci.* **2018**, *36*, 871.
[42] J. S. Lee, M. Taghavimehr, R. Montazami, M. D. Green, *Polymer* **2022**, *242*, 124543.
[43] W. Hoogsteen, A. R. Postema, A. J. Pennings, G. Ten Brinke, P. Zugenmaier, *Macromolecules* **1990**, *23*, 634.
[44] M. L. Arnal, S. Boissé, A. J. Müller, F. Meyer, J. M. Raquez, P. Dubois, R. E. Prud`homme, *CrystEngComm* **2016**, *18*, 3635.
[45] K. Pielichowska, M. Nowak, P. Szatkowski, B. Macherzyńska, *Appl. Energy* **2016**, *162*, 1024.
[46] E. W. Fischer, H. J. Sterzel, G. Wegner, *K. Z.u.Z. Polymere* **1973**, *251*, 980.
[47] R. J. Mondschein, J. M. Dennis, H. Liu, R. K. Ramakrishnan, S. Nazarenko, S. R. Turner, T. E. Long, *Macromolecules* **2017**, *50*, 7603.
[48] N. M. Ahmad, P. A. Lovell, S. M. Underwood, *Polym. Int.* **2001**, *50*, 625.
[49] C. C. Huang, M. X. Du, B. Q. Zhang, C. Y. Liu, *Macromolecules* **2022**, *55*, 3189.
[50] F. Kawai, K. Nakadai, E. Nishioka, H. Nakajima, H. Ohara, K. Masaki, H. Iefuji, *Polym. Degrad. Stab.* **2011**, *96*, 1342.
[51] H. Tsuji, S. Miyauchi, *Biomacromolecules* **2001**, *2*, 597.
[52] D. Macocinschi, D. Filip, M. F. Zaltariov, C. D. Varganici, *Polym. Degrad. Stab.* **2015**, *121*, 238.
[53] A. Magnin, E. Pollet, V. Phalip, L. Avérous, *Biotechnol. Adv.* **2020**, *39*, 107457.
[54] K. Yamashita, Y. Kikkawa, K. Kurokawa, Y. Doi, *Biomacromolecules* **2005**, *6*, 850.
[55] A. Ott, T. J. Martin, G. F. Whale, J. R. Snape, B. Rowles, M. G. Burgos, R. J. Davenport,

Sci. Total Environ. **2019**, *666*, 399.
[56] The British Standards Institution (BSI). **2016** BS ISO 18830:2016 Plastics. *Method by measuring the oxygen demand in closed respirometer*, pp. 1–18. London, UK: BSI.
[57] U. Strotmann, P. Reuschenbach, U. Pagga, *Appl. Environ. Microbiol.* **2004**, *70*, 4621.
[58] A. Nakayama, N. Yamano, N. Kawasaki, *Polym. Degrad. Stab.* **2019**, *166*, 290.
[59] S. López-Ibáñez, R. Beiras, *Sci. Total Environ.* **2022**, *831*, 154860.
[60] L. Feng, Y. Wang, Y. Inagawa, K. Kasuya, T. Saito, Y. Doi, Y. Inoue, *Polym. Degrad. Stab.* **2004**, *84*, 95.
[61] K. Numata, Y. Kikkawa, T. Tsuge, T. Iwata, Y. Doi, H. Abe, *Biomacromolecules* **2005**, *6*, 2008.
[62] M. Hakkarainen, In *Degradable Aliphatic Polyesters*, Springer, Berlin, Heidelberg, **2002**, pp. 113–138.
[63] S. Inkinen, M. Hakkarainen, A. C. Albertsson, A. Södergård, *Biomacromolecules* **2011**, *12*, 523.
[64] T. Zhu, L. Wang, Y. Lu, Z. Wei et al. *J. Hazard. Mater.* **2024**, *46*, 132791.
[65] T. Liu, D. Huang, P. Xu, B. Lu, Z. Zhen, G. Wang, J. Ji, *e-Polymers* **2022,** *22*, 615.
[66] Q. Luan, H. Hu, X. Jiang, C. Lin, X. Zhang, Q. Wang, Y. Dong, J. Wang, J. Zhu, *J. Hazard. Mater.* **2023**, *457*, 131801.
[67] Y. Ding, D. Huang, T. Ai, C. Zhang, Y. Chen, C. Luo, Y. Zhou, B. Yao, L. Dong, X. Du, J. Ji, *ACS Sustain. Chem. Eng.* **2021**, *9*, 1254.
[68] Q. Luan, H. Hu, X. Ouyang, X. Jiang, C. Lin, H. Zhu, T. Shi, Y. L. Zhao, J. Wang, J. Zhu, *J. Hazard. Mater.* **2024**, *465*, 133475.
[69] T. Y. Liu, D. Huang, P. Y. Xu, B. Lu, G. X. Wang, Z. C. Zhen, J. Ji, *ACS Sustain. Chem. Eng.* **2022**, *10*, 3191.
[70] Y. Tian, H. Hu, C. Chen, F. Li, W. Bin Ying, L. Zheng, J. Wang, R. Zhang, J. Zhu, *Chem. Eng. J.* **2022**, *447*, 137535.
[71] H. Hu, J. Li, Y. Tian, C. Chen, F. Li, W. B. Ying, R. Zhang, J. Zhu, *ACS Sustain. Chem. Eng.* **2021**, *9*, 3850.

Chapter 2. Design of novel poly(L-lactide)-based shape memory multiblock copolymers for biodegradable esophageal stent application

2.1 Introduction

Esophageal cancer ranks among the deadliest cancers globally owing to its highly malignant nature, with a 5-year survival rate of just 10% [1] and is the 8th most common and 6th most fatal malignancy [2,3]. Current treatment strategies for patients with advanced esophageal cancer and severe esophageal strictures often involve stent implantation [4]. Conventional stents, predominantly comprising metal alloys or metal alloys coated with polymers, present drawbacks such as non-degradability, tissue trauma, potential rejection by the body [5–9], and the need for a balloon for stent deployment [10]. It is also difficult to degrade, adjust, or remove them after performing their intended functions [11,12]. Furthermore, conventional stents lack sustained effectiveness in inhibiting tumor growth and inflammation [13]. Therefore, it is necessary to explore new esophageal stents to circumvent the need for repeated dilation or surgery in patients [1]. For example, biodegradable polymer stents [14,15] can prevent or unblock esophageal strictures in a certain period with mechanical support and non-toxic side effects through complete biodegradation without extra operation after they perform the desired function. Thus, the complications of removal stent, tissue ingrowth, and migration would be decreased.

Furthermore, the shape memory effect (SME) can be utilized to achieve easier stent implantation. Shape memory polymers (SMPs), as smart materials [16], exhibit the capability to recover their original shape after undergoing temporary shape programming upon exposure to an external stimulus such as temperature [17], water [18], light [19], and other stimuli [20–23]. In recent years, biodegradable SMPs have shown promising potential in biomedical applications owing to their unique properties [24,25]. These applications include tissue engineering scaffolds [26], stents [4,27], and drug release systems [28,29]. Common triggers such as heat, UV light, electricity, and magnetism can pose risks to human health, necessitating additional safety measures. To overcome this, harnessing stimuli inherent to humans, such as physiological body temperature (~37 °C) and water (from biofluid environments), is advantageous. However, the

majority of SMPs are primarily thermo-responsive, with water-responsive variants being rare or synthesis processes for multi-responsive or multi-functional variants being complicated. This limits their functionality in biomedical applications. Thus, precise control over the transition temperatures (T_{trans}) of SMPs around 37 °C in a polymer with a simple chemical structure, a prerequisite for *in vivo* applications, still poses challenges. Because manipulating a single thermo-responsive effect cannot completely fulfill the complex practical needs of the human body, the fabrication of multifunctional SMPs is required for biomedical applications. Therefore, this study aimed to fabricate multi-functional SMPs, which will play a critical role in developing polymer design strategies at the molecular level. Physical crosslinking is the preferred approach in the design of SMPs because it utilizes intramolecular interactions. This effective strategy employs a linear multiblock thermoplastic polyester or polyether comprising two distinct domains to achieve phase separation. One of the domains functions as a molecular switch (soft segment) for the deformation of the temporary shape at temperatures higher and lower than T_{trans}, corresponding to lower melting temperatures (T_m) and glass transition temperatures (T_g). Another domain is the permanent crystalline network, which comprises net points (hard segments) with a high T_m or T_g to recover the original shape of the material [30].

Among the various bio-based polymers, many studies have investigated PLA as a stent material. These studies have mainly focused on understanding the straightforward elastic stress-strain characteristics [31], exploring elastic memory [32,33], and developing novel materials [34,35]. PLA exhibits SME, usually as a hard segment to hold the original shape. However, its direct use in the human body is hindered by its T_g of 55–65 °C [36]. The study undertaken by Wang *et al*. has provided evidence that the T_m of the PLA can be tuned to the desired range of 33–53 °C. This can be achieved by adjusting the M_n of PLA and the molar ratio between the soft and hard segments [37]. Also, some research has been reported when the M_n of PLA segments is very short, such as lower than 2000, the T_m of PLA showed lower than 100 ℃. In particular, PEG, serving as a molecular switch (soft segment), exhibits flexibility and hydrophilicity. In addition, its lower thermal T_{trans} can be adjusted to fall within the human tolerance range (26–60 °C) by manipulating its M_n [38]. When considering molecular design, due to copolymers often combine the best attributes of each polymer, their diverse chemical composition allows for the design of copolymers with tailored functionalities. Which makes them versatile for specific applications.

Thus, the hydrophilicity of the PEG segment plays a crucial role in conferring water sensitivity to the multiblock copolymer. The use of drug incorporation to enhance anti-inflammatory effects presents a potential challenge in esophageal stents. Yet, the hydrophilic nature of PEG may facilitate the drug loading process, provided that the drug molecule exhibits water solubility.

The copolymerization and blending of PLA and PEG to produce shape-memory materials has been widely reported. However, the emphasis is primarily on improving the shape memory capability of the materials or the tuning and design of T_{trans} [38]. However, to the best of our knowledge, no research has been conducted on PEG-PLA multiblock copolymers with simple linear structures that are biocompatible, regenerative, biodegradable, sensitive to body temperature and biofluids, can release drugs, and have superior flexibility and robust mechanical properties for use in esophageal stents.

In this chapter, a flexible and biodegradable multiblock copolymer exhibiting excellent shape recovery and elasticity is developed. Additionally, the multiblock copolymer possesses satisfactory mechanical properties and biocompatibility, crucial for various biomedical applications, particularly for treating esophageal strictures and esophageal cancer. Consequently, a simple strategic approach was employed and implemented, using the widely recognized PLA and PEG block copolymers to obtain a series of PLA-based multiblock copolymers. By introducing a hydrophilic PEG flexible segment as an initiator, a precise PLA-PEG-PLA structure was achieved through the ring-opening reaction. Subsequently, PEG-PLA multiblock copolymers were produced by coupling with HDI. These multiblock copolymers exhibit a wide range of T_{trans} (30.19–43.90 °C), covering the body temperature (37 °C). They demonstrated a wide range of WUR of 41% to 328% and satisfactory elongation at break (142.8% to 1920.6%) to enable shape recovery and fixing. Specifically, $PEG_{4k}PLA_{1.5k}$ displayed excellent body temperature-triggered (recovery rate reaching 99.5%) and water-triggered dual SME, which allowed it to perform as a shape memory multiblock copolymer stent (SMBS) in vitro implantation assessment. Localized and sustained drug delivery effectively suppressed pain and tumor growth surrounding the stent. Meanwhile, it displayed a distinct pH-dependent and simulated gastrointestinal biodegradability (stable in acid pH conditions). It helped it perform the desired function and then degraded gradually, highlighting its significant potential

in treating esophageal cancer.

2.2 Experimental Section

2.2.1 Materials

L-lactide (>98%) and 1,6-Hexamethylene diisocyanate (HDI; >98%) were purchased from Tokyo Chemical Industry Co., Ltd. (Tokyo, Japan). Poly(ethylene glycol) with number-average M_n (PEG, M_n = 2000 Da, 4000 Da, and 6000 Da, respectively, GR grade), diethyl ether (GR grade), chloroform (CH_3Cl, GR grade), toluene (Super Dehydrate, organic synthesis grade), Tin (II) 2-Ethylhexanoate ($Sn(Oct)_2$) (>95%), 0.1mol L^{-1} Phosphate Buffer Solution, pH 7.0, 1 mol L^{-1} Hydrochloric Acid, 1 mol L^{-1} Sodium Hydroxide Solution, Pepsin from porcine stomach, and trypsin from porcine pancreas were acquired from FUJIFILM Wako Pure Chemical Industries (Osaka, Japan). $Sn(Oct)_2$ was diluted with dry toluene and used as a

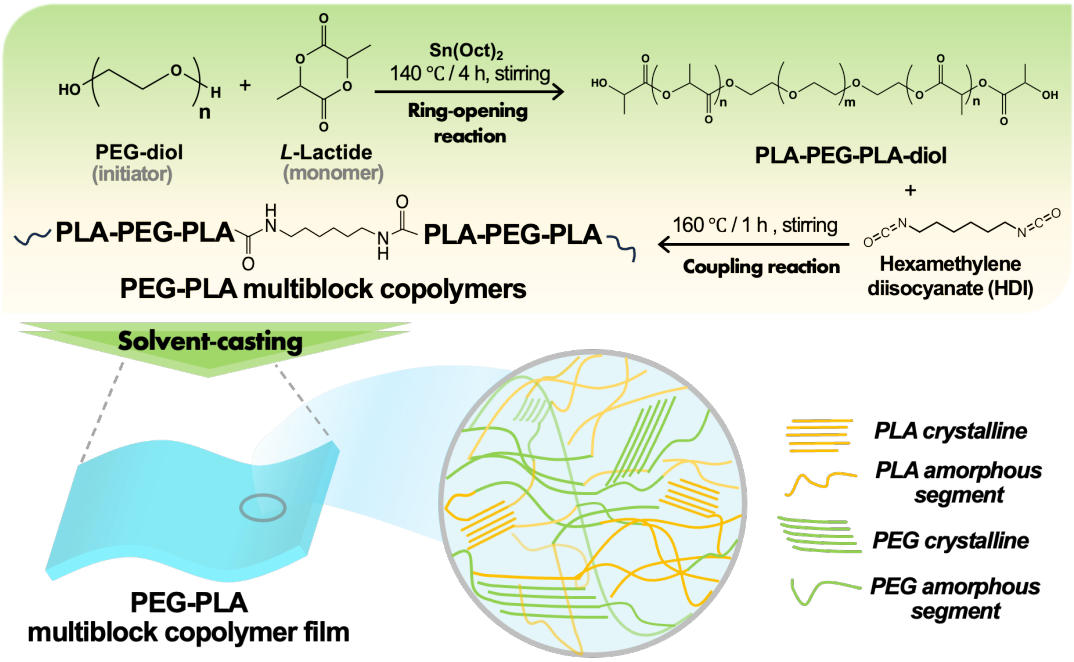

Scheme 2-1. Schematic of the synthetic route of the PEG-PLA multiblock copolymers.

solution (0.1 g mL^{-1}). All reagents were used as received. The obtained solution was stored in a glass volumetric flask under a nitrogen atmosphere. Milli-Q water was used for all experiments.

2.2.2 Preparation of PEG-PLA multiblock copolymer films

A series of PEG-PLA multiblock copolymers with varying compositions were *in situ* synthesized *via* a two-step bulk polymerization method, as shown in **Scheme 2-1**. The resulting products are denoted as PEG_xPLA_y, where the subscripts '*x*' and '*y*' represent the theoretical kinetic chain lengths of the respective polymers. For the detailed synthesis procedure please refer to the alternating sequence procedure in **Section 1.2.2** of **Chapter 1**.

2.2.3 Water uptake ratio of PEG-PLA multiblock copolymers

WUR tests were performed using Milli-Q water. Dry film samples (2 × 2 cm, five specimens) were initially weighed (W_d) and placed in water at 25 °C for specified durations (10, 60, and 120 min). Following immersion, the swollen samples were gently removed using tweezers, and excess water was removed before the samples were weighed (W_s). The WUR was calculated based on the initial weight of the dried film sample using **Eq. (2-1)**:

$$\textbf{WUR (\%)} = \frac{W_s - W_d}{W_d} \times 100\% \qquad \textbf{(2-1)}$$

The WUR calculations were performed in quintuplicate, and the average values were determined.

2.2.4 Degradation behaviors of PEG-PLA multiblock copolymers

2.2.4.1 Degradation at different pH conditions

The multiblock copolymers with diverse compositions were weighed (W_0) and immersed in PBS solution under varying pH conditions (pH = 2.0, 7.0, and 9.0) at 37 °C for 24 h to reach equilibrium swelling. Following incubation, the samples were carefully removed from the solutions, gently rinsed with distilled water, dried by lyophilization, and reweighed (W_t).

The degradation of multiblock copolymers was quantified using **Eq. (2-2)**:

$$\textbf{Remaining mass (\%)} = \frac{W_t}{W_0} \times 100\% \qquad \textbf{(2-2)}$$

The degradation tests were performed in triplicate, and the results were obtained as the mean and standard deviation.

2.2.4.2 In vitro static gastrointestinal degradation

Degradation behavior was characterized by immersion tests conducted in simulated fluids [39,40]. The multiblock copolymers were weighed (W_0) and then separately immersed in 25 mL of simulated gastric fluid (SGF, 0.1 mol L^{-1} PBS-HCl, pH 2.0) with pepsin (3 mg mL^{-1}) and simulated intestinal fluid (SIF, 0.1 mol L^{-1} PBS, pH 7.0) with trypsin (10 mg mL^{-1}) to evaluate their degradation behaviors at 37 °C. Freshly prepared pepsin and trypsin immersion media were replaced at different intervals to minimize the influence of pH changes and guarantee the stability of the enzymes. Also, new sterile containers were used for each replacement. After immersion, the samples were removed from the solution, gently rinsed with distilled water, withdrawn, lyophilized, and weighed again (W_t). The degradation of multiblock copolymers is defined by **Eq. (2-2)**. The degradation tests were performed in triplicate, and the average values were calculated.

2.2.5 Shape memory behavior of PEG-PLA multiblock copolymers

A schematic illustration of the SME is shown in **Fig. 2-1**. Typically, a stretching test was employed to investigate the shape memory properties of PEG-PLA multiblock copolymers.

The body temperature- and water-triggered SME was evaluated through a two-step process: (i) For the programming process, the sample was subjected to deformation at 37 °C (T_{high}) under applied force, followed by cooling to −20 °C (T_{low}) to fix a temporary shape B for 10 min. (ii) For the recovery process, the temperature was raised to 37 °C (T_{high}), thereby inducing the sample to recover from temporary shape B to the original shape A via body temperature triggering. Accordingly, immersion of the sample in water resulted in the recovery of the sample from temporary shape B to the original shape A, triggered by the presence of water. Corresponding, the average shape memory fixed rate (R_f) and response rate (R_r) were calculated using **Eq. (2-3)** and **(2-4)** [41,42]:

$$R_f = \frac{\varepsilon_{u\,(N)} - \varepsilon_{p\,(N-1)}}{\varepsilon_{m\,(N)} - \varepsilon_{p\,(N-1)}} \times 100\% \qquad (2\text{-}3)$$

$$R_r = \frac{\varepsilon_{u\,(N)} - \varepsilon_{p\,(N)}}{\varepsilon_{u\,(N)} - \varepsilon_{p\,(N-1)}} \times 100\% \qquad (2\text{-}4)$$

Here, $\varepsilon_{u\,(N)}$ refers to the strain present in the stress-free state after unloading the sample in the N^{th} cycle. At this point, the strain of the sample is denoted as the initial strain (ε_0). The sample was then subjected to appropriate tension to achieve the desired strain (ε_m). Following this, the sample was cooled to −20 °C while maintaining the applied stress to obtain the temporary strain (ε_m). Subsequently, the temperature was increased to 37 °C, and the stress was released (ε_u), allowing the sample to recover its original shape (ε_p) after isothermal incubation for 10 min. This cyclic process was repeated five times, and the values from the second to fifth cycles were recorded for analysis.

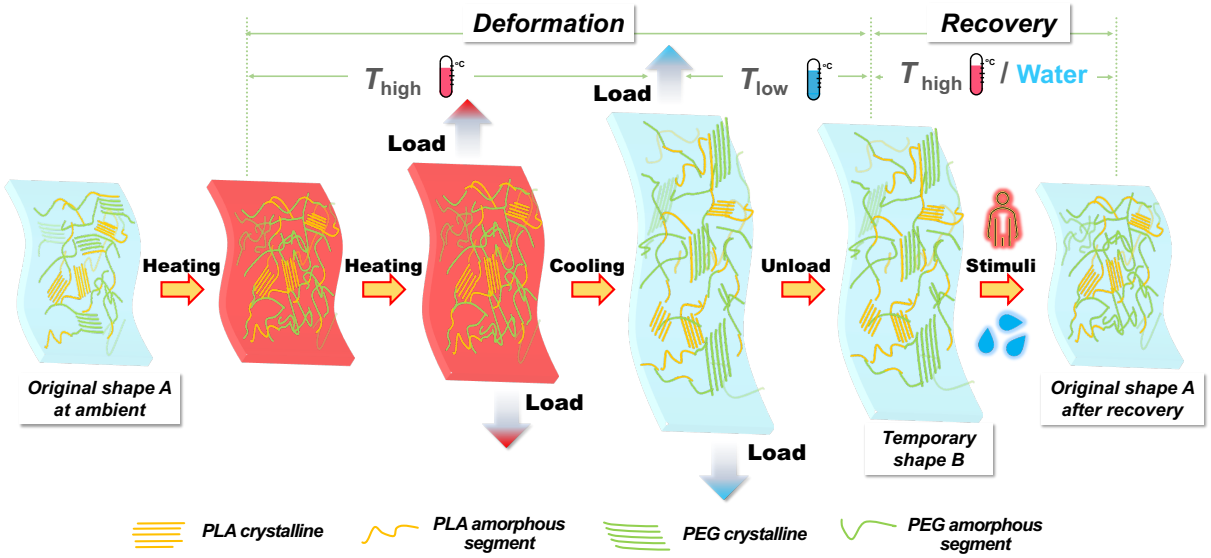

Fig. 2-1. Schematic illustration of SME (A: original shape; B: temporary shape).

2.2.6 Characterization and Measurements

For the characterization and measurements applied in this chapter please refer to **Section 1.2.6** of **Chapter 1**.

2.3 Results and Discussion

2.3.1 Preparation of PEG-PLA multiblock copolymer films

PLA-PEG-PLA-diol was synthesized through a typical ring-opening reaction of L-Lactide using PEG-diol as the initiator and $Sn(Oct)_2$ as the catalyst. The M_n of the copolymer was controlled by adjusting the feed ratio of *L*-Lactide/PEG-diol. As a result, copolymers with comparable molar masses containing hydroxyl groups at both ends were successfully obtained. The M_n of the PLA-PEG-PLA-diol and the conversion of L-lactide were calculated based on the areas of peaks corresponding to the –CH from the PLA repeat and the –CH derived from PEG, respectively, as shown in **Table 2-1**. Furthermore, the target product, the PEG-PLA multiblock copolymer, was obtained by coupling PLA-PEG-PLA-diol with HDI.

In detail, the M_n of the PLA-PEG-PLA-diol prepolymer, which contains two terminal hydroxyl groups, was prepared via a facile one-pot strategy, and its chemical structure was demonstrated by ^{1}H NMR spectrum. For more details on ^{1}H NMR spectrum, please refer to **Section 1.3.1** of **Chapter 1**. The M_n of PEG-PLA ranged from 48400 to 71900 g mol^{-1} and was evaluated by GPC, as shown in **Table 2-1**.

Table 2-1 The basic information of PLA-PEG-PLA-diol prepolymers and PEG-PLA multiblock copolymers

Samples	Ring-opening reaction PLA-PEG-PLA-diol prepolymers					Coupling reaction PEG-PLA multiblock copolymers	
	PEG-diol /M_n (g/mol)	L-Lactide /PEG (wt/wt)	L-Lactide Conversion (%)	M_n (g/mol) (theo.)	M_n (g/mol) (NMR)	M_n (g/mol) (GPC)	M_w/M_n PDI (GPC)
$PEG_{2k}PLA_{1k}$	2000	1.00/1	93.46	4000	3738	5.61×10^4	3.12
$PEG_{2k}PLA_{1.5k}$	2000	1.50/1	92.58	5000	4629	6.02×10^4	2.44
$PEG_{4k}PLA_{1k}$	4000	0.50/1	91.96	6000	5518	5.39×10^4	1.86
$PEG_{4k}PLA_{1.5k}$	4000	0.75/1	92.82	7000	6497	4.84×10^4	1.95
$PEG_{6k}PLA_{1.5k}$	6000	0.50/1	94.38	9000	8494	6.50×10^4	1.63
$PEG_{6k}PLA_{2k}$	6000	0.67/1	95.38	10000	9538	7.19×10^4	1.56

Moreover, the chemical structures of the obtained PLA-PEG-PLA-diol and PEG-PLA multiblock copolymers were further elucidated through FT-IR analysis (**Fig. 2-2**). The spectrum displayed all the characteristic absorptions corresponding to the PLA and PEG segments. Specifically, the absorption band at 1753 cm^{-1} was attributed to the C=O stretching band of the

PLA segment, with identified bending frequencies for the $–CH_3$ asymmetric and $–CH_3$ symmetric at 1458 and 1360 $cm^{–1}$, respectively. Furthermore, the –CH stretching vibration band and the ether stretching, assigned to the $–OCH_2CH_2–$ repeating units of PEG, were observed at 2879 and 1108 $cm^{–1}$, respectively. In **Fig. 2-2a**, the characteristic hydroxyl stretching bands of PLA-PEG-PLA-diol were evident around 3500 $cm^{–1}$, whereas they were absent in the spectrum of the PEG-PLA multiblock copolymer (**Fig. 2-2b**). Notably, the spectrum of the PEG-PLA (**Fig. 2-2b**) exhibited two distinct absorptions at 3326 $cm^{–1}$ and 1531 $cm^{–1}$, characteristic of the –NH unit in the urethane linkage. Thus, the successful preparation of the PEG-PLA multiblock copolymer is confirmed by these FT-IR observations, aligning with the previously mentioned ^1H NMR results.

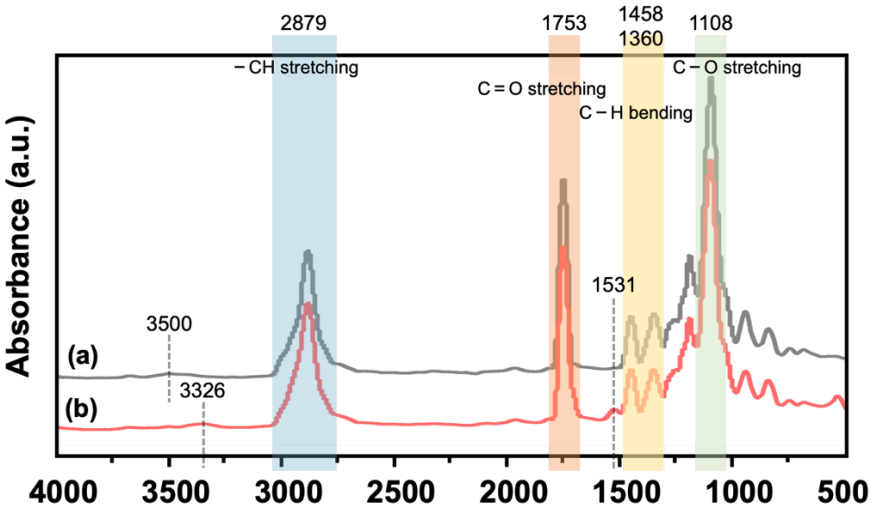

Fig. 2-2. The FT-IR spectrum of PLA-PEG-PLA-diol prepolymer (a) and PLA-PEG-PLA multiblock copolymer (b).

2.3.2 Thermal Behavior of PEG-PLA multiblock copolymers

DSC analysis was employed to study the thermal behavior of the PEG-PLA multiblock copolymers, which intrinsically dominated the thermally induced SME. **Fig. 2-3** shows the DSC curves of PEG-PLA with different feed ratios. Only the multiblock copolymers with sufficient crystallinity exhibited two distinct thermal transitions derived from the PEG and PLA phases. The T_c and T_m at low and high temperatures were assigned to the PEG and PLA phases, respectively, as illustrated in **Fig. 2-3** and **Table 2-2**. In detail, all PEG-PLA multiblock copolymers exhibited only one T_g from –29.70 °C to –14.60 °C, indicating that PLA and PEG segments are highly miscible in the amorphous domains. Interestingly, the T_m of PLA ranges from 68.90 °C to 86.80 °C, which is lower than the typical T_m of PLA (>100 °C). Based on the

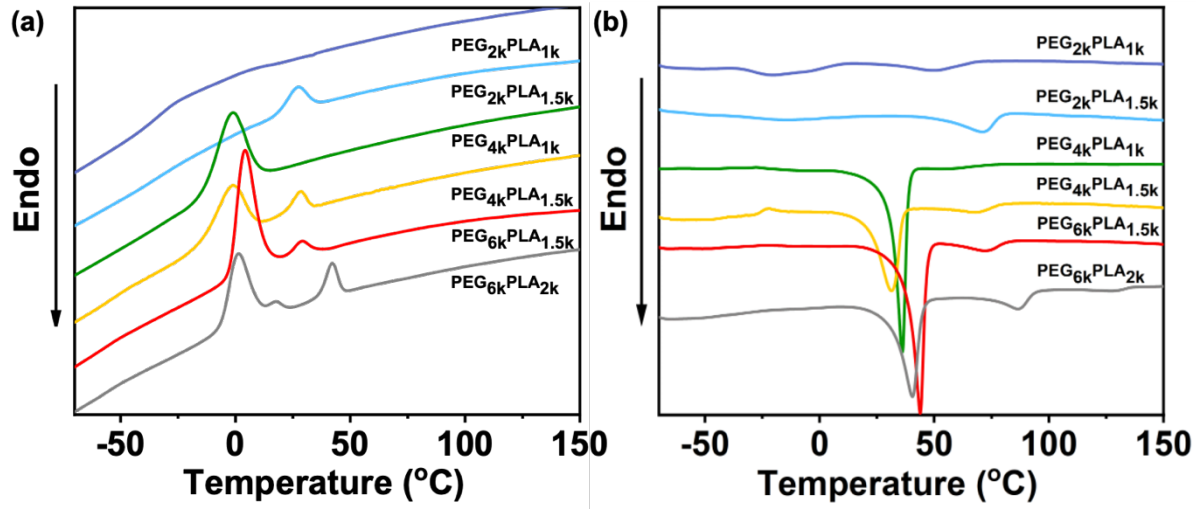

Fig. 2-3. DSC curves of PEG-PLA multiblock copolymers with various feed ratios in cooling scans (a) and heating scans (b).

literature [41–43], it was proposed that T_m downshift and melting peak widening occur when the molecular chain segments of PLA in the copolymer are very short. This contributes to them being restricted by the molecular chain segments of another phase, eventually affecting the crystallization process and mobility of PLA. For the sample with the PEG2000 segment, an increase in the PLA chain length resulted in a higher melting point of the multiblock copolymer. In addition, the crystallization properties of the PEG segments were influenced by the PLA segments because the PLA chains significantly constrained the chain mobility and arrangement of the short PEG chains. Consequently, this hindered the regularity and crystallinity of the PEG segments. However, forming a crystalline phase is challenging when the PLA chain length is below 1000 due to the presence of PEG disrupting the regularity of PLA chains. When the PLA chain length exceeds 1500, the copolymer shows enhanced crystallinity, and the melting point increases with increasing PLA chain length. When the PEG and PLA chain segment lengths exceed 4000 and 1500, respectively, they are both sufficient to form distinct crystal regions, indicating the presence of a specific phase separation structure, which is a prerequisite for the implementation of shape memory properties, as illustrated in **Fig. 2-3b**. However, only the T_m of the PEG phase (T_{trans} = 31.90 °C) and the PLA phase (68.90 °C) in $PEG_{4k}PLA_{1.5k}$ were measured to be lower and higher than 37 °C, respectively. This ensured the occurrence of PEG crystallization as the T_{trans} would exhibit sensitivity to human body temperature (T_{high} = 37 °C). In comparison, the PLA crystallization phase would remain relatively stable (more than 20 °C to T_{high}). In other words, this crystallization feature of $PEG_{4k}PLA_{1.5k}$ enables it to undergo a

thermally induced shape memory response triggered by the human body temperature.

In summary, the crystallization behavior of the PEG-PLA multiblock copolymer was influenced and could be modified by varying the feed ratio of PLA to PEG. From the perspective of the SME mechanism in this study, an appropriate PEG is crucial, as it not only provides sufficient crystallization to maintain the temporary shape but also affects the hydrophilicity of the multiblock copolymer and ultimately contributes to broader applications with desirable shape memory properties.

Table 2-2 Characteristic data of conventional DSC analysis

Samples	T_g [a] (°C)	PEG				PLA			
		T_c (°C)	ΔH_c (J g^{-1})	T_m (°C)	ΔH_m (J g^{-1})	T_c (°C)	ΔH_c (J g^{-1})	T_m (°C)	ΔH_m (J g^{-1})
$PEG_{2k}PLA_{1k}$	–29.70	-	-	54.60	6.94	-	-	-	-
$PEG_{2k}PLA_{1.5k}$	–27.30	-	-	-	-	27.70	10.90	71.50	7.83
$PEG_{4k}PLA_{1k}$	–14.60	2.00	41.90	36.40	45.60	-	-	-	-
$PEG_{4k}PLA_{1.5k}$	–17.80	–1.41	28.70	31.90	33.54	30.10	4.48	68.90	4.54
$PEG_{6k}PLA_{1.5k}$	–26.30	4.40	45.60	43.90	51.20	29.6	4.65	72.80	5.05
$PEG_{6k}PLA_{2k}$	–15.50	3.70	29.01	40.10	36.00	42.4	6.81	86.80	5.98

[a] Obtained from the second heating scan.

2.3.3 Optimal water durability of PEG-PLA multiblock copolymers

When considering the molecular design of polymers, the hydrophilicity of the PEG segment plays a crucial role in conferring water sensitivity to the multiblock copolymers. However, it should be noted that PEG-PLA possesses a linear molecular structure without chemical cross-linking, making it susceptible to dissolution upon excessive water absorption. Therefore, investigating the water durability of multiblock copolymers is imperative. The prepared PEG-PLA film was immersed in water for 2 h to evaluate wet durability. The WUR was calculated by measuring the weight of the dried and wet films. The results revealed that the WUR ranged from 41% ($PEG_{2k}PLA_{1.5k}$) to 328% ($PEG_{4k}PLA_{1k}$) and was significantly affected

by the PEG segment content. As depicted in **Fig. 2-4a**, the water uptake ability of the multiblock copolymers decreased gradually as the hydrophobic PLA chain segment content increased while the PEG chain segment content remained constant. However, when the PEG content varied, a noticeable change in the WUR was observed. For instance, as the PEG chain segments increased from 2000 to 4000, the WUR of the films increased approximately fourfold.

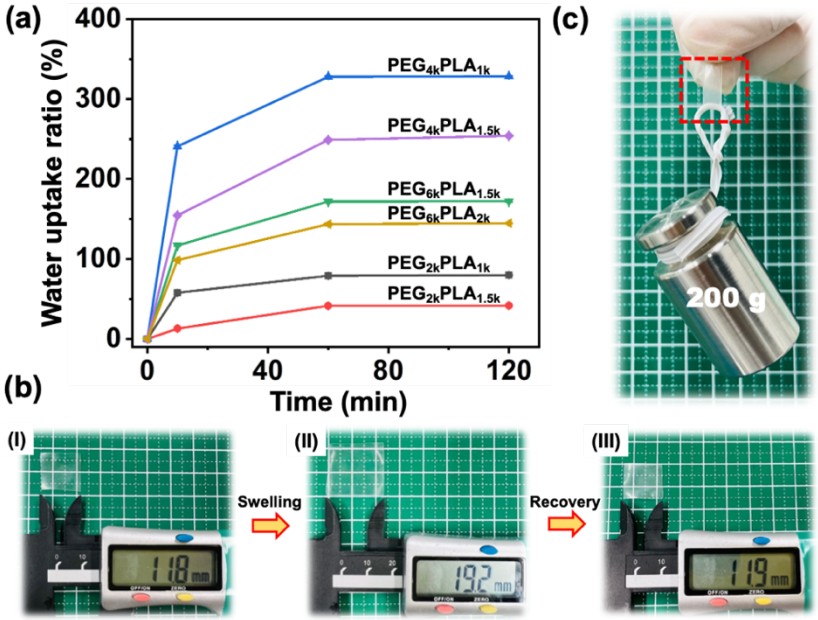

Fig. 2-4. (a) WUR of PEG-PLA multiblock copolymer films with various feed ratios (b) (I) $PEG_{4k}PLA_{1.5k}$ film, (II) after being immersed in water and (III) dried in the oven at 37 °C several times (employed to carry out the water durability experiments) (c) Digital photos demonstrating that the $PEG_{4k}PLA_{1.5k}$ film could withstand 200 g of weight.

In contrast, the film with PEG6000 exhibited a decreased WUR. This phenomenon can be attributed to the increased crystallization ability of the growing PEG chain segments, which hinders the chain segment mobility and restricts the free diffusion of water molecules within the limited molecular space. However, it should be noted that the $PEG_{4k}PLA_{1k}$ film, which displayed the highest WUR, completely dissolved in water after approximately 4 h of immersion, rendering it unsuitable for further applications. Based on these findings, the $PEG_{4k}PLA_{1.5k}$ film, which demonstrated a favorable balance between hydrophilicity and wet durability, was used for further experiments. The film was subjected to multiple water immersion cycles and subsequent drying in an oven at 37 °C. The results depicted in **Fig. 2-4b,c** confirm its excellent hydrophilicity and sufficient durability, contributing to its water-responsive shape memory properties.

2.3.4 Mechanical properties of PEG-PLA multiblock copolymers

The mechanical strength and elasticity of the PEG-PLA multiblock copolymers under both dry and wet conditions were evaluated using typical engineering stress-strain curves, as shown in **Fig. 2-5a,b**, respectively, which are essential for shape programming and load-bearing applications of SMPs. E, σ_m, and ε_b are presented in **Table 2-3**.

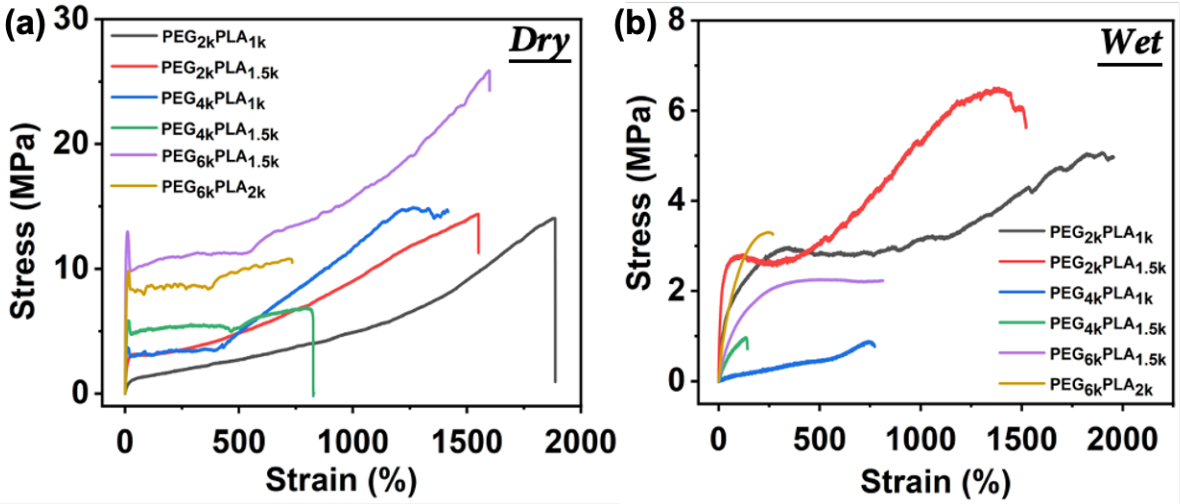

Fig. 2-5. Typical engineering stress-strain curves of PEG-PLA multiblock copolymers with various feed ratios in (a) dry and (b) wet conditions.

Under dry conditions, it is evident that the ε_b of all samples exceeds 700%, and the E increases from 6.4 to 242.3 MPa, which is sufficient for achieving the SME. Notably, the weight content of the PEG segments significantly affects the mechanical properties. The results demonstrate a transition from rubber-like behavior seen in soft PEG segments to plastic-like behavior reminiscent of PLA. As discussed in the previous DSC analysis, the PLA and the PEG segments were mostly amorphous, with low crystallization for $PEG_{2k}PLA_{1k}$. Consequently, compositions with appropriate proportions exhibit typical thermoplastic elastomer behaviors. Increasing the content of both the PEG and PLA segments enhanced the rigidity of the material. However, in the case of $PEG_{6k}PLA_{2k}$, both the PEG and PLA segments had sufficient crystallinity, resulting in mutual restriction and a decreased E and ε_b. In the wet state, the samples with high PEG content exhibited rubbery behavior owing to the absorption of water molecules, which facilitated the movement of chain segments and disrupted crystallization to some extent. Owing to the comparatively low WUR of PEG2000, the amount of water absorbed within the structure is limited. Instead, the flexibility of its chain segments is promoted, leading to a slight improvement in mechanical properties.

The results mentioned above indicate that the mechanical properties of the PEG-PLA multiblock copolymers are primarily governed by the PLA content. As the PEG segment chain length increases from 2000 to 6000 g mol^{-1}, multiblock copolymers exhibit a transition from rubber-like to plastic-like tensile properties; thus, they show the potential to undergo deformation at human body temperature, which is beneficial for achieving the SME.

Table 2-3 Mechanical properties of PEG-PLA multiblock copolymers in different conditions

Samples	Dried films			Wet films		
	Young's Modulus *E* (MPa)	Maximum Stress σ_m (MPa)	Elongation at break ε_b (%)	Young's Modulus *E* (MPa)	Maximum Stress σ_m (MPa)	Elongation at break ε_b (%)
$PEG_{2k}PLA_{1k}$	6.4 ± 0.3	14.1 ± 1.3	1864.1 ± 93.4	4.6 ± 0.1	5.1 ± 0.5	1920.6 ± 45.4
$PEG_{2k}PLA_{1.5k}$	28.6 ± 1.2	15.1 ± 0.5	1524.1 ± 25.3	15.1 ± 0.8	5.8 ± 0.5	1393.9 ± 51.8
$PEG_{4k}PLA_{1k}$	53.2 ± 1.6	15.0 ± 3.3	1216.2 ± 57.9	0.3 ± 0.1	0.9 ± 0.1	684.3 ± 42.4
$PEG_{4k}PLA_{1.5k}$	72.1 ± 3.5	6.5 ± 0.6	833.6 ± 62.9	1.1 ± 0.1	1.0 ± 0.1	142.8 ± 10.3
$PEG_{6k}PLA_{1.5k}$	242.3 ± 9.0	27.8 ± 0.4	1598.5 ± 37.1	1.8 ± 0.1	2.3 ± 0.1	485.2 ± 20.3
$PEG_{6k}PLA_{2k}$	149.4 ± 5.8	10.5 ± 0.5	796.2 ± 48.9	4.5 ± 0.3	3.1 ± 0.2	258.6 ± 8.3

2.3.5 Degradation behavior at different pH conditions of PEG-PLA multiblock copolymers

This chapter aims to develop a shape memory multiblock copolymer for potential biomedical applications. Thus, it is crucial to comprehensively understand their behaviors under different pH conditions. **Fig. 2-6** presents the results when the multiblock copolymers were exposed to an aqueous incubation medium at 37 °C. Notably, only the multiblock copolymers containing PEG4000 were observed to degrade and dissolve upon transition

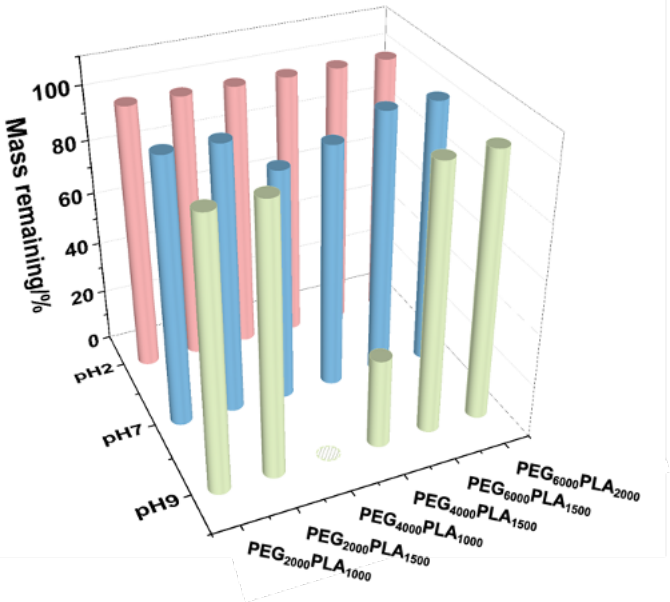

Fig. 2-6. Degradation behavior of PEG-PLA multiblock copolymers in different pH conditions for 24 h.

from an acidic condition to a neutral condition and to an alkaline pH medium after 24 h of immersion, resulting in rapid weight loss. In contrast, the multiblock copolymers with other PEG content demonstrated structural stability in aqueous solutions with varying pH conditions. This observation might be attributed to a reduction in the PEG content (specifically PEG2000) and an enhancement in the crystallization ability of the PEG-PLA copolymer (PEG6000). Collectively, these factors limit the diffusive motion of molecules, thereby contributing to the structural integrity of multiblock copolymers. This behavior can be explained by the degradation of the two-phase microstructure of the PEG-PLA multiblock copolymer films. The cleavage of the main chains is initiated by the ester bonds present in the amorphous phase of the entire specimen. It progresses gradually until the amorphous phase is almost exhausted.

These findings revealed that $PEG_{4k}PLA_{1.5k}$ displayed desirable crystallinity properties for biomedical applications, exceptional water durability, suitable mechanical properties, and pH sensitivity. As a result, $PEG_{4k}PLA_{1.5k}$ was identified as the optimal composition for subsequent characterization and applications.

2.3.6 In vitro gastrointestinal degradation test of the PEG-PLA multiblock copolymers

The esophagus typically exhibits a pH range of 4 to 7 [40,43]. To meet the clinical treatment period of 2 to 6 months [4,44], it was necessary to study the degradation behavior of PEG-PLA multiblock copolymers under varying pH conditions of simulated gastrointestinal fluids environments. To gain further insights into the degradation behavior of PEG-PLA multiblock copolymers in human body biofluids, we investigated the degradation of $PEG_{4k}PLA_{1.5k}$ in SGF and intestinal fluid SIF. This simulation enables researchers to observe how the stent material behaves when exposed to gastric fluids, thereby predicting its performance within the human body. The remaining mass experiment was conducted to monitor the degradation rate of $PEG_{4k}PLA_{1.5k}$ over 24 h, with the immersion fluid replaced every 2 h. **Fig. 2-7a** illustrates the mass remaining ratio curves in the two solutions. The remaining mass ratio in the SGF containing pepsin remained close to 100% throughout the immersion process, which was calculated using **Eq. (2-2)**. Conversely, the presence of pancreatin in SIF with trypsin resulted in a significantly lower mass remaining ratio than that in SGF with pepsin.

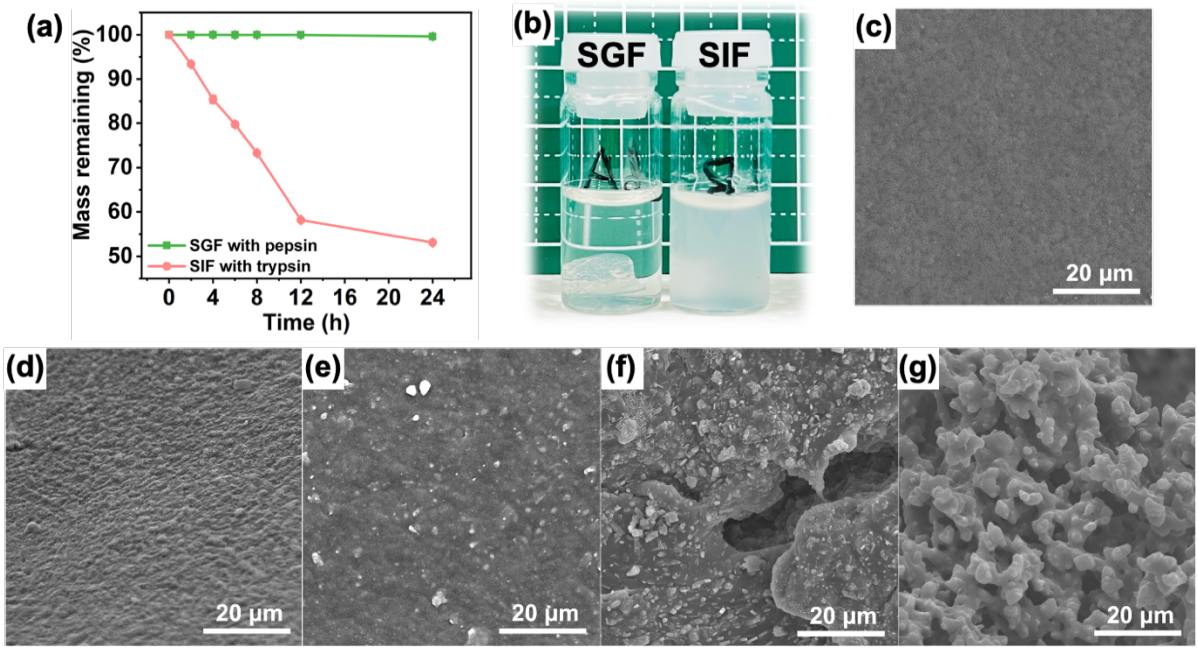

Fig. 2-7. (a) Degradation profiles of $PEG_{4k}PLA_{1.5k}$ in SGF with pepsin and SIF with trypsin (b) Photographs of $PEG_{4k}PLA_{1.5k}$ in different simulated solutions (c) SEM image of the surface micromorphology of $PEG_{4k}PLA_{1.5k}$ before in vitro degradation test (d) SEM image of the surface micromorphology of $PEG_{4k}PLA_{1.5k}$ after incubation in SGF with pepsin for 8 h and (e) 24 h (f) SEM images of the surface micromorphology of $PEG_{4k}PLA_{1.5k}$ after incubated in SIF with trypsin for 8 h and (g) 24 h.

Specifically, during immersion in the SIF with pepsin, $PEG_{4k}PLA_{1.5k}$ exhibited a high corrosion rate at the initial stage, gradually decreasing over time in all solutions. This behavior indicates the formation of a corrosion product layer on the surface of $PEG_{4k}PLA_{1.5k}$. As depicted in **Fig. 2-7b**, the visual appearance of $PEG_{4k}PLA_{1.5k}$ after 24 h of immersion in SGF (left, transparent solution) and SIF (right, cloudy solution) corresponded to the mass loss results. SEM was used to further study the microstructure of $PEG_{4k}PLA_{1.5k}$. The SEM images displayed in **Fig. 2-7(d-g)** revealed the morphologies of $PEG_{4k}PLA_{1.5k}$ after 24 h of immersion in the simulated solutions. In SGF, the sample surface appeared smooth and flat without any cracks, as shown in **Fig. 2-7d** (8 h) and **Fig. 2-7e** (24 h). In contrast, the sample soaked in SIF exhibited a dense degradation product with numerous microcracks spanning the entire surface, as shown in **Fig. 2-7g**. The degradation products of SIF are fragile and prone to detachment. These SEM observations aligned well with the previous in vitro degradation test results. In conjunction with these observations, it was proven that $PEG_{4k}PLA_{1.5k}$ exhibited remarkable stability in vitro when exposed to SGF conditions but very low in the SIF conditions. These results suggest the potential suitability of $PEG_{4k}PLA_{1.5k}$ as an esophageal stent, offering stability for the orderly

self-expanding process. Then, it can be slowly biodegradable and absorbed in neutral conditions of the esophagus over time, upon reaching the intestinal tract should it decompose further or be excreted, thus ensuring harmlessness to the body and eliminating the need for surgical removal. This reduces the risk of complications associated with long-term implantation and offers a more patient-friendly treatment option.

2.3.7 Evaluation of SME of PEG-PLA multiblock copolymers

The appropriate polymer building blocks are carefully chosen based on the desired characteristics of the target multiblock copolymers. PEG-PLA multiblock copolymers are influenced by the expected physical crosslinking transition in the structures of the PEG-PLA and the hydrophilicity of the PEG.

To demonstrate the thermo-responsive SME, a sample of chosen $PEG_{4k}PLA_{1.5k}$ with a strip spline was first heated to 37 °C. Subsequently, a temporary spiral shape was obtained through deformation under stress, then cooling to –20 °C for 10 min. Finally, after stress release, the fixed temporary shape was carried out to recover to its original state by sequential heating at palm temperature (37 °C), displaying superior thermo-responsive SME triggered by body temperature, as illustrated in **Fig. 2-8**.

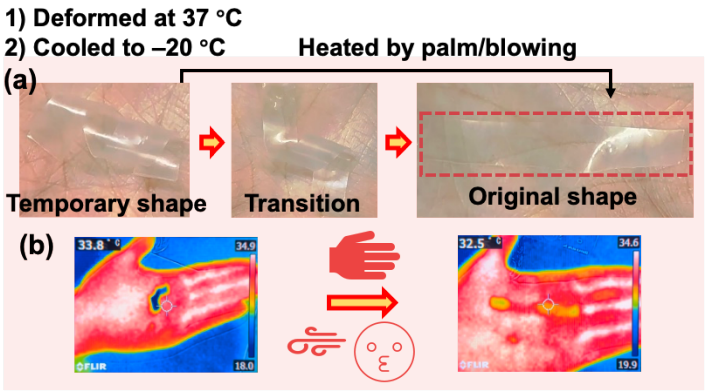

Fig. 2-8. The thermo-responsive process of $PEG_{4k}PLA_{1.5k}$ by palm recorded using a digital camera (a) and an infrared thermal video camera (b).

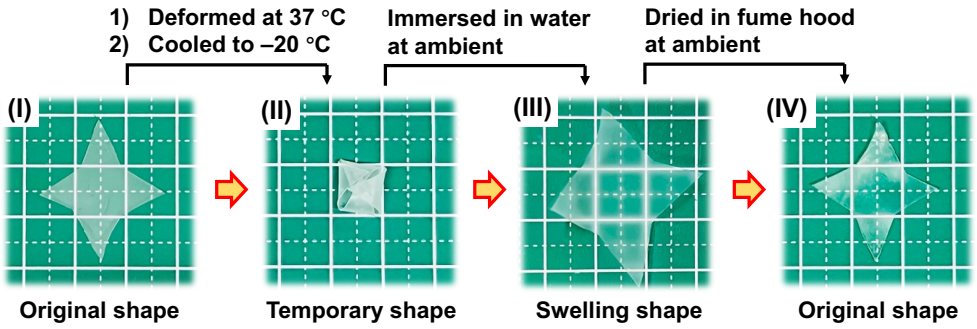

Fig. 2-9. Water-responsive process of $PEG_{4k}PLA_{1.5k}$ recorded using a digital camera.

Similarly, the water-responsive SME was achieved by subjecting a star-shaped $PEG_{4k}PLA_{1.5k}$ multiblock copolymer to shape-memory programming. The material was exposed to water, recovering its original shape, as shown in **Fig. 2-9**.

The shape recovery process of P $PEG_{4k}PLA_{1.5k}$ from a temporary shape back to its original shape is observed when heated by the human body at T_{trans}, as depicted in **Fig. 2-8**. This phenomenon is mainly due to the melting of the crystallized PEG phase. Additionally, the return of the original star shape when the multiblock copolymer is immersed in ambient temperature water is attributed to the diffusion of water molecules acting as plasticizers and the disruption of the crystallinity of the PEG phase (**Fig. 2-9**). These results underscore the remarkable shape memory properties of $PEG_{4k}PLA_{1.5k}$, indicating their potential for various applications that respond to temperature and water stimuli.

2.3.8 In vitro application of the PEG-PLA multiblock copolymer as a new type of esophageal stent

A comprehensive analysis and discussion were undertaken to study the fundamental aspects of $PEG_{4k}PLA_{1.5k}$, specifically its thermo- and water-responsive shape memory behaviors. Encouraging results from these investigations have inspired the development of novel biodegradable esophageal stents. SMBS, fabricated using $PEG_{4k}PLA_{1.5k}$, exhibit a high degree of responsiveness to changes in body temperature and possess exceptional swelling abilities, surpassing those seen in some chemically crosslinked polymer networks. This self-expandable stent can load and sustainably release specific amounts of anti-cancer and anti-inflammatory drugs within the moist environment of the esophagus. The SMBS recovery process can be programmed step-by-step, as illustrated in **Scheme 2-2**.

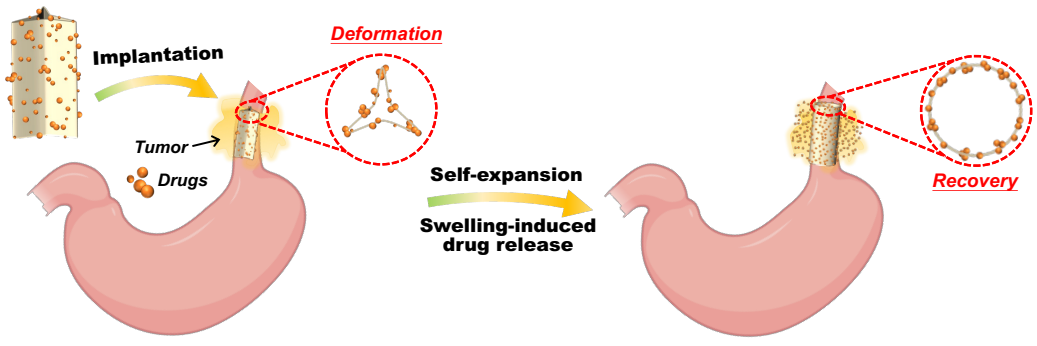

Scheme 2-2. Graphic illustration of the self-expansion and swelling-induced drug release of SMBS.

In vitro evaluations were conducted to validate this concept, considering the results mentioned earlier, along with the pH-dependent and gastrointestinal degradability of $PEG_{4k}PLA_{1.5k}$. Initially, the $PEG_{4k}PLA_{1.5k}$ multiblock copolymer film was dyed with a diluted Orange G aqueous solution. This dye served as a drug molecule and facilitated the visualization of the simulated drug loading and delivery processes. Subsequently, a novel SMBS was fabricated using the dyed $PEG_{4k}PLA_{1.5k}$ multiblock copolymer film, as depicted in **Fig. 2-10**.

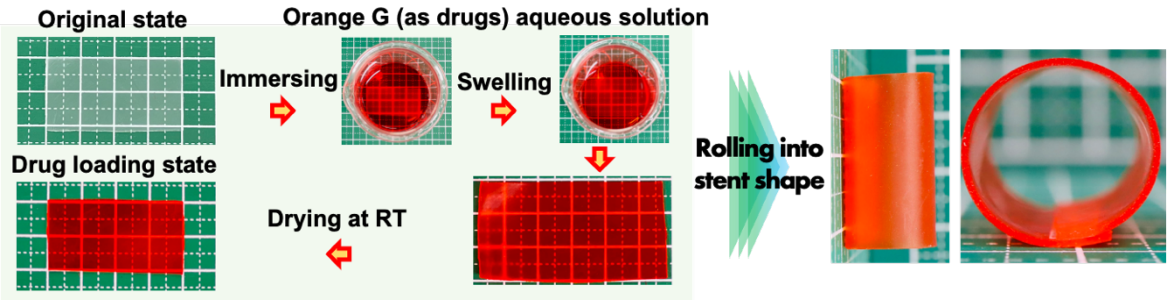

Fig. 2-10. Digital camera recording of the drug carrier process of $PEG_{4k}PLA_{1.5k}$ simulated by soaking in the Orange G aqueous solution.

Importantly, when immersed in the respective drug solution, the $PEG_{4k}PLA_{1.5k}$ multiblock copolymer film could absorb any drug molecule with good water solubility. To ensure that the dyeing process (simulated drug carrier process) did not affect the properties of $PEG_{4k}PLA_{1.5k}$, quantitative and qualitative evaluations of its thermo-responsive shape memory properties were performed. First, quantitative shape-programming experiments were performed using the procedure shown in **Fig. 2-11**. A T_{high} of 37 °C, determined from the DSC analysis (T_{trans} = 31.90 °C, T_m of PEG), was selected as the triggering temperature for the thermo-induced SME. The assessment of shape memory properties included the

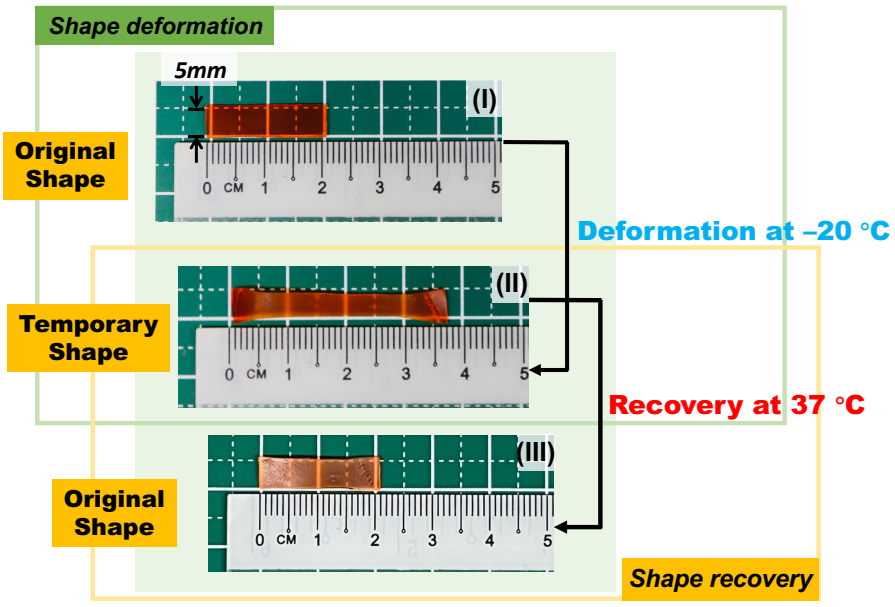

Fig. 2-11. Thermo-responsiveness of the dyed $PEG_{4k}PLA_{1.5k}$ multiblock copolymer film recorded using a digital camera.

evaluation of the recovery of the multiblock copolymer after undergoing manual stretching, fixing, and reheating stimulations. The extent of recovery was determined by quantifying the changes in length using a ruler. The results demonstrated excellent thermally induced shape memory properties with a recovery rate of 99.5%. This value was determined from calculations performed using **Eq. (2-3)** and **(2-4)**, as presented in **Table 2-4.**

Table 2-4 PEG-PLA multiblock copolymers determined by cyclic thermo-mechanical tensile test under 37 °C as recovery temperature

Samples	R_f (%)	R_r (%)
$PEG_{2k}PLA_{1k}$	-	-
$PEG_{2k}PLA_{1.5k}$	-	-
$PEG_{4k}PLA_{1k}$	95.80%	56.10%
$PEG_{4k}PLA_{1.5k}$	98.20%	99.50%
$PEG_{6k}PLA_{1.5k}$	50.30%	43.10%
$PEG_{6k}PLA_{2k}$	56.50%	32.30%

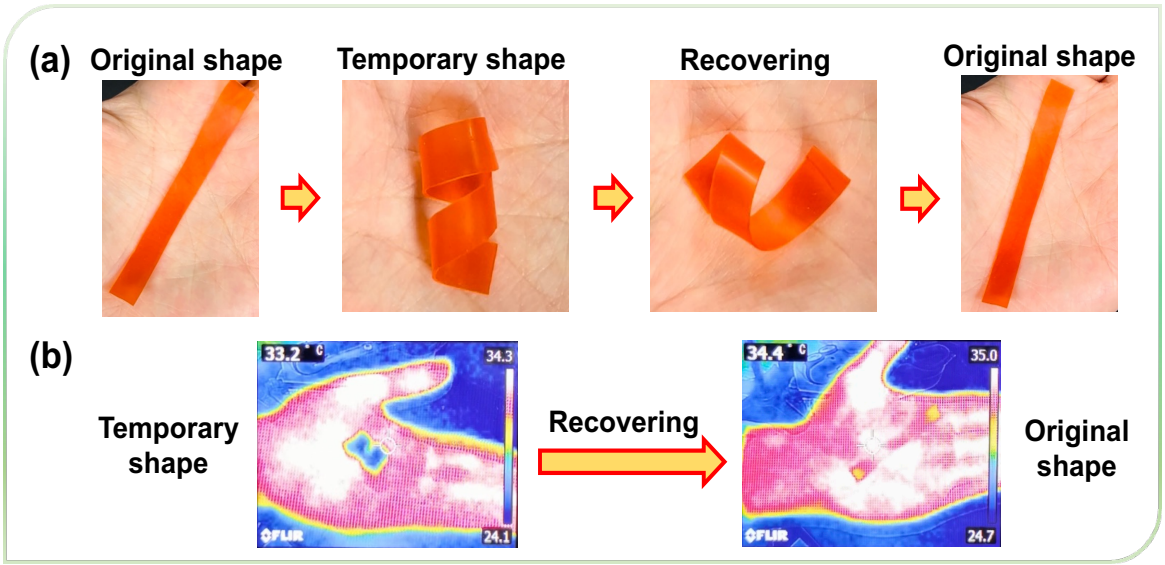

Fig. 2-12. (a) Thermo-responsiveness of dyed $PEG_{4k}PLA_{1.5k}$ by palm recorded using a digital camera (b) and an infrared thermal video camera.

Accordingly, the bent membranes displayed exceptional recovery processes on a 37 °C temperature platform as well. Furthermore, as shown in **Fig. 2-12**, the same results were obtained when the material was exposed to the human body temperature (palm), as anticipated.

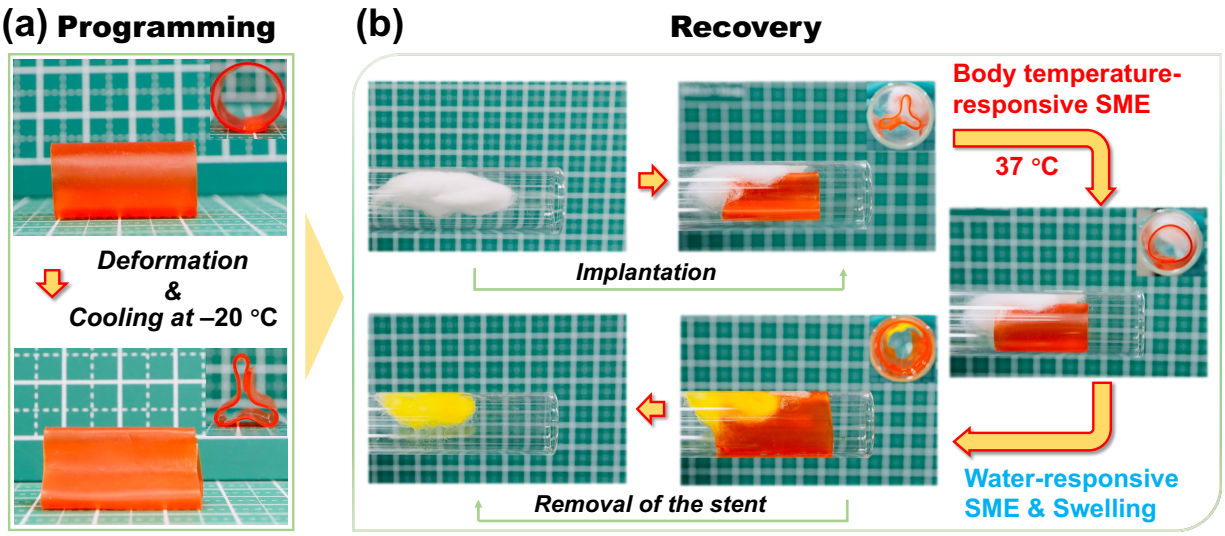

Fig. 2-13. Application of the polymer network as an esophageal stent. (a) Photos showing the $PEG_{4k}PLA_{1.5k}$ with a stent structure and the temporary shape fixation. (b) Photos showing the implantation, adjustment, and drug release of the $PEG_{4k}PLA_{1.5k}$ stent based on the SME.

Subsequently, a custom-made glass tube partially obstructed by a cotton pad was prepared to simulate an occluded esophagus before the in vitro implantation assessment. The PEG-PLA SMBS, in its contracted state after deformation, was easily implanted into the esophagus (glass tube) and positioned near the tumor (cotton), as shown in **Fig. 2-13a**. With the body temperature-induced SME alone, SMBS almost completely recovered its original shape, providing mechanical support to expand the blocked esophagus. Upon subsequent water treatment, the SMBS fully recovered its original shape owing to the water-responsive SME induced by the biofluids. This complete recovery facilitated a tighter implantation and enabled drug release from the stent. Notably, localized and sustained drug delivery effectively suppressed the pain and tumor growth around the SMBS, highlighting its potential for biomedical applications.

2.4 Conclusions

Biodegradable esophageal stents with on-demand synchronous shape memory and drug-release functionality were fabricated by exploiting the SME of a shape-memory multiblock copolymer programmed in a specific shape. Various PEG-PLA multiblock copolymers with different structures were successfully synthesized using a simple one-pot ring-opening and coupling reaction strategy to achieve this goal. PEG-PLA multiblock copolymers exhibited tunable transition temperatures (33–53 °C) and significant water durability (WUR, ~328%). Additionally, PEG-PLA exhibited high elongation at break (~1920.6%) and excellent pH-dependent and enzyme-dependent biodegradability. In particular, $PEG_{4k}PLA_{1.5k}$ displayed excellent body temperature-triggered (recovery rate reached 99.5%) and water-triggered dual SME. Furthermore, the *in vitro* assessment showed that the novel self-expanding SMBS could release drugs locally and sustainably, potentially exerting a substantial influence on disease treatment. For instance, through the sequential body temperature- and water-responsive behavior of SMBS, drugs can be immobilized at the target site during cancer therapy to release and function gradually. Thus, the development of a novel shape memory multiblock copolymer stent, capable of responding to body temperature and water while simultaneously functioning as a carrier for drugs, has substantial significance in addressing the therapeutic requirements of esophageal stenosis. The simple design requirements of the SMBS contribute to its potential for various biomedical applications.

2.5 References

[1] C. G. Park, M. H. Kim, M. Park, J. E. Lee, S. H. Lee, J. H. Park, K. H. Yoon, Y. Bin Choy, *Macromol. Res.* **2011**, *19*, 1210.

[2] M. Arnold, I. Soerjomataram, J. Ferlay, D. Forman, *Gut* **2015**, *64*, 381.

[3] E. Morgan, I. Soerjomataram, H. Rumgay, H. G. Coleman, A. P. Thrift, J. Vignat, M. Laversanne, J. Ferlay, M. Arnold, *Gastroenterology* **2022**, *163*, 649.

[4] Y. Kang, *Biomed. Res. Int.* **2019**, *2019*, e9265017.

[5] A. Dobashi, D. K. Li, G. Mavrogenis, K. H. Visrodia, F. Bazerbachi, *Thorac. Surg. Clin.* **2022**, *32*, 479.

[6] C. S. Shim, Y. D. Cho, J. H. Moon, J. O. Kim, J. Y. Cho, Y. S. Kim, J. S. Lee, M. S. Lee, *Endoscopy* **2001**, *33*, 843.

[7] X. Yu, L. Wang, M. Huang, T. Gong, W. Li, Y. Cao, D. Ji, P. Wang, J. Wang, S. Zhou, *J. Mater. Sci: Mater. Med.* **2012**, *23*, 581.

[8] T. M. Jeewandara, S. G. Wise, M. K. C. Ng, *Materials (Basel)* **2014**, *7*, 769.

[9] D. M. Whelan, W. J. van der Giessen, S. C. Krabbendam, E. A. van Vliet, P. D. Verdouw, P. W. Serruys, H. M. van Beusekom, *Heart* **2000**, *83*, 338.

[10] R. A. Byrne, G. W. Stone, J. Ormiston, A. Kastrati, *Lancet* **2017**, *390*, 781.

[11] S. Law, P. H. M. Tung, K. M. Chu, J. Wong, *Gastrointest. Endosc.* **1999**, *50*, 427.

[12] R. F. Wong, D. G. Adler, K. Hilden, J. C. Fang, *Dig. Dis. Sci.* **2008**, *53*, 322.

[13] Z. Zheng, J. Hu, H. Wang, J. Huang, Y. Yu, Q. Zhang, Y. Cheng, *ACS Appl. Mater. Interfaces* **2017**, *9*, 24511.

[14] T. Tsuji, H. Tamai, K. Igaki, E. Kyo, K. Kosuga, T. Hata, M. Okada, T. Nakamura, S. Motohara, H. Uehata, *Curr. Interv. Cardiol. Rep.* **2001**, *3*, 10.

[15] S. Bangalore, B. Toklu, N. Amoroso, M. Fusaro, S. Kumar, E. L. Hannan, D. P. Faxon, F. Feit, *BMJ* **2013**, *347*, f6625.

[16] W. M. Huang, Z. Ding, C. C. Wang, J. Wei, Y. Zhao, H. Purnawali, *Mater. Today* **2010**, *13*, 54.

[17] M. Behl, A. Lendlein, *Mater. Today* **2007**, *10*, 20.

[18] W. M. Huang, B. Yang, L. An, C. Li, Y. S. Chan, *Appl. Phys. Lett.* **2005**, *86*, 114105.

[19] H. Xie, K. K. Yang, Y. Z. Wang, *Prog. Polym. Sci.* **2019**, *95*, 32.

[20] M. J. He, W. X. Xiao, H. Xie, C. J. Fan, L. Du, X. Y. Deng, K. K. Yang, Y. Z. Wang, *Mater. Chem. Front.* **2017**, *1*, 343.

[21] M. Q. Li, J. M. Wu, F. Song, D. D. Li, X. L. Wang, L. Chen, Y. Z. Wang, *Compos. Sci. Technol.* **2019**, *173*, 1.

[22] L. Du, J. Dai, Z. Y. Xu, K. K. Yang, Y. Z. Wang, *Polymer* **2019**, *172*, 52.

[23] X. J. Han, Z. Q. Dong, M. M. Fan, Y. Liu, J. H. Li, Y. F. Wang, Q. J. Yuan, B. J. Li, S. Zhang, *Macromol. Rapid Commun.* **2012**, *33*, 1055.

[24] C. M. Yakacki, R. Shandas, D. Safranski, A. M. Ortega, K. Sassaman, K. Gall, *Adv. Funct.*

Mater. **2008**, *18*, 2428.
[25] P. Testa, R. W. Style, J. Cui, C. Donnelly, E. Borisova, P. M. Derlet, E. R. Dufresne, L. J. Heyderman, *Adv. Mater.* **2019**, *31*, 1900561.
[26] Q. Zhao, J. Wang, H. Cui, H. Chen, Y. Wang, X. Du, *Adv. Funct. Mater.* **2018**, *28*, 1801027.
[27] B. Q. Y. Chan, Z. W. K. Low, S. J. W. Heng, S. Y. Chan, C. Owh, X. J. Loh, *ACS Appl. Mater. Interfaces* **2016**, *8*, 10070.
[28] S. Paonessa, N. Barbani, E. C. Rocchietti, C. Giachino, C. Cristallini, *Mater. Sci. Eng. C Mater. Biol. Appl.* **2017**, *75*, 1427.
[29] L. Du, S. Yang, W. Li, H. Li, S. Feng, R. Zeng, B. Yu, L. Xiao, H. Y. Nie, M. Tu, *Mater. Sci. Eng. C. Mater. Biol. Appl.* **2017**, *78*, 1172.
[30] Y. Xia, Y. He, F. Zhang, Y. Liu, J. Leng, *Adv. Mater.* **2021**, *33*, 2000713.
[31] J. Torres, J. Cotelo, J. Karl, A. P. Gordon, *JOM* **2015**, *67*, 1183.
[32] H. Tamai, K. Igaki, E. Kyo, K. Kosuga, A. Kawashima, S. Matsui, H. Komori, T. Tsuji, S. Motohara, H. Uehata, *Circulation* **2000**, *102*, 399.
[33] T. Välimaa, S. Laaksovirta, T. L. J. Tammela, P. Laippala, M. Talja, T. Isotalo, A. Pétas, K. Taari, P. Törmälä, *Biomaterials* **2002**, *23*, 3575.
[34] L.D. Kimble, D. Bhattacharyya, S. Fakirov, *eXPRESS Polym. Let.* **2022**, *9*, 300.
[35] N. Grabow, C. M. Bünger, C. Schultze, K. Schmohl, D. P. Martin, S. F. Williams, K. Sternberg, K. P. Schmitz, *Ann. Biomed. Eng.* **2007**, *35*, 2031.
[36] A. Z. Naser, I. Deiab, B. M. Darras, *RSC Adv.* **2021**, *11*, 17151.
[37] W. Wang, P. Ping, X. Chen, X. Jing, *Eur. Polym. J.* **2006**, *42*, 1240.
[38] R. Paberit, E. Rilby, J. Göhl, J. Swenson, Z. Refaa, P. Johansson, H. Jansson, *ACS Appl. Energy Mater.* **2020**, *3*, 10578.
[39] M. Tobío, A. Sánchez, A. Vila, I. Soriano, C. Evora, J. L. V. Jato, M. J. Alonso, *Colloids Surf. B Biointerfaces* **2000**, *18*, 315.
[40] Y. Chen, X. Yan, J. Zhao, H. Feng, P. Li, Z. Tong, Z. Yang, S. Li, J. Yang, S. Jin, *Carbohydr. Polym.* **2018**, *191*, 8.
[41] H. Tobushi, H. Hara, E. Yamada, S. Hayashi, *Smart Mater. Struct.* **1996**, *5*, 483.
[42] A. Lendlein, S. Kelch, *Angew. Chem. Int. Ed.* **2002**, *41*, 2034.
[43] G. Champion, J. E. Richter, M. F. Vaezi, S. Singh, R. Alexander, *Gastroenterology* **1994**, *107*, 747.
[44] Y. Saito, T. Tanaka, A. Andoh, H. Minematsu, K. Hata, T. Tsujikawa, N. Nitta, K. Murata, Y. Fujiyama, *World. J. Gastroenterol.* **2007**, *13*, 3977.

Chapter 3. High-performance bioinspired multi-responsive chiral cellulose nanocrystals-based flexible films for information encryption

3.1 Introduction

In the era of artificial intelligence and information technology, traditional anti-counterfeiting methods are becoming increasingly vulnerable due to easily accessible decryption processes. This situation underscores the need for improving encryption and decryption technologies that offer high levels of security while maintaining convenient operation to mitigate the potential risks of information breaches. The scenario necessitates the development of encryption and decryption technologies that are highly secure and convenient to operate to alleviate the risks of information leaks. A common method involves integrating various anti-counterfeiting elements into materials [1–3]. Another method leverages multiple stimuli to function as crucial factors for information decryption [4–6]. However, multilevel anti-counterfeiting materials require complex manufacturing, advanced machines, extensive energy consumption, and time waste.

Structural colors originate from the interaction of visible light with micro/nanostructures through interference, diffraction, or scattering. These present a broad range of colors and sustainability compared with conventional chemical pigments and dyes [7,8]. The long-range order of these materials generates an anisotropic photonic bandgap (PBG) that enables light to be reflected at specific wavelengths [9]. Consequently, when observed from various viewing angles, these materials display varying structural colors (or iridescence) [10,11]. These have aroused considerable attention for applications such as anti-counterfeiting, information storage, and colorimetric sensing [12–16]. In contrast, angle-independent structural colors are formed by amorphous arrays that exhibit only a short-range order [17–20].

Cellulose nanocrystals (CNCs) are attractive for their crystallinity, strength, and aspect ratio [21]. The interaction between the electrostatic repulsion of the sulfate ester groups on CNCs and the hydrogen bonding between these facilitates the formation of layered chiral nematic

photonic crystals through evaporation-induced self-assembly (EISA) [22,23]. These results produce variable iridescent structural colors that can be tuned by stimuli-induced helical pitch. In addition, it endows CNC films with inherent selective reflection of circularly polarized light (CPL) [24]. Although CNCs are used extensively in green optical devices, anti-counterfeiting, and information storage due to their sustainability and biocompatibility, their rigidity and brittleness limit their further applications [25]. Recent efforts have focused on enhancing the functionality and practical applications of chiral nematic CNC films by controlling the pitch and chiral organization of the CNCs to create uniform structural colors and by introducing polymers with different properties into the CNC's chiral nematic structure (such as mechanical flexibility and solvent resistance) [26]. Small molecules, such as glycerol [27] and citric acid [28], have been utilized as plasticizers to enhance the flexibility of CNC. However, the incorporation of PVA [29], PEG [30,31], and polysaccharides [32,33] into CNC has been shown to provide even better mechanical properties improvement for CNC-based iridescent materials. Despite these advancements, further enhancement of the mechanical properties is required for more intricate practical applications. The high flexibility of the poly(methyl methacrylate) [34] and poly(ethylene glycol) diacrylate [35] chains also imparts remarkable strength and elasticity to the CNC films through chemical crosslinking. Despite these improvements, considering the sustainability after use, it would be preferable to incorporate biodegradable polymers into CNC through an efficient evaporation-induced co-assembly process.

A potential approach inspired by the peacock feather's microstructure (**Scheme 3-1b**) (which exhibits iridescent colors owing to its unique combination of periodicity and defects [36–38] and thereby results in high/low angle dependence and reflectance structural color variations) involves manipulating the microstructure by strategically blending CNCs with flexible polymers displaying superior mechanical properties by varying the compositions. This ensures the preservation of the CNC's chiral structure without the need for complex operations and structural designs. Previous studies have shown that with the introduction of semi-crystalline polymers such as PEG into CNC when the content exceeds 40%, the chiral layered structure of the composite film is disrupted. This leads to a noteworthy blueshift in structural color [30,39]. However, whether additional polymers can yield new equilibrium structures has not been

studied. Dong et al. constructed CNC composite films that transitioned from angle-dependent to angle-independent by adding different amounts of poly (dimethyl diallyl ammonium) chloride [40]. This demonstrated the feasibility of our designed strategy.

The stability of CNC aqueous suspension significantly impacts the EISA process, which limits the structural coloration possibilities and restricts the use of CNCs with a wider range of water-insoluble polymers. Currently, there have been no studies exploring the use of water-insoluble, biomass-derived, and biodegradable polymers in creating flexible CNC-based chiral nematic composite films with structural colors. Therefore, there is a need to design multi-responsive functional iridescent CNC/water-insoluble polymer flexible composites with a simple yet effective strategy. These materials can achieve reversible structural coloration suitable for various practical environments while maintaining the chiral nematic structures.

Bio-based PLA has gathered significant attention due to its biodegradability, heat resistance, and high transparency [41]. However, it is water-insoluble. A common method for water-insoluble polymers comprises blending and ultrasonication with freeze-dried CNCs for dispersion in dipole aprotic solvents such as DMSO or DMF [42,43]. Another approach involves surface modification to enhance hydrophobicity, which can disrupt the essential structure of CNCs needed for structural color formation [44,45]. Chang et al. demonstrated that CNC suspensions prepared in DMF, water, and their mixtures (even with water contents of 25–75%) were more effective in dispersing CNC than pure water or DMF [46]. Based on the findings from Chapters 1 and 2, it is evident that PEG-PLA biodegradable copolymers possess exceptional properties such as flexibility, toughness, hydrophilicity, and water uptake ability. Which also recognized for their amphiphilic nature, good biocompatibility, non-toxicity, and widespread application in the biomedical field [48]. Therefore, the integration of DMF solutions containing hydrophilic PEG-PLA water-insoluble polymers into CNC aqueous suspensions could potentially be accomplished through a direct blending approach. In addition, as we mentioned in the **General Introduction**, given the self-assembling properties of block copolymers, incorporating PEG-PLA copolymers into CNCs is highly feasible.

In this chapter, by blending two separately processed components, incorporating water-insoluble PEG-PLA copolymers into CNC using evaporation-induced co-assembly to fabricate CNC/PEG-PLA composite films was studied. This composite film has a 1044 % increase in toughness, reversible robust structural color, and the convenience of storing, cutting, and deformation. They presented effective responses to stimuli such as left-handed CPL and different backgrounds. They also demonstrated a high/low angle-dependent structural color response affected by the PEG-PLA content. Additionally, the CNC/PEG-PLA composite film displayed reversible and stable structural colors under varying relative humidity (RH) environments. It shows a fast 18 s redshift to attain equilibrium in water. With these features, we demonstrated a coding array designed to encrypt information in channels with reversible color-variation responses for encoding/decoding and further translate information using the Caesar cipher for on-demand decryption.

3.2 Experimental Section

3.2.1 Material

Quantitative filter paper (No. 5C) utilized as the pristine cellulose source (Advantec, Toyo Roshi Co. Ltd., Japan) was torn up into small slices for use. PEG-PLA copolymer multiblock (M_n = 5.39×10^4 g mol^{-1} and PDI = 1.86 from GPC) was prepared by ring-opening and coupling reaction from PEG-diol (M_n = 4000 Da, GR grade) and poly(L-lactide) as we previously reported [47]. Sulfuric acid (H_2SO_4, 64%), N, N-dimethyl formamide (DMF, >99.5%), methanol (>99.8%), ethanol (>99.5%), acetone (>99.5%), chloroform ($CHCl_3$, >99.5%), magnesium chloride ($MgCl_2$), magnesium nitrate [$Mg(NO_3)_2$], potassium iodide (KI), potassium chloride (KCl), and potassium sulfate (K_2SO_4) were purchased from Wako Pure Chemical Industries Ltd. (Tokyo, Japan) Acetone (>99.5%) and tetrahydrofuran (THF, >99.5%) were supplied by Nacalai Tesque, INC. (Kyoto, Japan). All the chemical reagents were used as received. Dialysis membrane (MCWO 10000, Spectra/Por® 6 Standard Regenerated Cellulose Dialysis Tubing, Pre-Wetted) was purchased from Repligen Corporation (Waltham, USA). Deionized (DI) water

was obtained with a Millipore purification system (Millipak® Express 40 Filter, Millipore Inc., Milford, USA) was used for each experiment.

3.2.2 Preparation of CNC suspensions

Based on the previously reported acidic hydrolysis approach [49,50], modifications were performed to produce the desired CNC suspensions (**Scheme 3-1a**). Briefly, 30 g of chopped filter paper (cotton as cellulose source) underwent hydrolysis by reacting with 450 mL of 64% H_2SO_4 solution in the ratio of 1:15 g mL^{-1} under vigorous mechanical stirring (~500 rpm) at 45°C for 45 minutes. The reaction was quenched by adding a 10-fold volume of ice-cold DIW, and the reaction vessel was cooled in an ice bath. The excess acidic solution containing soluble cellulose residues and excess acid was removed via centrifugation at 9000 rpm for 10 minutes at 4 °C. The particles were redispersed in DIW after each round. This purification step was repeated until optical turbidity was observed in the supernatant. They were then centrifugated at a low speed and filtrated to eliminate large CNC nanoparticles of CNC, and then the turbid supernatant was collected. Subsequently, they were dialyzed with a membrane against DIW to obtain neutral CNC suspensions (pH 6.8). Finally, CNC suspensions were concentrated to 5.58 wt% using a rotary evaporator and stored at 4 ℃ for further use.

3.2.3 Fabrication of iridescent CNC/PEG-PLA composites films

DMF solutions of $PEG_{4k}PLA_{1k}$ at concentrations of 0, 0.02, 0.03, 0.04, 0.05, and 0.06 g mL^{-1} were mixed with the CNC suspension in a 3:2 volume ratio via the evaporation-induced co-assembly process to fabricate CNC/PEG-PLA composite films (**Scheme 3-1c**). The corresponding CNC and $PEG_{4k}PLA_{1k}$ mass fraction are listed in **Table 3-1**. The corresponding samples are CNC, CNC/P2, CNC/P3, CNC/P4, CNC/P5, and CNC/P6, respectively. The mixed binary suspensions were stirred overnight to obtain uniform dispersions, and an ultrasonic homogenizer (SONICSTAR85 Violamo, AS ONE Co. Ltd., Osaka, Japan) was employed to degas and disperse the suspensions to create CNC/PEG-PLA colloidal dimensions. The time, output level, and frequency of ultra-sonification were 2 min, 50 W, and 50–60 kHz, respectively. Subsequently, the composite suspensions were cast onto diameter aluminum molds of 5.7 cm

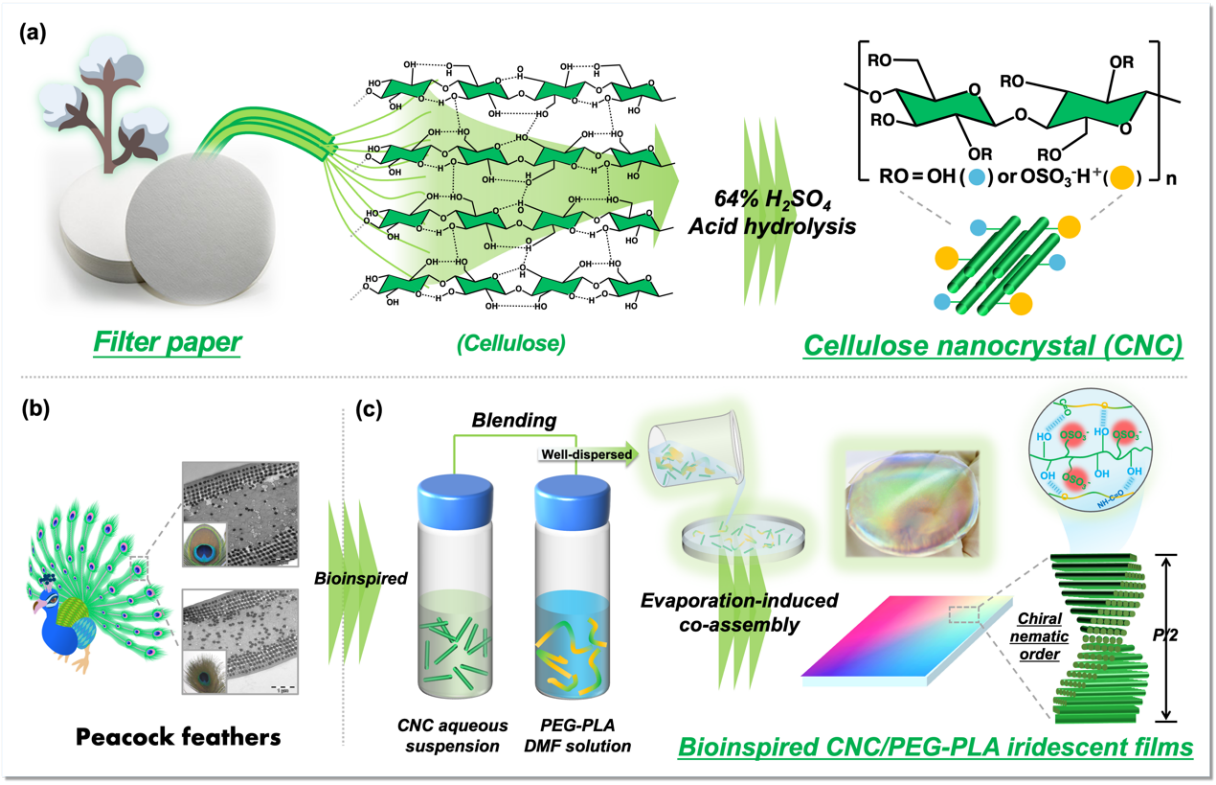

Scheme 3-1. Bioinspired design of structural color CNC/PEG-PLA composite films. (a) Schematic route of acid hydrolysis synthesis of CNCs. (b) A peacock and TEM images of the cross-section microstructure of its feathers at different ages [37]. (c) Fabrication of CNC/PEG-PLA composite films with a chiral nematic structure through evaporation-induced co-assembly process and the intermolecular interaction between CNC and PEG-PLA (P/2 indicates the half-helical pitch).

and dried in an oven at 30 °C for 3–4 days until constant weight to obtain solid CNC composite films. For subsequent tests, these films were stored in a dry desiccator at 25 °C and with 49% relative humidity (RH).

Table 3-1 The essential characteristics of CNC/PEG-PLA suspension

Samples	CNC/$PEG_{4k}PLA_{1k}$ (wt%)	DLS average size (nm)	PI	Zeta potential (mV)	Mobility ($cm^2\ Vs^{-1}$)
CNC	100	163.8	0.340	–56.03	-4.37×10^{-4}
CNC/P2	81.51/18.41	143.9	0.281	–48.06	-3.75×10^{-4}
CNC/P3	74.72/25.28	152.4	0.284	–42.69	-3.33×10^{-4}
CNC/P4	68.91/31.09	166.7	0.244	–29.10	-2.27×10^{-4}
CNC/P5	63.94/36.06	192.7	0.292	–16.17	-1.02×10^{-4}
CNC/P6	59.64/40.36	228.5	0.291	–7.48	-5.83×10^{-5}

3.2.4 Humidity-responsive behavior of CNC/PEG-PLA composite films

Saturated $MgCl_2$, $Mg(NO_3)_2$, KI, KCl, and K_2SO_4 solutions were prepared to generate various RH conditions of 33%, 52%, 70%, 85%, and 98% [51]. To generate the specified relative humidity (RH) conditions within the chamber, as depicted in **Fig. 3-1.** The films were equilibrated under the desired RH conditions. Their color variations were recorded using a digital camera.

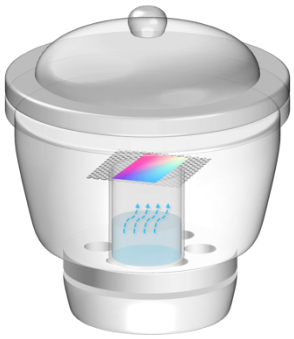

Fig. 3-1. Schematic illustration of the humidity-responsive process of CNC/PEG-PLA composite films in a chamber.

3.2.5 Solvent-responsive performance of CNC/PEG-PLA composite films

Solvents such as water, methanol, ethanol, acetic acid, $CHCl_3$, acetone, and THF were dropped onto the surface of the composite films. The resulting color variations and corresponding UV-vis reflectance spectra were recorded to investigate the response behavior of the composite films toward ethanol/water and ethanol/methanol binary solvent mixtures. Subsequently, the films were left to dry in ambient conditions, and their colors returned to their original state. These experiments were repeated multiple times to assess the reusability of the films. For quantitative analysis, methanol solutions with concentrations ranging from 0 to 100% were prepared using ethanol as the diluting solvent. The detection method employed was the same as previously described.

3.2.6 Characterization and Measurements

Atomic force microscopy (AFM, SPI3800N/SPA-400, Seiko Instruments Inc., Tokyo, Japan) was employed to analyze the morphologies and dimensions of the hydrolyzed CNCs and CNC/PEG4$_k$PLA$_{1k}$ composite films. A diluted CNC suspension (approximately 1.0×10^5 wt%) was dropped on the mica surface. After adsorption onto the surface, the sample was air-dried.

Transmission Electron Microscopy (TEM, JEM-2100, JEOL, Tokyo, Japan) was utilized to observe the morphologies of CNC suspensions. Drops of diluted CNC suspension

were deposited onto a 300 mesh carbon-coated copper grid by glow discharge, excess droplets were removed, and the droplets were then negatively stained using a 1% phosphotungstic acid solution and dried under vacuum for testing.

The hydrodynamic radius and translational diffusion coefficient by dynamic light scattering and charge surface of the CNC and CNC/PEG-PLA were measured with a **ζ-potential and particle size analyzer** (ELSZ-1000ZS, Otsuka Electronics Co. Ltd., Japan) to determine the successful preparation of the CNC/$PEG_{4k}PLA_{1k}$ suspensions. The suspension concentration was fixed at 0.05 wt% for the measurement. For each sample, five parallel measurements were conducted to give average results.

Polarized optical microscopy (POM) in reflectance mode (POM, BX51, Olympus) was used to observe the morphologies of the surface of composite films, and all samples examined by POM were observed on polished surfaces in reflectance mode with automatic white balance function.

The surface elemental composition was measured using **energy-dispersive X-ray spectroscopy** (EDX, HITACHI, Miniscope TM 3000 equipped with Swift ED 3000). Before morphological observation, the samples were dried under vacuum conditions for 4 hours.

X-ray diffraction (XRD) patterns were recorded using a SmartLab (In-plane) (Rigaku Corporation, Japan) with Cu-Kα radiation (λ = 1.541 Å) at RT. The scanning speed was 5° min^{-1} over a 2θ range of 5° to 60°. The generator voltage and current were 45 kV and 200 mA, respectively. The samples were prepared by solvent casting and stored for 1 week at RT before the test. The crystallinity (CrI) of CNCs was calculated using the following formula [52]:

$$\mathbf{CrI\ (\%)} = \frac{I_{200} - I_{am}}{I_{200}} \times 100\%$$

Here, I_{200} is the maximum diffraction peak intensity of the (200) crystal face of CNCs, and its position is 2θ = 22.7°; I_{am} is the minimum scattering peak intensity of the amorphous region of CNCs, and position is 2θ = 18.7°.

The orientation structure was observed by **Small and Wide-angle X-ray scattering (SAXS&WAXS) measurements**, which were performed at the BL40B2 beamline at the Spring-8 synchrotron radiation facility (Hyogo, Japan) and used a highly monochromatic beam with a low divergence and a small cross-section, and 2D images were recorded using the detectors. A flat panel (C9728DK-10; Hamamatsu Photonics KK, Shizuoka, Japan) was used as the detector. The sample-to-detector lengths. The sample-to-detector distance was 1150.0 mm and 58.3 mm for SAXS and WAXS, respectively.

Reflection spectra were recorded by a **UV-vis spectrophotometer** (U-2810, Hitachi, Tokyo, Japan) and scanned in the range of 400–800 nm.

For the other characterization and measurements applied in this chapter please refer to **Section 1.2.6** of **Chapter 1**.

3.3 Results and Discussion

3.3.1 Morphology and structure analysis of CNC/PEG-PLA composite suspensions

This chapter extracted the CNCs from filter paper via acid hydrolysis. The hydrolysis process in sulfuric acid includes the swelling and depolymerization of cellulose. Here, the acid permeates the amorphous and crystalline regions of cellulose by forming complexes. This results in the oxidative decomposition of the amorphous regions [53]. Understanding the morphology, size, and surface charge of CNC is vital for tuning the performance of composite films. As shown in **Fig. 3-2a,b**, the AFM topography, the as-prepared CNCs exhibited homogeneous rod-like nanoparticles. This is consistent with the findings of the literature [54,55]. As illustrated in **Fig. 3-2e,f**, their average length and width were 165.75 ± 34.26 nm and 18.86 ± 4.54 nm, respectively (an aspect ratio of approximately 8.79). The morphology of CNC with a well-defined rod-like shape was further verified by TEM analysis (**Fig. 3-2c**). It is noteworthy that because of the nanometer size of the CNCs, the colloidal CNC in the suspension caused scattering along the laser path, causing the laser beam visible. The Typical Tyndall effect of the CNC suspension is observed in **Fig. 3-2d**. It was also observed in the CNC/PEG-PLA

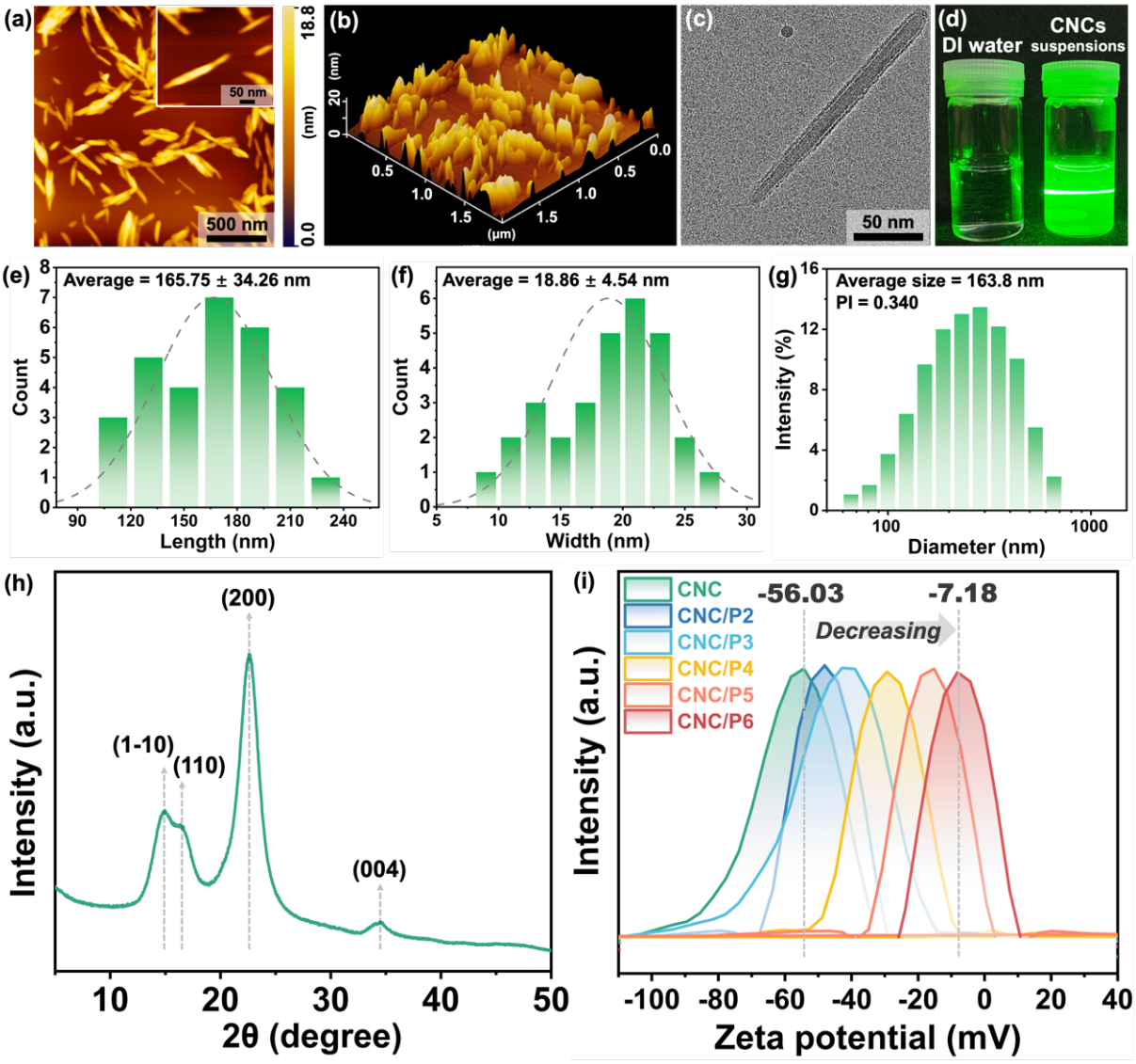

Fig. 3-2. Basic information on CNC and CNC/PEG-PLA suspensions. AFM topography (a) and corresponding 3d image (b) of neat CNCs; TEM image of diluted neat CNCs (c); Typical Tyndall effect owing to the nanosize of neat CNC suspensions (d); Particle size of average length (e) and width (f) measured by AFM; Diameter distribution of neat CNCs (g); XRD pattern of neat CNCs (h); Zeta potential profiles of CNC/PEG-PLA composite suspensions (i).

composite suspension (**Fig. 3-3c**). The observation indicates that the introduction of PEG-PLA did not compromise the stability of the CNC suspensions [56,57]. This was crucial for the subsequent construction of the chiral nematic phase during the EISA process.

The particle size distribution of CNC suspensions was measured by dynamic light scattering (DLS) analysis. The results showed an average length of 163.8 nm and a polydispersity index of 0.34 (**Fig. 3-2g**), which aligned with the AFM results. The XRD pattern of the CNC suspension (**Fig. 3-2h**) revealed characteristic peaks at 15.1°, 16.5°, 23.0°, and

34.5°, corresponding to the (1-10), (110), (200), and (004) lattice planes, respectively, of cellulose I [58,59]. These results verified that the crystalline structure of cellulose remains unchanged during acid hydrolysis, confirming the CNC was obtained successfully.

Surface charge is a crucial factor affecting the stability and diffusion of colloidal dispersions. In the acid hydrolysis of cellulose, sulfuric acid reacts with the hydroxyl groups on cellulose, resulting in the formation of negatively charged sulfate half-ester groups on the CNC. This leads to an overall negative zeta potential in the CNC suspension, thereby enabling its stable dispersion in aqueous media. Moreover, the rod-like CNC with negative sulfate groups can self-assemble into helical chiral nematic structures. Conductometric titration confirmed a sulfur content of 0.75 ± 0.04 wt% in CNC [60,61]. However, as this research involved water-insoluble polyurethane, to avoid phase separation in an aqueous solution during the co-assembly process, the uniform dispersion of the composite suspensions obtained by binary solution mixing fundamentally determined whether the composite film co-assembly process would proceed as expected. In addition, dispersions with different ratios of CNC/PEG-PLA composite suspensions exhibited a uniform and transparent state (**Fig. 3-3a,b**). It is worth mentioning that when we attempted to prepare CNC complex suspensions by directly blending the DMF and CNC suspensions in the desired amounts, the only outcome was the swelling of PEG-PLA in the solvent mixture rather than the formation of a homogeneous CNC composite suspension (**Fig. 3-3d**).

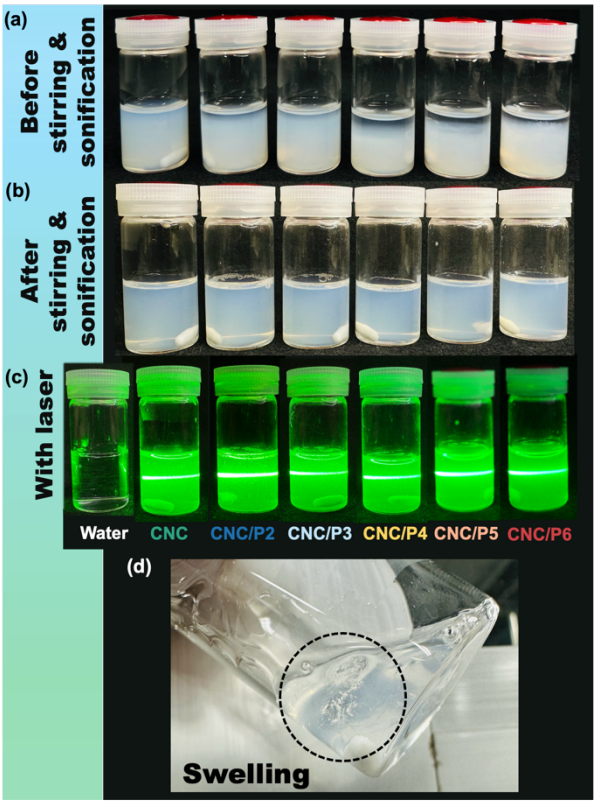

Fig. 3-3. Real-time dispersion stability photographs of CNC suspension (5.58 wt%) blending with different PEG-PLA concentration DMF solutions before (a) and after (b) processing. (c) CNC/PEG-PLA composite suspensions show a noticeable Tyndall effect. (d) The PEG-PLA was swelling when directly added to the DMF solvent and CNC aqueous suspensions.

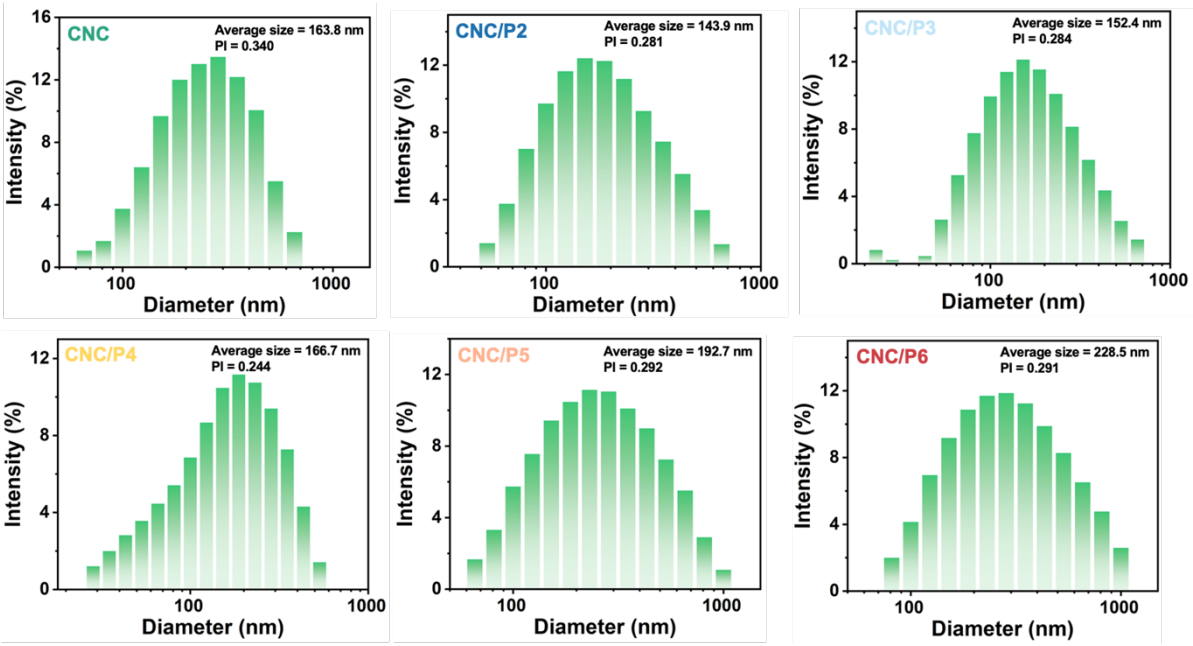

Fig. 3-4. The particle size distribution of CNC/PEG-PLA composite suspension was measured by DLS.

As shown in **Fig. 3-2i**, the dispersion state of the CNC suspension was assessed quantitatively by measuring its zeta potential based on the electrophoretic mobility [62]. The neat CNC exhibited a zeta potential of –56.03 mV. However, upon adding PEG-PLA to the CNC suspension, the zeta potential of the CNC/PEG-PLA composite suspension displayed a decreasing trend, with the absolute value dropping from –56.03 mV to –7.48 mV, which may be explained by the following. The addition of PEG-PLA copolymer to the CNC solution resulted in a decrease in the zeta potential (**Table 3-1**). The PEG-PLA molecular chains effectively wrapped around the CNC particles at a specific concentration, shielding their surface charges and reducing electrostatic repulsion between them. As a result, attractive forces such as van der Waals and hydrogen bonds became more prominent, leading to a further decrease in the zeta potential. The CNC/PEG-PLA composite suspensions maintained a negative charge, which was beneficial for the repulsion between the molecular chains. Moreover, the particle size distribution of the composite suspension increased with PEG-PLA contents (**Fig. 3-4**). This demonstrated the entanglement and bonding between the copolymer and CNC. Thus, a CNC/PEG-PLA composite suspension with a stable dispersion was prepared successfully.

3.3.2 Chemical structure, thermal and crystallization behavior analysis of CNC/PEG-PLA composite films

A simple and effective strategy was proposed to create neat CNC and CNC/PEG-PLA composite films (**Scheme 3-1c**). It introduced a water-insoluble PEG-PLA biodegradable copolymer into CNCs by directly blending two separately preprocessed components. $PEG_{4k}PLA_{1k}$ is a flexible semi-crystalline multiblock copolymer polyurethane.

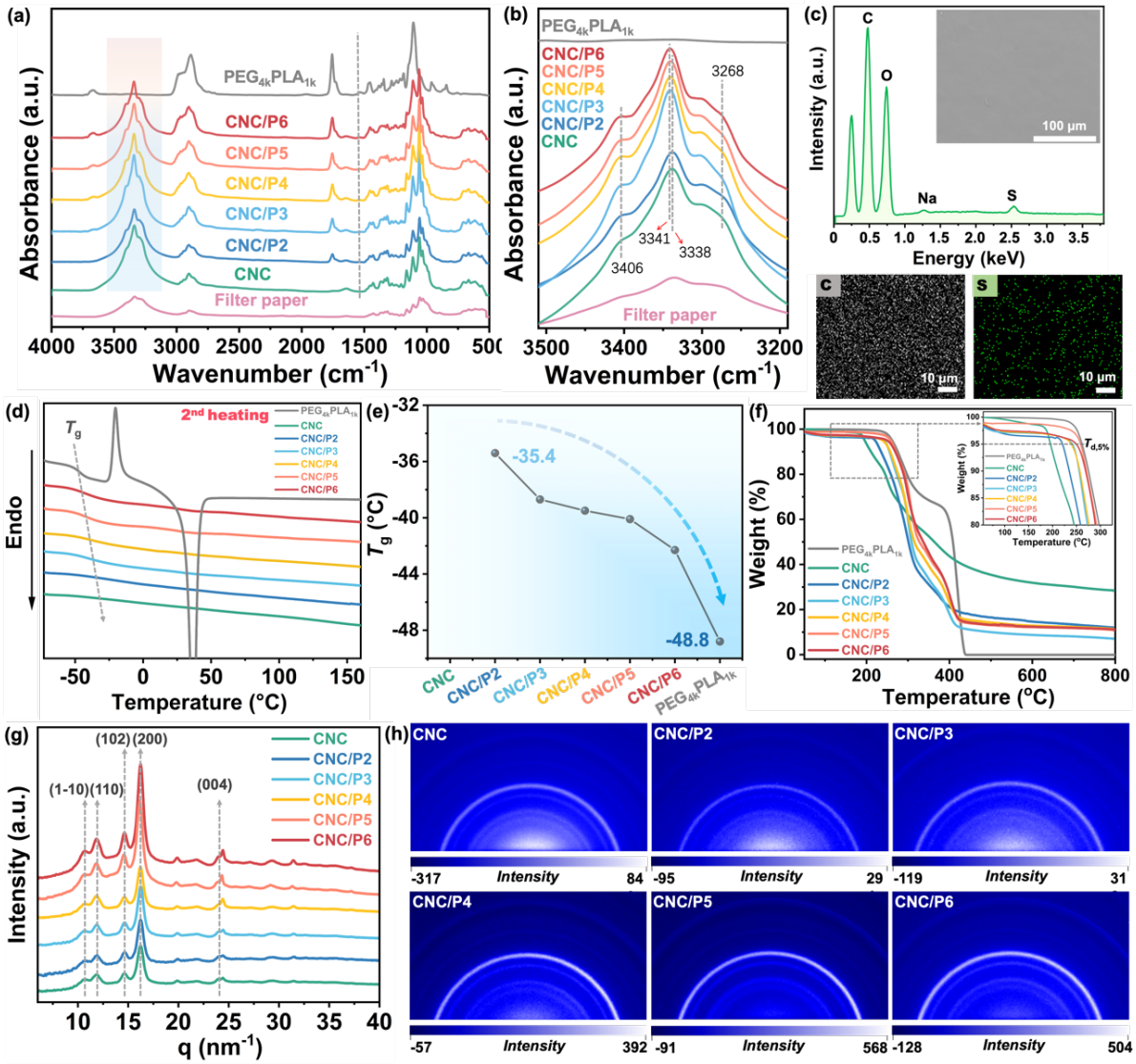

Fig. 3-5. Basic chemical structures and thermal and crystallinity properties of CNC/PEG-PLA composite films. FT-IR spectra (a) and enlarged FT-IR spectra (b); Elemental distribution detected by EDX analysis and mapping of neat CNC film(c); The second heating scan curves of DSC analysis (d); The T_g variation profile obtained by second heating scan of DSC analysis (e); Thermal stability evaluated by TGA analysis (f); 1D profiles (g) and 2D images (h) of WAXS pattern.

Unlike small molecules, the impact of their content on the structure of the composite is worth evaluating. As $PEG_{4k}PLA_{1k}$ is enriched with carbonyl, ether, and amide groups, the CNC surfaces are abundant hydroxyl groups. Therefore, the formation of hydrogen bonds between these is reasonable and was verified by FT-IR (**Fig. 3-5a,b**). In detail, the neat CNC films

exhibited a typical band at 3338 cm^{-1}. This is attributable to the -OH stretching of hydroxyl groups on CNCs. An increase in the $PEG_{4k}PLA_{1k}$ content showed a 3 cm^{-1} shift from 3338 cm^{-1} to 3341 cm^{-1} (CNC/P6). This indicated new interactions between the amide groups of $PEG_{4k}PLA_{1k}$ and the hydroxyl groups weakened the inherent hydrogen bonds of CNC. Also, in the CNC/P6 film, the band at 3268 cm^{-1} reduced and disappeared completely, while a shoulder emerged and increased at the higher wavenumber side of 3405 cm^{-1}. This further demonstrated the weakening internal hydrogen bonds of CNC due to polymer addition. Moreover, the peaks at 1430 cm^{-1} and 1163 cm^{-1} are considered to be representative of the crystalline structure of the cellulose Iβ phase, and the band at 1109 cm^{-1} is assignable to the C−O−C pyranose ring skeletal vibrations of CNCs [63,64]. This suggests that the hydrolysis process did not affect the chemical structure of cellulose, confirming the stable presence of CNC within the composite films [21,65]. The elemental distribution on the surface of the neat CNC film was determined using EDX coupled with FESEM. The EDX spectrum of CNC (**Fig. 3-5c**) displays peaks near 0.5, 0.75, and 2.55 keV. These are associated with the binding energies of carbon, oxygen, and sulfur, respectively (1.25 keV of sodium from the filter paper).

Further studies were conducted on the crystallinity and thermal stability of the neat CNC and CNC/PEG-PLA composite films. **Fig. 3-5d** displays the DSC heating scan curves for the CNC/PEG-PLA composite films. The thermal performance data obtained from the DSC tests are listed in **Table 3-2**. The $PEG_{4k}PLA_{1k}$ within the composite films did not exhibit its characteristic crystallization and melting transitions, possibly due to the inhibition of its crystallization behavior by the EISA process involving interactions with CNC. Nevertheless, the T_g exhibited a decreasing trend with an increase in $PEG_{4k}PLA_{1k}$ content (**Fig. 3-5e**). It ranged from –35.4 °C (CNC/P2) to –48.8 °C (CNC/P6). This indicated that the CNC composites were endowed with enhanced flexibility compared with neat CNC, which is beneficial for practical applications.

The crystalline structures were investigated using 1D (**Fig. 3-5g**) and 2D (**Fig. 3-5h**) WAXS patterns. Upon incorporating $PEG_{4k}PLA_{1k}$, the CNC composite films exhibited diffraction peaks at positions identical to those for the neat CNC. This indicated the preservation of the cellulose I crystal structure. No new diffraction peaks were observed, implying that PEG-PLA existed in an amorphous form. This observation indicates that the composite films retained

the chiral nematic structure, and the CNCs self-assembled with PEG-PLA into periodic structures. This, in turn, verified the DSC observations and was consistent with previous studies. However, the possibility of overlapping diffraction peaks with CNC should be considered. This is because the diffraction peak areas at 16.8 Å and other positions increased with the increase in $PEG_{4k}PLA_{1k}$. Overall, this conserved crystal structure is preferable for maintaining the chiral nematic structure and mechanical strength required for the structural color in the CNC/PEG-PLA composite films. Compared with the neat CNC, the diffraction rings in the 2D WAXS patterns of the CNC composites appeared dimmer. This indicated a decrease in the crystallinity of the composites. This observation aligns with previous studies. It is primarily attributed to the amorphous state of the incorporated polymer [66].

Table 3-2 The thermal characteristics of CNC/PEG-PLA composite films

Samples	T_g [a] (℃)	$T_{d,max}$-CNC [b] (℃)	$T_{d,max}$-PLA [b] (℃)	$T_{d,max}$-PEG [b] (℃)
CNC	- [c]	192.26/250.97	- [c]	- [c]
CNC/P2	–35.4	237.65	295.71	- [c]
CNC/P3	–38.7	260.44	301.31	398.15
CNC/P4	–39.5	265.01	296.52	398.70
CNC/P5	–40.1	271.27	305.54	405.87
CNC/P6	–42.3	- [c]	298.46	403.62
$PEG_{4k}PLA_{1k}$	–48.8	- [c]	293.51	418.96

[a] Obtained from DSC analysis

[b] Taken from TGA analysis

[c] Failed to obtain from DSC or TGA analysis

Furthermore, the microstructure of the CNC/PEG-PLA composite films played a crucial role in their thermal stability, as characterized by TGA (**Fig. 3-5f**). The corresponding data, including the maximum decomposition temperature ($T_{d,\ max}$), are listed in **Table 3-2**. The presence of sulfate groups in CNC films adversely affects their thermal stability [67]. Additionally, the hydrophilicity of the material resulted in the evaporation of water molecules. This implied the essential role of water in the chiral nematic structure and the importance of the

supramolecular arrangement. In the composite films, the $T_{d,\ max}$ of CNC increased from 192.26 °C (CNC) to 271.27 °C (CNC/P5). This improvement in thermal stability can be attributed to the formation of intermolecular hydrogen bonds and the inherently superior thermal stability of PEG-PLA.

3.3.3 Morphology and self-assembly structure analysis of CNC/PEG-PLA composite films

The employed PLA in this chapter is PLLA, which also exhibits chirality. However, the impact of its chirality on the final properties of the composite film is not the focus of this research and will not be discussed. The preservation of the left-handed chiral nematic structure of the CNC/PEG-PLA composite films was confirmed by SEM to observe their cross-section micromorphology (**Fig. 3-6a**). It indicated the successful preparation of iridescent CNC composite films even in the case of CNC/P6 [**Fig. 3-6a(VI)**], which was disrupted and defective but distinguishable. This unique chiral nematic layered structure with a periodic helical pitch (P) was the primary cause for the CNC film's selective reflection of different wavelengths. Bragg's law describes the variation in structural color as illustrated in **Eq. (3-1)** [68]:

$$\lambda_{max} = n_{avg}\, P\, \sin\theta \qquad (3\text{-}1)$$

Here, λ_{max} represents the peak wavelength, n_{avg} is the average refractive index, and P and θ correspond to the chiral nematic pitch and incident angle of light, respectively. When θ is fixed, λ_{max} depends mainly on P for solid CNC films.

A periodic lamellar left-handed chiral nematic structure of the neat CNC film was observed [**Fig. 3-6a(I)**] with a P of 336 nm. For the CNC composite films [**Fig. 3-6a(II,III)**], the adhesion between the CNC rods and PEG-PLA caused relatively blurred boundaries, and the corresponding P increased to 449 nm. The specific data are presented in **Table 3-3**. This implies that PEG-PLA was inserted uniformly into the chiral nematic structure of the CNCs. This expanded the CNC layer space and increased P. As the amount of PEG-PLA increased, local defects appeared in the chiral nematic structure, and the pitch decreased correspondingly. This was similar to the observation of previous research. In semi-crystalline PVA and PEG, local phase separation and crystallization occur when their contents in EISA exceed 40 wt%. This

destroys the chiral structure of CNC and reduces the accurate content of polymers inserted in

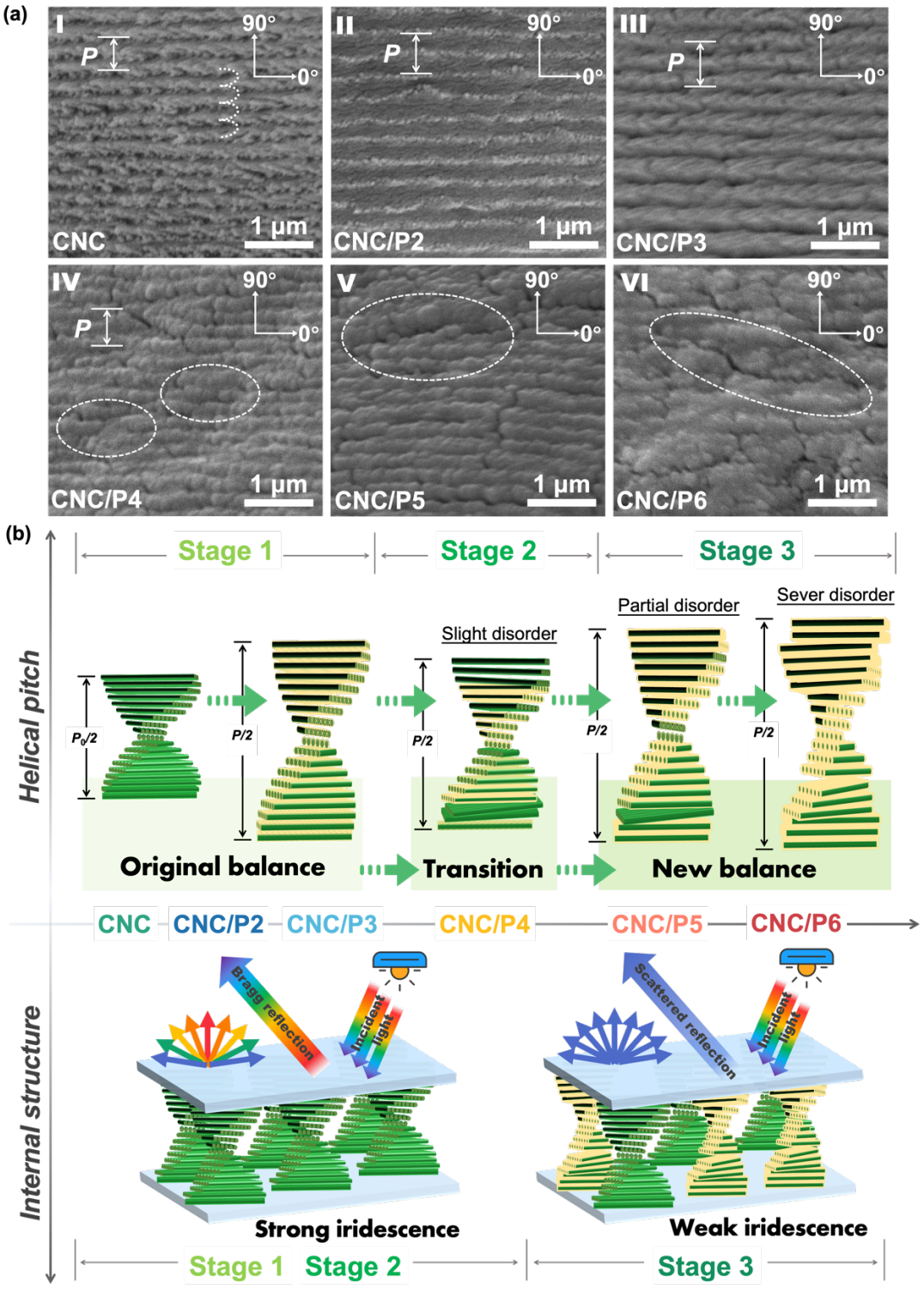

Fig. 3-6. Morphology and self-assembly structure analysis of chiral nematic neat CNC and CNC/PEG-PLA composite films. SEM images of a cryo-fractured cross-section of neat CNC and CNC/PEG-PLA composite films, showing the helical twist of CNCs (a); Schematic diagram of a feasible mechanism for the evolution of the chiral nematic structure and the generation of structural color influenced by the PEG-PLA content (b).

the CNCs [30,39]. With a further increase in PEG-PLA content, the fracture surface of the CNC/PEG-PLA films became irregular and disrupted but still maintained a layered structure. PEG-PLA and CNC can also form physical entanglements through hydrogen bonding and other interactions. This enhanced the flexibility of the composite films [69,70].

Herein, we propose a feasible mechanism for the structural coloration of CNC/PEG-PLA composite films (**Fig. 3-6b**). Due to the presence of sulfate groups, neat CNC spontaneously forms chiral helical layered structures by the EISA process because of electrostatic interactions and other non-covalent forces. After adding a small amount of PEG-PLA, its hydroxyl groups penetrated the nematic layers. These PEG-PLA functioned as uniform dispersants increased the layer space and caused an increase in the reflected wavelength (Stage 1). As the PEG-PLA content increased, the CNC layered structure was disrupted. Here, PEG-PLA underwent local phase separation and crystallization. This reduced the *P* and caused a blue shift (Stage 2). However, as the PEG-PLA content increased, the composite attained a new equilibrium, the pitch expanded, and the structural color shifted back to red. When the contents of PEG-PLA were sufficiently high, its "wrapping effect" destroyed the original periodic chiral helical layered structure of CNC [71]. The DLS and Zeta potential results in **Section 3.3.1** support the statement that the increased PEG-PLA wrapped the CNC. A transition from a state of "long-range order" to "short-range order with long-range disorder" and from Bragg's reflection to scattering reflection was observed (Stage 3). The sensitivity of the structural color variation to the angle also decreased. These microstructural changes confirmed our hypothesis that diverse color reflection types can be achieved in composite films by simply controlling the variation in polymer content. This increases the potential for practical applications.

Additionally, the 2D Fast Fourier Transform (FFT) is an effective tool for understanding structural order while analyzing SEM images [72]. This analytical method converts the geometric structure of a given image from the spatial domain to the frequency domain, thereby yielding sharp spots at specific frequencies. This implied the periodicity of closely packed ordered colloidal particles. The sharp spots confirmed that the ordered CNCs were packed tightly within the crystalline structure. In contrast, the circular patterns corresponding to the sharp peaks signified an ordered structure of closely packed colloidal particles. There became annular in the power spectrum with the introduction of PEG-PLA, causing the disappearance of the sharp

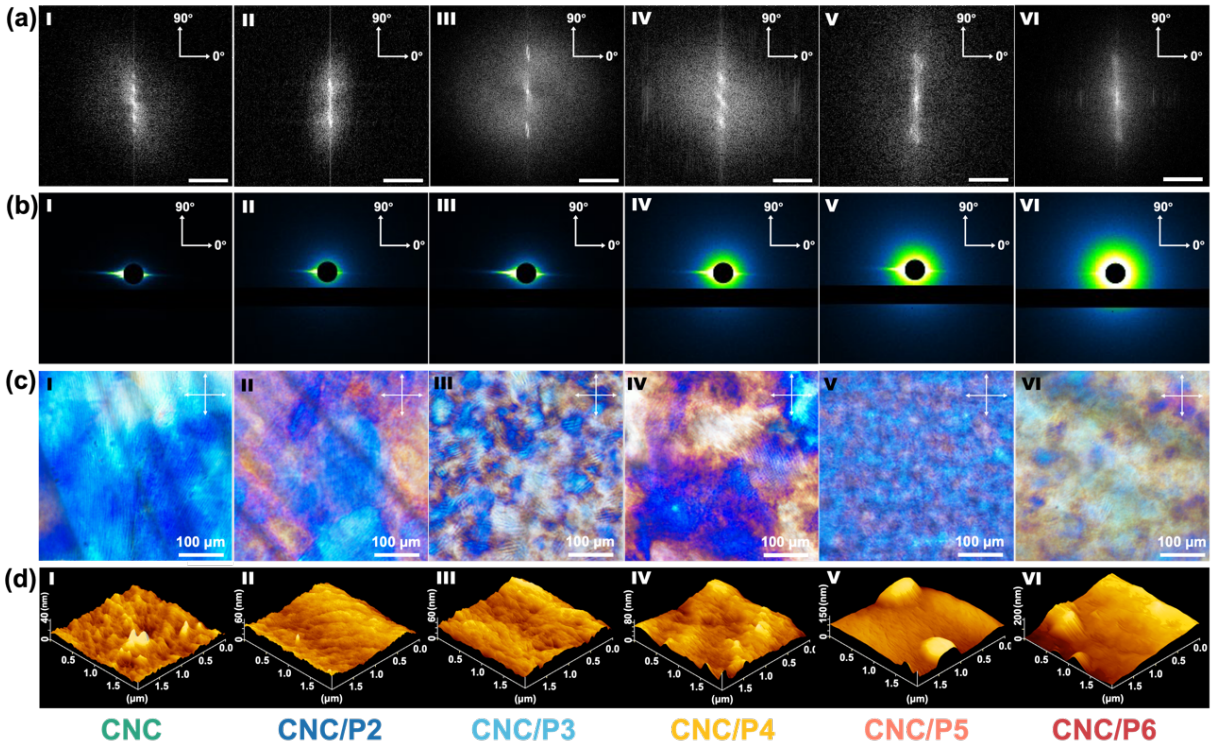

Fig. 3-7. Morphology and self-assembly structure analysis of chiral nematic neat CNC and CNC/PEG-PLA composite films. 2D-FFT images obtained from SEM images (a); 2D SAXS intensity patterns displaying the anisotropic orientation (b); POM images with apparent fingerprint textures taken with crossed polarizers (c); Surface morphology of 3D AFM images (d).

peaks (**Fig. 3-7a**). Moreover, as the amount of PEG-PLA increased, the ring-like power spectrum dispersed further. This suggested that the addition of PEG-PLA gradually lowered the periodic order of the CNCs. This allowed for the constructive interference of scattering phases, other frequency destructive interference, and the angle dependence/independence properties of the CNC/PEG-PLA composite films. This demonstrates that adding PEG-PLA can modulate the structural order and color of CNC composite films. Furthermore, 2D SAXS analysis was employed to observe the cross-section of the CNC composite film to demonstrate their orientation alignment **(Fig. 3-7b**). With an increase in PEG-PLA, the SAXS diffraction pattern transitioned from sharp rhomboidal shapes to a short and indistinct meridional annular pattern, yet sharp rhomboidal diffraction was still observable. This indicated the anisotropic orientation of the cellulose chains. The introduced PEG-PLA did not destroy the CNC orientation. However, it gradually weakened the reflection caused by this orientation within the composite films.

To understand the relationship between the structure and color of the CNC/PEG-PLA composite films with varying mass ratios and to elucidate the mechanism for controllable

iridescence, POM was employed to observe the micro-nanostructure of the composite films **(Fig. 3-7c)**. When neat CNC films were observed under a microscope in the transmission mode between crossed polarizers, the emergence of a fingerprint texture, which signified the inherent birefringence of chiral nematic liquid crystals. The phenomenon was also apparent in the CNC/PEG-PLA composite films. This verified that CNC was still assembled into a helical layered structure characteristic of composite films and that the addition of PEG-PLA had a negligible effect on the structure of the CNC composite films. However, differences were observed between the groups. The existence of the fingerprint texture revealed the pitch of the helical structure, i.e., the distance between two adjacent plane textures. It increased dramatically with the PEG-PLA content from 0.711 ± 0.008 μm (CNC) to 0.795 ± 0.011 μm (CNC/P2) and 0.913 ± 0.005 μm (CNC/P3). This phenomenon could also have caused the redshift in the reflected wavelength [73]. Micro-phase separation occurred with a further increase in the PEG-PLA content (CNC/P4). The POM micrographs showed multiple pitch textures and non-uniform color distribution owing to the excessive polymers in CNC. These caused the separation and destruction of the long-range ordered mesophase. CNC/P5 displayed a multi-domain structure [**Fig. 3-7c(V)**]. It was enlarged with an increase in PEG-PLA content, thereby potentially affecting the crystallinity, thermal stability, and mechanical properties of the composite films.

As presented in **Fig. 3-7d**, AFM was used to observe the surface roughness of the CNC composite films. These gradually became smoother with the increase in PEG-PLA content, indirectly demonstrating the "wrapping effect" on the CNC surface. The corresponding SEM results also showed similar variations in the surface morphology (**Fig. 3-8**), which inherently affected the optical properties of the CNC/PEG-PLA composite films.

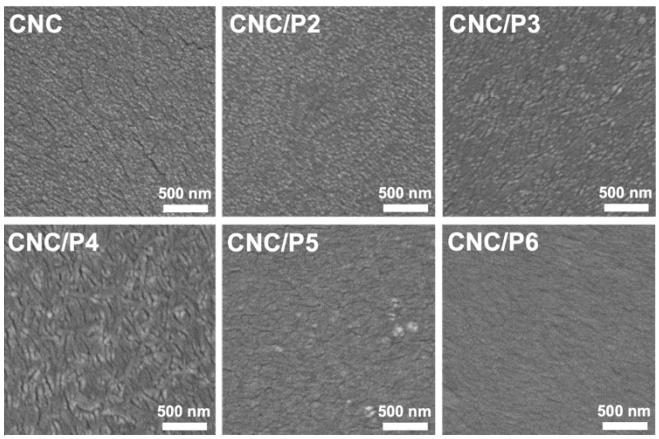

Fig. 3-8. SEM images of surface morphology of neat CNC and CNC/PEG-PLA composite films.

3.3.4 Evaluation of optical properties of CNC/PEG-PLA composite films

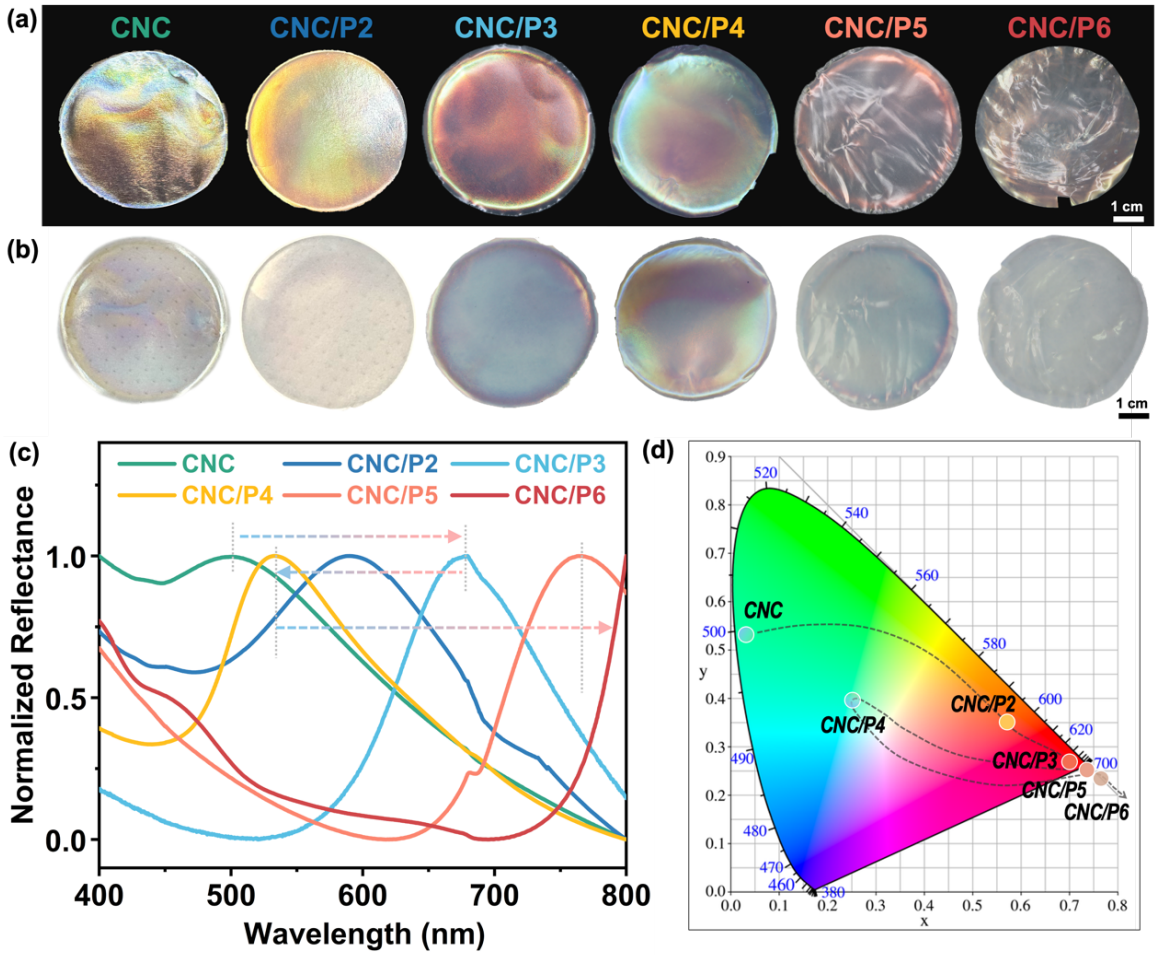

Fig. 3-9. Optical properties of chiral nematic CNC/PEG-PLA composite films. Digital photographs under black (a) and white (b) backgrounds presenting the different iridescence due to structural coloration; λ_{max} of UV-vis reflection spectra (c) and CIE 1931 color space chromaticity diagrams (d) for films with color-changing by varying compositions.

The CNC/PEG-PLA composite films selectively reflected specific wavelengths of light due to their periodic helical arrangement of the liquid crystal cholesteric structure [74]. The background color is important for creating colorful materials. The coloring mechanism of structural color depends on the base color, such as black or white. Its appearance against a black background under natural light perpendicular to the surface of the CNC composite film is shown in **Fig. 3-9a**. The neat CNC film reflected a bright iridescence to the naked eye with blue-green colors. With an increase in PEG-PLA, the color gradually redshifted to yellow (CNC/P2) and orange-red (CNC/P3), blueshifted to blue-yellow (CNC/P4); then to red (CNC/P5); and almost faded (CNC/P6). This covered nearly the entire visible spectrum. Correspondingly, the appearance was almost transparent on a white background (**Fig. 3-9b**) except for CNC/P4. The color variation mechanism for black and white backgrounds is illustrated in **Fig. 3-10**. White

light displays three primary colors: blue, green, and red. The black background of CNC/P3 presents an orange-red color due to the absorption of green and red light by the black background (**Fig. 3-10a**). This resulted in the reflected orange-red. In contrast, when the background was white, the reflection intensity from the background was high across the entire visible region. It displayed a light blue-violet to transparent color (**Fig. 3-10b**). This is because the red light was reflected from the surface, and the white base refracted the absorbed light, which yielded a light blue-violet composite color [75,76].

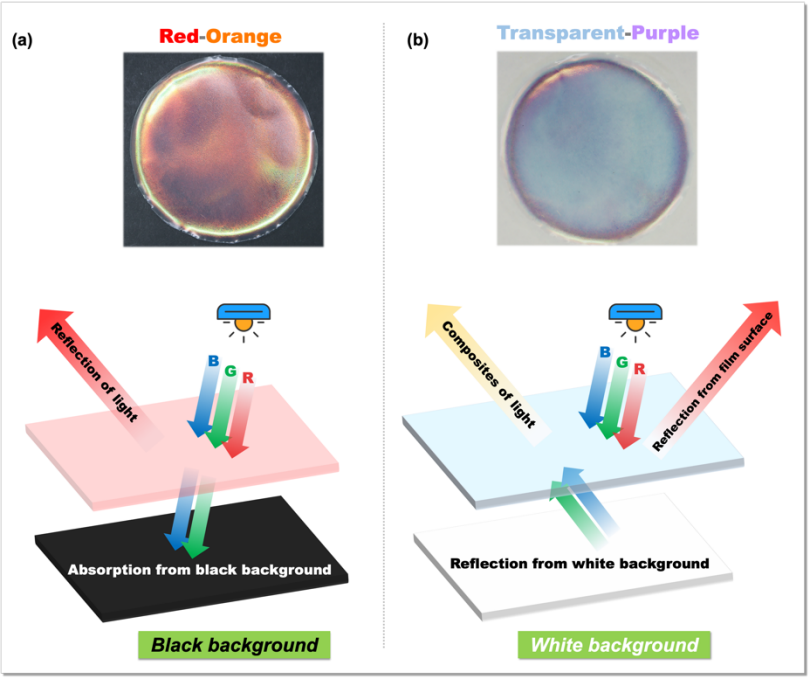

Fig. 3-10. Digital photos and mechanism of structural coloration under black (left) and white (right) background of CNC/P3 composite film.

According to Bragg's law, because the film color variations correspond to the variation in *P* affecting the reflected wavelength, **Fig. 3-9c** shows the UV-vis reflection spectra and the variations in λ_{max} with PEG-PLA content. The reflection peak shifted from 498 nm (CNC) to 589 nm (CNC/P2) and 686 nm (CNC/P3), then blueshifted to 533 nm (CNC/P4) and conversely redshifted to 755 nm (CNC/P5) and >800 nm (CNC/P6). This implied that the increase in PEG-PLA content disrupted the cholesteric helical structure. The λ_{max} calculated by the *P* values measured by SEM into **Eq. (3-1)**, with sin θ set to 1, is close to the actual λ_{max} recorded by the UV-vis reflection spectra, as shown in **Table 3-3**. The calculated λ_{max} is consistent with the actual λ_{max} and follows a similar variation. To reveal the effect of the PEG-PLA content on the visualized structural coloration, the UV-vis absorption spectra were converted directly into the Commission Internationale de l'Éclairage (CIE) chromaticity diagram (**Fig. 3-9d**). The results obtained using this commonly used color analysis method align well with the visually observed colors. Combined with the previous SEM, FFT, and 2D SAXS results, despite the amorphous polymeric structural defects in the intermediate layer, it was found that CNC/P6 still retained a

certain ordered layered structure. Overall, this simple and effective co-assembly method enabled the fabrication of CNC-based composite materials with tunable chiral nematic structures by combining CNC and water-insoluble polymer. By altering the PEG-PLA content in the composite films, the structural variations caused tunable reflective color and intensity.

Table 3-3 The comparison of the maximum reflected wavelength (λ_{max}) calculated by SEM and UV-vis reflection spectra

Samples	n_{avg}	P [a] (nm)	λ_{max} [a] (nm)	λ_{max} [b] (nm)	Color
CNC	1.54	336 ± 15	517 ± 23	498 ± 12	Blue–Green
CNC/P2	1.53	393 ± 11	601 ± 17	589 ± 8	Green–Yellow
CNC/P3	1.52	449 ± 8	682 ± 12	667 ± 6	Orange–Red
CNC/P4	1.52	364 ± 30	553 ± 46	531 ± 34	Blue–Yellow
CNC/P5	1.52	- [c]	- [c]	735 ± 21	Red
CNC/P6	1.51	- [c]	- [c]	>800	Red–Colorless

[a] Indicates calculated by SEM, $\lambda_{max} = n_{avg} P \sin\theta$, $\theta = 90°$

[b] Indicates λ_{max} obtained from UV-vis reflection spectra

[c] Indicates failed to calculate

Chiral nematic self-assembly CNC films exhibit selective left-handed circular polarization characteristics [77]. To verify this phenomenon, a filter was used to pass non-polarized light through a left-handed circularly polarized filter (L-CPF) or right-handed circularly polarized filter (R-CPF) interacting with the CNC/PEG-PLA film, and the direct visualizable optical activity under processed CPL was evaluated. The CNC/PEG-PLA composite films exhibited recognizable reflection under L-CPF (**Fig. 3-11a**). This indicated that the composite films retained a selective reflection of left-handed CPL. The intensities of the reflection spectra were recorded using UV-vis spectroscopy. As shown in **Fig. 3-11b**, after L-CPF processing, the CNC composite films displayed a strong reflection peak. In contrast, the corresponding reflection peak weakened or even disappeared with the R-CPF. These results revealed that CNC/PEG-PLA can reflect left-handed CPL. This is consistent with the anticipated retention of the left-handed chiral nematic of CNCs.

Moreover, the anisotropic PBG allows light to reflect at specific wavelengths. Therefore, CNC/PEG-PLA composite films with a particular composition can exhibit varying structural colors at different viewing angles (**Fig. 3-11c**). CNC/P4 [**Fig. 3-11c(II)**] presented an orange-

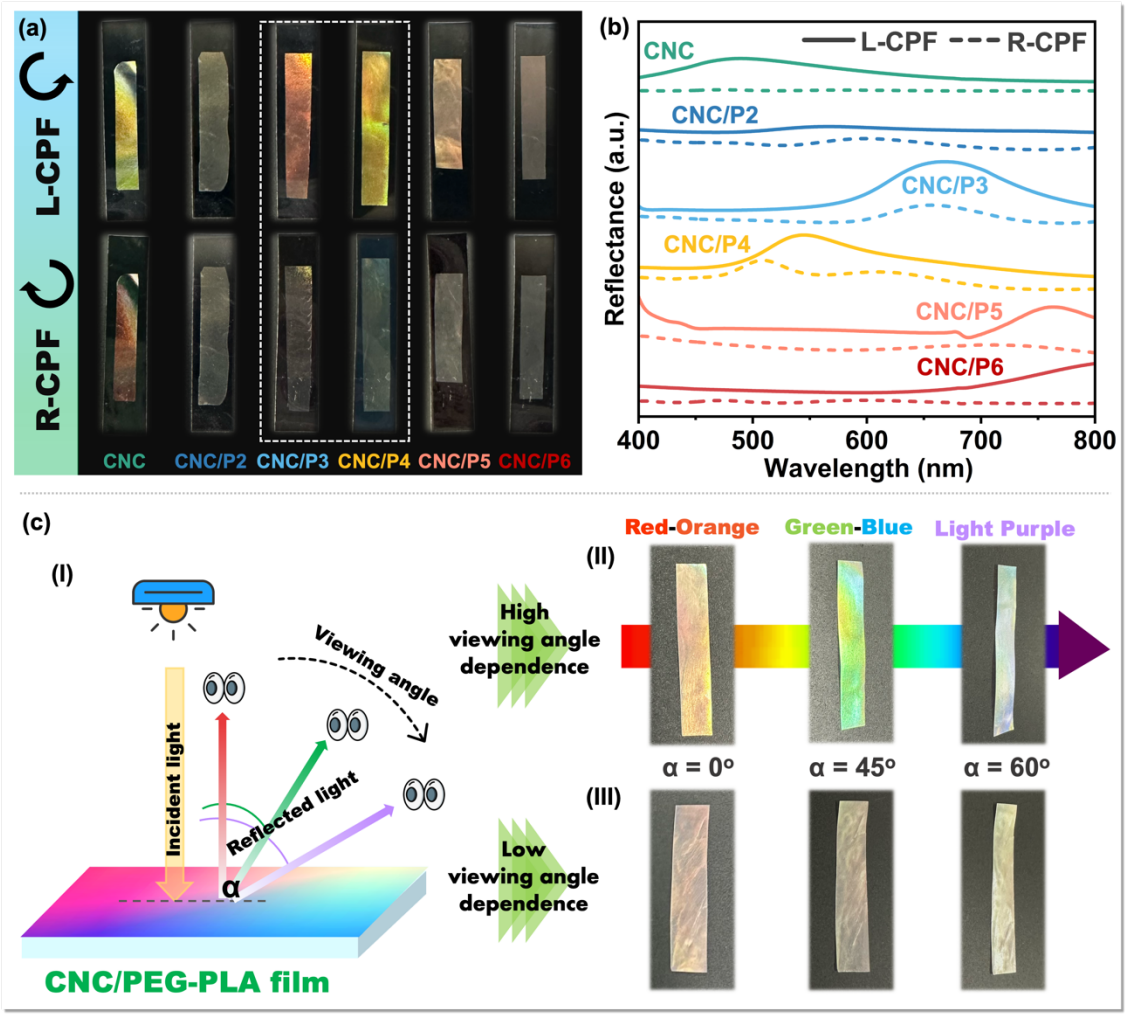

Fig. 3-11. Structural coloration response to different conditions. (a) Digital photographs and (b) reflection spectra of CNC/PEG-PLA composite films covered by L-CPF and R-CPF; (c) Schematic illustration of the observation at different viewing angles (i); Digital photographs of CNC/P4 (ii) and CNC/P6 (iii) at various viewing angles.

red color at 0°. However, the color shifted gradually to light purple as the viewing angle increased. According to the Bragg–Snell formula as **Eq. (3-2)** [78]:

$$\lambda_{max} = 2d\sqrt{(n_{eff}^2 - \sin^2\alpha)} \qquad (3\text{-}2)$$

Here, λ_{max} represents the peak wavelength, α is the observation angle from the normal to the reflective surface, n_{eff} is the effective refractive index, and d corresponds to the $P/2$, respectively. For solid CNC films, when d is fixed, it mainly depends on the value of α, and λ_{max} decreases as the α viewing angle increases [**Fig. 3-11c(I)**]. Therefore, the color variation of CNC/P4 can be explained well. However, as the PEG-PLA content increased, CNC/P6 showed an almost low angle-dependent color variation [**Fig. 3-11c(III)**]. This can be explained by the transition from ordered to disordered structures and strong light scattering. Owing to the increase in the

scattering effect, the color saturation and brightness decreased. These results verify that introducing PEG-PLA can induce a transition from an iridescent structural color to a low or even angle-independent structural coloration. This is consistent with the discussion of the structural variations in **Section 3.3.3**.

3.3.5 Mechanical properties of CNC/PEG-PLA composite films

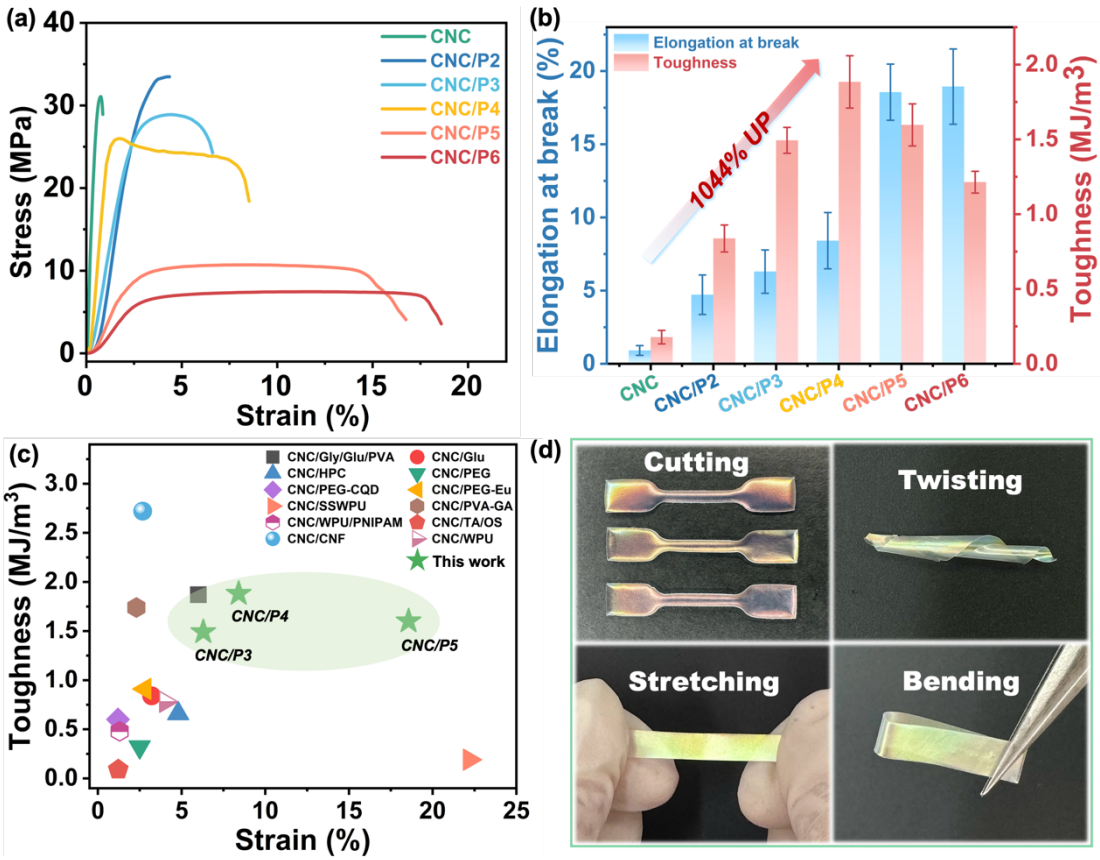

Fig. 3-12. Mechanical properties of CNC/PEG-PLA composite films. Typical engineering stress-strain curves (a); Bar charts of elongation at break and toughness (b); Ashby plot in terms of toughness vs tensile strain of CNC/PEG-PLA films and the previously reported CNCs-based chiral nematic films (c). The CNC/P4 with excellent mechanical properties can be cut, stretched, bent, and twisted as desired under the action of an external force (d).

For practical applications, it is essential to evaluate the mechanical properties of the CNC composite films. The ultimate tensile strength (σ_m), elongation at break (ε_b), and toughness of CNC composite films with varying PEG-PLA contents were assessed through the tensile test, as shown in **Fig. 3-12a,b**. The corresponding data are listed in **Table 3-4**. The neat CNC film exhibited low ε_b and toughness of 0.91 ± 0.33% and 0.18 ± 0.05 MJ/m^3, respectively. It displayed brittleness and low water resistance due to the absence of a flexible energy-

dissipating phase. This severely hinders their practical application. For CNC/PEG-PLA composite films, the introduction of PEG-PLA significantly influenced their σ_m and ε_b during fracture. This is primarily attributed to the plasticization between the rigid CNC and PEG-PLA, the formation of appropriate hydrogen bonds, and the inherent flexibility of PEG-PLA. The SEM images (**Fig. 3-6a**) of the fracture cross-sections further support the toughening mechanism after adding PEG-PLA. The fracture surface of neat CNC was smooth, whereas that of CNC/PEG-PLA exhibited increased roughness and amorphous defect structures with the growing polymer. It has been reported that a rougher fracture surface implies higher energy dissipation during the fracture process. This improves the toughness of the material. The amorphous phase acted as an energy-dissipating binder phase, which rendered the iridescent CNC composite films more ductile. Remarkably, CNC/P4 exhibited plastic deformation, and it facilitated the dissipation of fracture energy and displayed high toughness (1.88 ± 0.16 MJ/m^3) among the composites. It was capable of free cutting, bending, and 360° twists without breaking (**Fig. 3-12d**). CNC/PEG-PLA composite films demonstrated significant improvements in strength and toughness compared with the neat CNC. Their mechanical performance was compared with previously reported CNC-based films, as shown in **Fig. 3-12c** [29,33,35,79–89]. To our knowledge, similar superior toughness has not been achieved in previous studies on non-chemically crosslinked CNC composite films, and this remarkable toughness would be advantageous for various practical applications. Thereby, it would promote the development of high-performance CNC-derived chiral materials.

Table 3-4 Mechanical properties of CNC/PEG-PLA composite films

Samples	Toughness (MJ/m^3)	Young's modulus E (GPa)	Tensile Strength σ_m (MPa)	Elongation at break ε_b (%)
CNC	0.18 ± 0.05	7.40 ± 1.12	31.86 ± 8.34	0.91 ± 0.33
CNC/P2	0.84 ± 0.09	1.56 ± 0.33	32.63 ± 5.51	4.72 ± 1.35
CNC/P3	1.49 ± 0.09	1.36 ± 0.24	29.87 ± 3.66	6.30 ± 1.48
CNC/P4	1.88 ± 0.16	2.97 ± 0.17	24.40 ± 4.29	8.11 ± 1.92
CNC/P5	1.60 ± 0.14	0.42 ± 0.08	11.58 ± 2.37	18.56 ± 3.03
CNC/P6	1.214 ± 0.07	0.31 ± 0.03	8.02 ± 1.28	18.94 ± 2.57

3.3.6 Sensing performance of CNC/PEG-PLA composite films

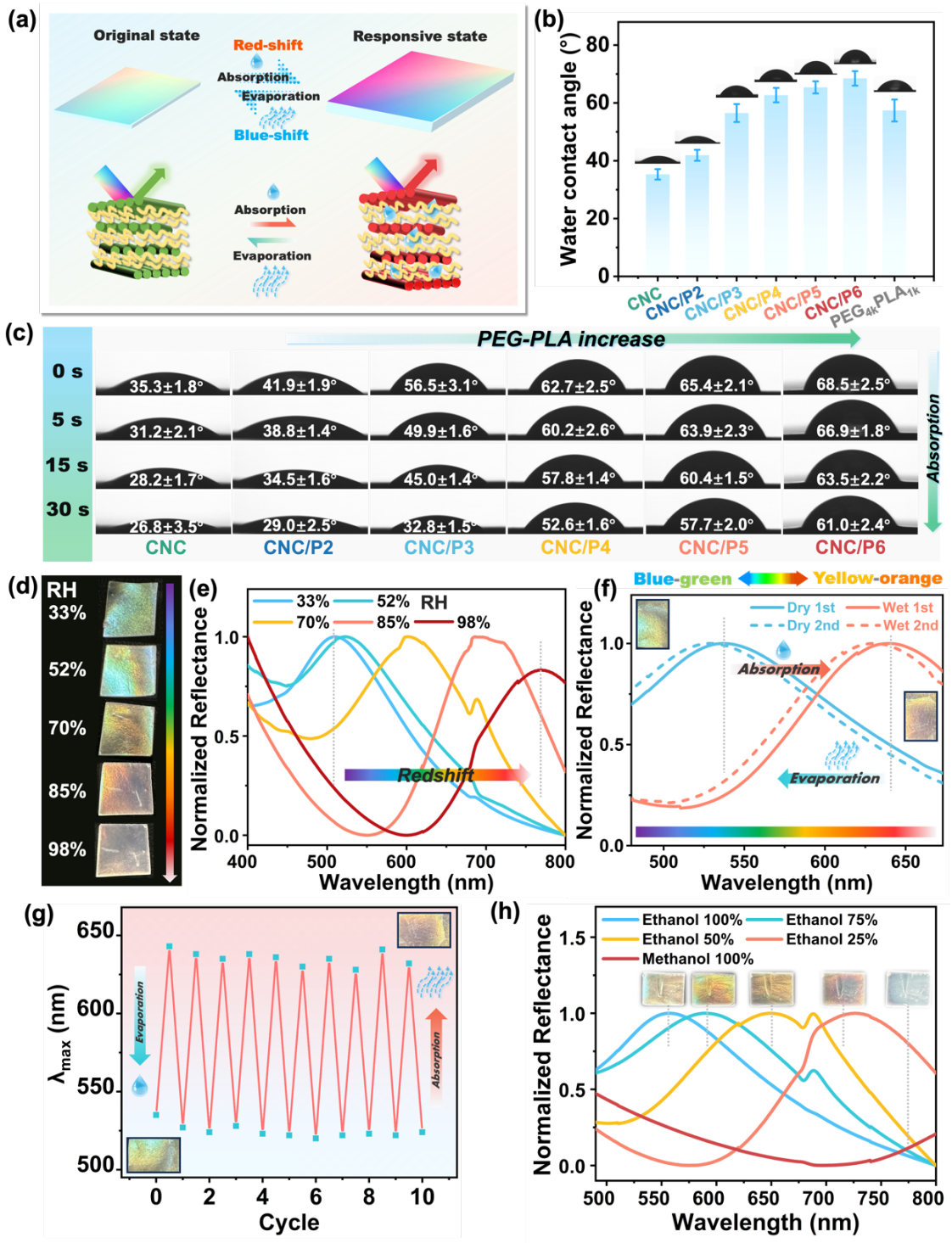

Fig. 3-13. Evaluation of sensing performance of responsive chiral nematic CNC/PEG-PLA composite films. Schematic illustration of helical pitch affected by RH and solvents of swelling and deswelling process (a); Bar charts of water contact angles (b); Comparison of time-dependent water contact angle (c); Exposed at different RH environments (d) and UV-vis reflection spectra (e); UV-vis reflection spectra and appearance of CNC/P4 before and after immersion in mixed ethanol/water (30:70 v/v) (f); Reversible responsive process within 10 cycles (g); Transitions of UV-vis reflection spectra and appearance of CNC/P4 after immersed in ethanol/methanol binary solvents with different volume ratios (h).

These may be potentially applicable as sensors because of the exceptional mechanical properties, thermal stability, and chiral nematic structural coloration of the CNC composite films. Due to the abundance of free hydroxyl groups, hydrophilic self-assembled CNC films exhibit exceptional water absorption and swelling capabilities [90]. Moreover, $PEG_{4k}PLA_{1k}$ has been proven to possess exceptional water absorption properties [47]. This allows these to visibly display variations in the reflected color in response to external stimuli such as variations in humidity and different solvents (**Fig. 3-13a**). Wettability is a crucial surface parameter that significantly determines the molecular transportation and function of a film. Hence, I first examined the hydrophilicity of the CNC/PEG-PLA composite films using WCA tests. As shown in **Fig. 3-13b**, within an equal duration of water absorption, the WCA in the composite films increased with the PEG-PLA content from 35.3° ± 1.8° (CNC) to 68.5° ± 2.5° (CNC/P6). CNC/P4, CNC/P5, and CNC/P6 all reach 60° but lower than 70°, maintaining relatively hydrophilic surfaces. On the other hand, as depicted in **Fig. 3-13c**, the WCA of the neat CNC film decreased from 35.3° ± 1.8° to 25.8° ± 3.5° after 30 s due to its high hydrophilicity, which facilitated the diffusion of water molecules into the film and disrupted the hydrogen bonds between individual CNCs. In contrast, the WCA of CNC/P3 dropped from 56.5° ± 3.1° to 34.8° ± 1.5°. This could be explained by 1) the improvement of this process by the excellent water uptake capability of PEG-PLA and 2) the presence of components with different hydrophilicity abilities of CNC, PEG, and PLA in the composite films, which created a microstructure capable of producing a "self-pumping effect" [91] and thereby promoted the diffusion of free water molecules and their adsorption in the pores of the iridescent composite films. The time-dependent WCA further confirmed the satisfactory water response of the hydrophilic CNC/(PEG-PLA) composite films.

With a wide range between the UV-vis reflection peak and the invisible spectral region, as well as the favorable mechanical properties of the CNC/P4 composite, the response of CNC/P4 to different RH environments was studied (**Fig. 3-13d**). When the RH increased from 33% to 98%, the structural color of CNC/P4 underwent a noticeable variation due to the redshift by water absorption. It returned to its original color when the RH environment was removed. The corresponding UV-vis reflectance spectra are shown in **Fig. 3-13e**. The mechanism of the

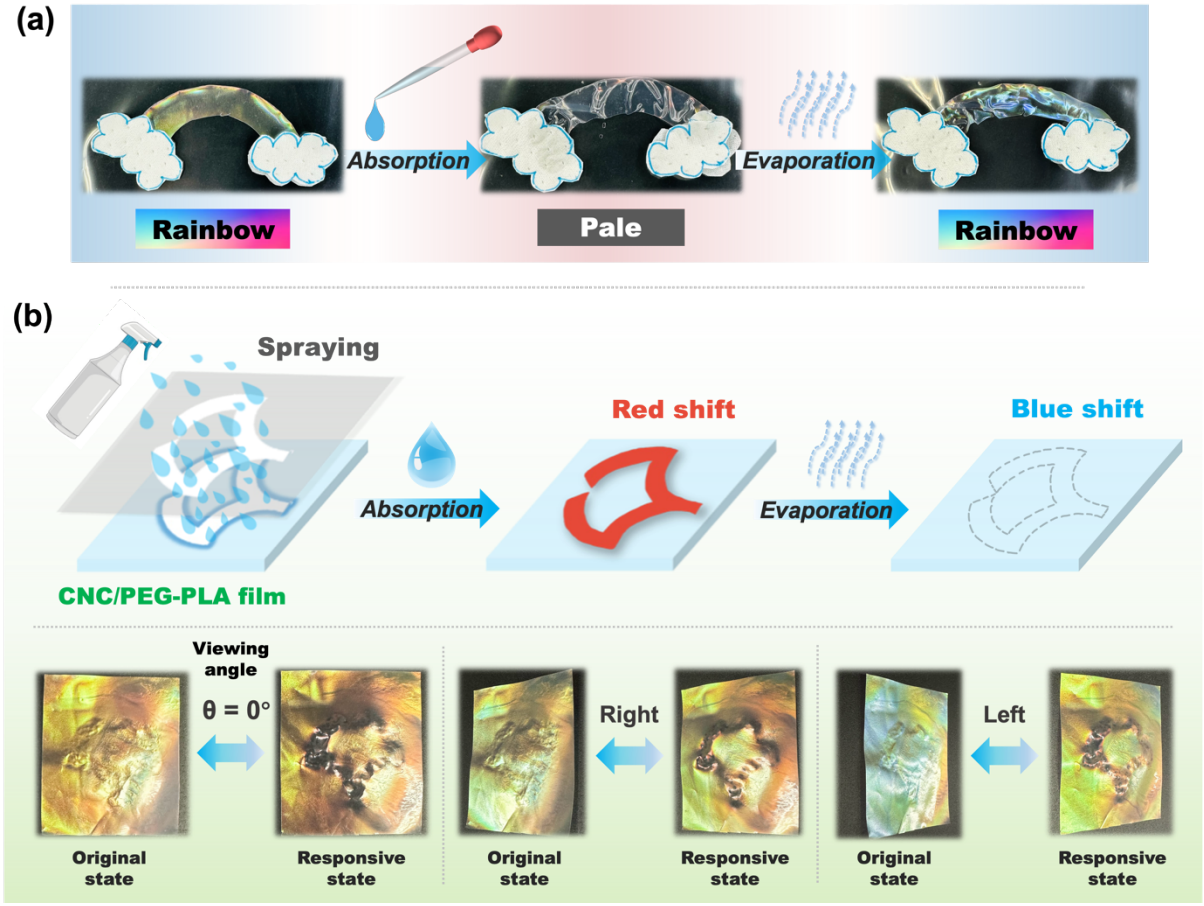

Fig. 3-14. (a) Water-responsive process of CNC/P4 composite films. (b) Ethanol/water (15:85 v/v) mixing solvent-responsive process of CNC/P4 with Osaka University's emblem hollow-out pattern.

color variation of the CNC composite films in response to various RH is illustrated in **Fig. 3-13a**. In addition, upon immersion in DIW, CNC/P4 exhibited a rapid color variation response. It reached equilibrium within 18 s, significantly improving compared with previous research [30,92]. Meanwhile, the response selectivity to common organic solvents was evaluated. After 24 h of immersion, the CNC composite films showed almost no response to acetone, $CHCl_3$, or THF, whereas ethanol showed a slight redshift. Acetic acid and methanol exhibited a notable redshift to red and transparent. The equilibrium response time for methanol was 40 s.

Water caused a tremendous color change because the film swelled to its maximum extent in pure water. Although CNC/P4 displayed reversible structural coloration after pure water evaporation, the structure of the composite film was damaged irreversibly (**Fig. 3-14a**). An ethanol/water mixture (15:85, v/v) was unsuitable for reversible applications (**Fig. 3-14b**). Therefore, the response behavior of the film was verified using an appropriate ethanol/water

(30:70, v/v) mixed solvent. **Fig. 3-13f** illustrates the reversible variations in the λ_{max} of CNC/P4 upon alternating absorption and evaporation of the solvent. Fatigue was not observed after over 10 cycles (**Fig. 3-13g**). This indicated an outstanding and robust reversible structural color stability and improved humidity sensitivity in the CNC composite film. Furthermore, the biodegradability of CNC and PEG-PLA is advantageous for environmental protection [93,94]. Thus, I used a simple swelling dissolution test to investigate the potential degradation behavior of the CNC/PEG-PLA composite films. As shown in **Fig. 3-15**, the CNC and CNC composite films exhibited swelling after being immersed in DIW at room temperature for 10 min, nearly disintegrated after 2 h, and dissolved after 24 h. This provides a convenient and environmentally friendly strategy for recycling iridescent CNC-based composite materials.

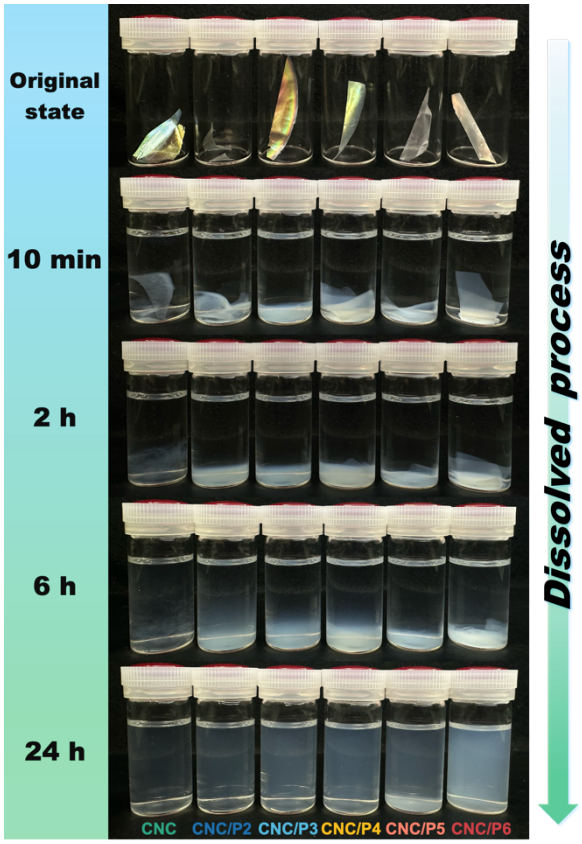

Fig. 3-15. Fast dissolution behavior of CNC and CNC/PEG-PLA composite films in DIW at ambient environment.

Conveniently distinguishing methanol from ethanol is challenging because their properties are similar to their homologs. Therefore, methanol detection is vital for daily life, industrial alcohol production, and environmental monitoring. **Fig. 3-13h** compares the color variations of CNC/P4 under ethanol/methanol mixing solvents with different volume ratios and the corresponding variation in the λ_{max} of UV-vis reflection spectra. In detail, methanol and ethanol caused a redshift of CNC/P4, shifting the λ_{max} to higher wavelengths. However, the degree of response was more extensive for methanol During the response process, as the methanol ratio increased, the color of the CNC/P4 gradually changed from its original cyan-yellow to orange, red, and eventually transparent in 100% methanol. This indicates that the visual distinction between methanol and ethanol is feasible. When the CNC/P4 reached its maximum response

state, it was removed from the solvent and exposed to fresh air. The color and maximum reflection wavelength shifted gradually to blue due to the rapid evaporation of the solvent. This revealed a tremendous reversibility. Moreover, a strong linear correlation (correlation coefficient ($R^2 = 0.97$), was identified between the methanol content and the redshift of the UV-vis reflection peak. It is reasonable to expect that the CNC composite films may practically serve as visual indicators of RH variations and methanol content in mixed solvents.

3.3.7 Multiple information storage and encryption applications of CNC/PEG-PLA composite films

Utilizing their superior optical and sensing performance and exceptional mechanical properties, a multi-encrypted system with reversible color variations can be created by combining the sensing capabilities of CNC composite films with different viewing angles and backgrounds. Because of the varied response speeds and sensitivities of the CNC composite films to water (**Fig. 3-16**), the CNC composite films with higher and lower responses to the ethanol/water (30:70, v/v) mixed solvent were cut into the same size. These were arranged precisely into an array of color blocks that are unidentifiable under natural light but can reveal visually identifiable information in the specific solvent (abbreviation "**OU**" symbol for Osaka University). As the solvent evaporated, the information became unidentifiable again. This resulted in reversible encryption (**Fig. 3-17a**).

Fig. 3-16. The reversible solvent-responsive process of neat CNC and CNC/PEG-PLA composite films shows the different coloration ranges and response speeds.

To further enhance the encryption complexity, CNC composite films displaying different colors against different viewing angles, CPL, and backgrounds were utilized as encoding

elements. This incorporated the unique encoding technique of the Caesar cipher for information encryption and decryption (**Fig. 3-17b**). By establishing color-coding rules (the identified

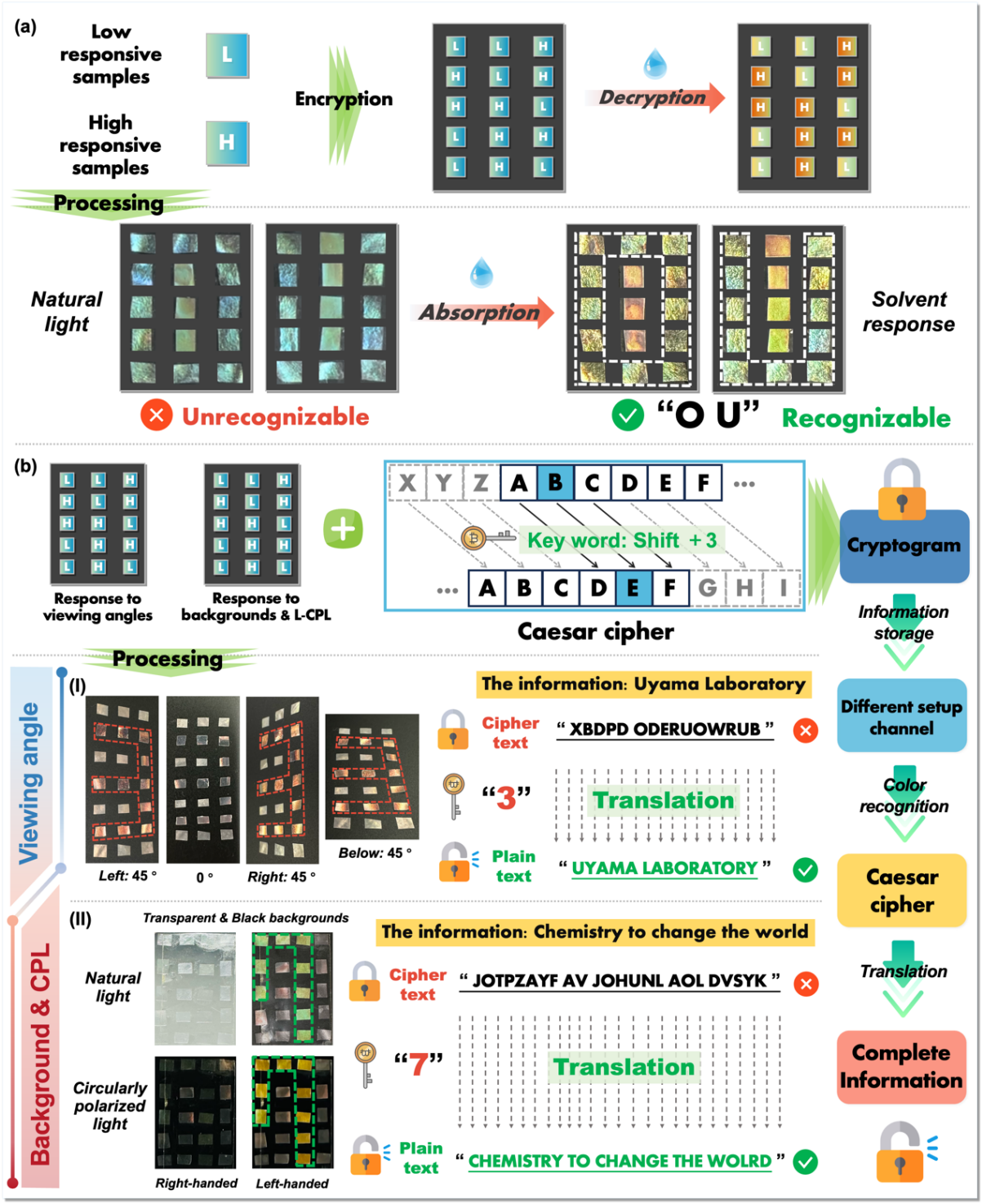

Fig. 3-17. Applications for multiple information storage and encryption. (a) Schematic illustration of design (top) and operation (bottom) of the information "OU" encryption and decryption by a specific solvent; (b) Multiple information encryption based on multi-stimuli conditions and cipher coding. Only the authentic information can be recognized under certain viewing angles with natural light (I) and different backgrounds or circularly polarized light (II).

number serving as the Caesar cipher's shift keyword) and encoding information, encoding arrays based on the strong and weak reflective responses to angle variations and arrays that display distinguishable structural colors against different backgrounds or different polarized lights were created. These can be visually identified under the corresponding decryption channels to obtain the shift keyword. Meanwhile, the color under natural light covers and protects the authentic information. According to the defined decryption rules, the unreadable information "**XBDPD ODERUOWRUB**" and "**JOTPZAYF AV JOHUNL AOL DVSYK**" were translated using the obtained shift keywords "**3**" [**Fig. 3-17b(I)**] and "**7**" [**Fig. 3-17b(II)**], thereby revealing the preset authentic information "**UYAMA LABORATORY**" and "**CHEMISTRY TO CHANGE THE WORLD**". This allows for different keys for each piece of information, which, in turn, increases the difficulty of decryption and demonstrates the tremendous potential of a sophisticated multi-encrypted system. Considering the complexity of the coding system and its large information capacity, this multi-encoding strategy offers a potential pathway for information storage and communication security.

3.4 Conclusions

In summary, by incorporating water-insoluble PEG-PLA copolymers into CNC using two separate preprocessed components, a direct blending approach successfully fabricated multifunctional (CNC/PLA)-based composite films with exceptional toughness and robust reversible structural colors. The simple and effective co-assembly approach significantly increased the toughness of flexible CNC/PEG-PLA composite films by 1044%, making them easier to handle and manipulate. Additionally, these composite films exhibit responsiveness and reversibility to various stimuli, including left-handed CPL, different backgrounds, viewing angles, and changes in environmental relative humidity. They demonstrated an 18 s redshift to reach equilibrium in water and recover to the origin within 20 min after water evaporation but dissolved in water after 24 h of soaking. The designed coding arrays store information in channels with reversible color variation responses for encoding/decoding and further translate information using the Caesar cipher for complex yet accessible multi-information storage and anti-counterfeiting with a considerable information capacity. The integration of water-insoluble, PLA-based polymers paves the way for future research, providing a novel and effective process for developing biodegradable (CNC/PLA)-based flexible chiral materials with multiple responsive and tunable structural colorations for optical devices, color sensors, information storage, and communication encryption security. The co-assembly strategy not only enhances material versatility but also promotes environmental sustainability.

3.5 References

[1] R. Lan, Q. Wang, C. Shen, R. Huang, J. Bao, Z. Zhang, L. Zhang, H. Yang, *Adv. Funct. Mater.* **2021**, *31*, 2106419.

[2] F. Bian, L. Sun, H. Chen, Y. Wang, L. Wang, L. Shang, Y. Zhao, *Adv. Sci.* **2022**, *9*, 2105278.

[3] Y. Shen, X. Le, Y. Wu, T. Chen, *Chem. Soc. Rev.* **2024**, *53*, 606.

[4] H. Huang, H. Li, X. Shen, K. Gu, J. Guo, C. Wang, *Chem. Eng. J.* **2022**, *429*, 132437.

[5] J. Fu, J. Feng, B. Shi, Y. Zhou, C. Xue, M. Zhang, Y. Qi, W. Wen, J. Wu, *Chem. Eng. J.* **2023**, *451*, 138240.

[6] Y. Jiang, J. Ma, Z. Ran, H. Zhong, D. Zhang, N. Hadjichristidis, *Angew. Chem. Int. Ed.* **2022**, *61*, e202208516.

[7] P. V. Braun, *Nature* **2011**, *472*, 423.

[8] J. Sun, B. Bhushan, J. Tong, *RSC Adv.* **2013**, *3*, 14862.

[9] Z. Y. Li, J. Wang, B. Y. Gu, *Phys. Rev. B* **1998**, *58*, 3721.

[10] B. Datta, E. F. Spero, F. J. Martin-Martinez, C. Ortiz, *Adv. Mater.* **2022**, *34*, 2100939.

[11] A. Narkevicius, R. M. Parker, J. Ferrer-Orri, T. G. Parton, Z. Lu, G. T. van de Kerkhof, B. Frka-Petesic, S. Vignolini, *Adv. Mater.* **2022**, *34*, 2203300.

[12] F. Marlow, Muldarisnur, P. Sharifi, R. Brinkmann, C. Mendive, *Angew. Chem. Int. Ed.* **2009**, *48*, 6212.

[13] C. Ji, M. Chen, L. Wu, *Adv. Opt. Mater.* **2022**, *10*, 2102383.

[14] W. Hong, Z. Yuan, X. Chen, *Small* **2020**, *16*, 1907626.

[15] L. Y. Li, D. Li, X. Dong, Q. W. Tan, X. L. Wang, Y. Z. Wang, F. Song, *Chem. Eng. J.* **2024**, *479*, 147669.

[16] Z. L. Wang, Z. P. Deng, F. Wang, X. L. Wang, Y. Z. Wang, F. Song, *Chem. Eng. J.* **2023**, *478*, 147364.

[17] K. Chung, S. Yu, C. J. Heo, J. W. Shim, S. M. Yang, M. G. Han, H. S. Lee, Y. Jin, S. Y. Lee, N. Park, J. H. Shin, *Adv. Mater.* **2012**, *24*, 2375.

[18] Y. Takeoka, *J. Mater. Chem.* **2012**, *22*, 23299.

[19] R. O. Prum, J. A. Cole, R. H. Torres, *J. Exp. Biol.* **2004**, *207*, 3999.

[20] J. D. Forster, H. Noh, S. F. Liew, V. Saranathan, C. F. Schreck, L. Yang, J. G. Park, R. O. Prum, S. G. J. Mochrie, C. S. O'Hern, H. Cao, E. R. Dufresne, *Adv. Mater.* **2010**, *22*, 2939.

[21] J. George, S. Sabapathi, *Nanotechnol. Sci. Appl.* **2015**, *8*, 45.

[22] R. M. Parker, G. Guidetti, C. A. Williams, T. Zhao, A. Narkevicius, S. Vignolini, B. Frka-Petesic, *Adv. Mater.* **2018**, *30*, 1704477.

[23] J. F. Revol, H. Bradford, J. Giasson, R. H. Marchessault, D. G. Gray, *Int. J. Biol. Macromol.* **1992**, *14*, 170.

[24] M. Xu, G. Li, W. Li, B. An, J. Sun, Z. Chen, H. Yu, J. Li, G. Yang, S. Liu, *Angew. Chem. Int. Ed.* **2022**, *61*.

[25] J. Shojaeiarani, D. S. Bajwa, S. Chanda, *Compos. Part C Open Access* **2021**, *5*, 100164.

[26] C. Xu, C. Huang, H. Huang, *Appl. Mater. Today* **2021**, *22*, 100912.
[27] Y. D. He, Z. L. Zhang, J. Xue, X. H. Wang, F. Song, X. L. Wang, L. L. Zhu, Y. Z. Wang, *ACS Appl. Mater. Interfaces* **2018**, *10*, 5805.
[28] L. Bai, Z. Wang, Y. He, F. Song, X. Wang, Y. Wang, *ACS Sustain. Chem. Eng.* **2020**, *8*, 18484.
[29] Z. Yu, K. Wang, X. Lu, *Int. J. Biol. Macromol.* **2021**, *188*, 385.
[30] K. Yao, Q. Meng, V. Bulone, Q. Zhou, *Adv. Mater.* **2017**, *29*, 1701323.
[31] Y. Qi, S. Wang, J. Sun, J. Song, H. Li, J. Guo, *I Int. J. Biol. Macromol.* **2024**, *260*, 129544.
[32] A. B. Ghazvini, B. Acharya, D. R. Korber, *Carbohydrate Polymers* **2022**, *275*, 118709.
[33] Y. Meng, Z. Long, Z. He, X. Fu, C. Dong, *Biomacromolecules* **2021**, *22*, 4479.
[34] J. Liao, C. Zhu, B. Gao, Z. Zhao, X. Liu, L. Tian, Y. Zeng, X. Zhou, Z. Xie, Z. Gu, *Adv. Funct. Mater.* **2019**, *29*, 1902954.
[35] Y. Huang, G. Chen, Q. Liang, Z. Yang, H. Shen, *Int. J. Biol. Macromol.* **2020**, *149*, 819.
[36] J. Zi, X. Yu, Y. Li, X. Hu, C. Xu, X. Wang, X. Liu, R. Fu, *Proc. Natl. Acad. Sci.* **2003**, *100*, 12576.
[37] J. M. Medina, J. A. Díaz, P. Vukusic, *Opt. Express, OE* **2015**, *23*, 10198.
[38] M. Kohri, *Sci. Technol. Adv. Mater.* **2020**, *21*, 833.
[39] R. Duan, M. Lu, R. Tang, Y. Guo, D. Zhao, *Biosensors* **2022**, *12*, 707.
[40] X. Dong, Z. L. Zhang, Y. Y. Zhao, D. Li, Z. L. Wang, C. Wang, F. Song, X. L. Wang, Y. Z. Wang, *Compos. B Eng.* **2022**, *229*, 109456.
[41] K. Madhavan Nampoothiri, N. R. Nair, R. P. John, *Bioresour. Technol.* **2010**, *101*, 8493.
[42] D. Viet, S. B. Candanedo, D. G. Gray, *Cellulose* **2007**, *14*, 109.
[43] E. Valkama, O. Haluska, V. P. Lehto, O. Korhonen, K. Pajula, *Int. J. Pharm.* **2021**, *606*, 120902.
[44] Q. Y. Cheng, C. S. Guan, M. Wang, Y. D. Li, J. B. Zeng, *Carbohydr. Polym.* **2018**, *199*, 390.
[45] J. Huang, S. Lyu, F. Fu, Y. Wu, S. Wang, *RSC Adv.* **2017**, *7*, 20152.
[46] H. Chang, J. Luo, A. A. Bakhtiary Davijani, A. T. Chien, P. H. Wang, H. C. Liu, S. Kumar, *ACS Appl. Mater. Interfaces* **2016**, *8*, 5768.
[47] M. He, Y.-I. Hsu, H. Uyama, *Appl. Mater. Today* **2024**, *36*, 102057.
[48] R. Z. Xiao, Z. W. Zeng, G. L. Zhou, J. J. Wang, F. Z. Li, A. M. Wang, *Int. J. Nanomedicine* **2010**, *5*, 1057.
[49] N. Roopsung, A. Sugawara, Y. I. Hsu, T. A. Asoh, H. Uyama, *Macromol. Rapid Commun.* **2023**, *44*, 2300205.
[50] P. Sukhavattanakul, H. Manuspiya, *Carbohydr. Polym.* **2020**, *230*, 115566.
[51] J. F. Young, *J. Appl. Chem.* **1967**, *17*, 241.
[52] L. Segal, J. J. Creely, A. E. Martin, C. M. Conrad, *Text. Res. J.*, **1959**, *29*, 786.
[53] H. Zhao, J. H. Kwak, Z. Conrad Zhang, H. M. Brown, B. W. Arey, J. E. Holladay, *Carbohydr. Polym.* **2007**, *68*, 235.

[54] H. Hasegawa, Y. Horikawa, T. Shikata, *Macromolecules* **2020**, *53*, 2677.
[55] C. Q. Pritchard, F. Navarro, M. Roman, M. J. Bortner, *J. Colloid Interface Sci.* **2021**, *603*, 450.
[56] L. Tang, B. Wang, S. Bai, B. Fan, L. Zhang, F. Wang, *Carbohydr. Polym.* **2024**, *324*, 121485.
[57] M. Y. Li, P. F. Yan, J. Liu, X. J. Zheng, K. Y. Tang, F. Wang, *Cellulose* **2022**, *29*, 1609.
[58] Z. Wang, Z. Yao, J. Zhou, Y. Zhang, *Carbohydr. Polym.* **2017**, *157*, 945.
[59] J. A. Sirviö, M. Visanko, O. Laitinen, A. Ämmälä, H. Liimatainen, *Carbohydr. Polym.* **2016**, *136*, 581.
[60] G. Xu, A. J. Onyianta, J.-C. Eloi, R. L. Harniman, J. Laverock, I. Bond, O. A. Diejomaoh, T. T. Koev, Y. Z. Khimyak, S. J. Eichhorn, *Biomacromolecules* **2024**, *25*, 715.
[61] T. Abitbol, E. Kloser, D. G. Gray, *Cellulose* **2013**, *20*, 785.
[62] F. Niu, M. Li, Q. Huang, X. Zhang, W. Pan, J. Yang, J. Li, *Carbohydr. Polym.* **2017**, *165*, 197.
[63] C. F. Castro-Guerrero, D. G. Gray, *Cellulose* **2014**, *21*, 2567.
[64] J. Q. Han, C. J. Zhou, Y. Q. Wu, F. Y. Liu, Q. L. Wu, *Biomacromolecules* **2013**, *14*, 1529.
[65] J. H. Jordan, M. W. Easson, B.e Dien, S. Thompson, B.D. Condon, *Cellulose* **2019**, *26*, 5959.
[66] Z. Ling, J. Chen, X. Y. Wang, L. P. Shao, C. Wang, S. Chen, J. Q. Guo, Q. Yong, *Carbohydr. Polym.* **2022**, *296*, 119920.
[67] N. Wang, E. Ding, R. Cheng, *Polymer* **2007**, *48*, 3486.
[68] H. de Vries, *Acta. Cryst.* **1951**, *4*, 219.
[69] J. Zhu, H. Sun, B. Yang, Y. Weng, *Materials (Basel)* **2024**, *17*, 336.
[70] S. A. Jin, R. J. Spontak, *Adv. Ind. Eng. Polym. Res.* **2023**, *6*, 356.
[71] L. J. Andrew, C. M. Walters, W. Y. Hamad, M. J. MacLachlan, *Biomacromolecules* **2023**, *24*, 896.
[72] R. O. Prum, R. Torres, C. Kovach, S. Williamson, S. M. Goodman, *J. Exp. Biol.* **1999**, *202*, 3507.
[73] M. Xu, W. Li, C. Ma, H. Yu, Y. Wu, Y. Wang, Z. Chen, J. Li, S. Liu, *J. Mater. Chem. C* **2018**, *6*, 5391.
[74] Y. Yuan, A. Martinez, B. Senyuk, M. Tasinkevych, I. I. Smalyukh, *Nat. Mater.* **2017**, *17*, 71.
[75] M. Sakai, T. Seki, Y. Takeoka, *Small* **2018**, *14*, 1800817.
[76] J. M. Kim, J. M. Bak, B. Lim, Y. J. Jung, B. C. Park, M. J. Park, J. M. Park, H. Lee, S. H. Jung, *Nanoscale* **2022**, *14*, 5377.
[77] A. Tran, C. E. Boott, M. J. MacLachlan, *Adv. Mater.* **2020**, *32*, 1905876.
[78] G. Mayonado, S. Mian, V. Robbiano, F. Cacialli, *BFY Proceedings* **2015**, pp. 60-63.
[79] C. M. Walters, C. E. Boott, T.-D. Nguyen, W. Y. Hamad, M. J. MacLachlan, *Biomacromolecules* **2020**, *21*, 1295.

[80] R. Xiong, S. Yu, M. J. Smith, J. Zhou, M. Krecker, L. Zhang, D. Nepal, T. J. Bunning, V. V. Tsukruk, *ACS Nano* **2019**, *13*, 9074.
[81] F. Zhang, Q. Li, C. Wang, D. Wang, M. Song, Z. Li, X. Xue, G. Zhang, G. Qing, *Adv. Funct. Mater.* **2022**, *32*, 2204487.
[82] R. Xue, H. Zhao, Z. W. An, W. Wu, Y. Jiang, P. Li, C. X. Huang, D. Shi, R. K. Y. Li, G.-H. Hu, S. F. Wang, *ACS Nano* **2023**, *17*, 5653.
[83] F. Zhang, W. Ge, C. Wang, X. Zheng, D. Wang, X. Zhang, X. Wang, X. Xue, G. Qing, *ACS Appl. Mater. Interfaces* **2021**, *13*, 17118.
[84] Y. Sui, X. Li, W. Chang, H. Wan, W. Li, F. Yang, Z. Z. Yu, *Carbohydr. Polym.* **2020**, *232*, 115778.
[85] K. Feng, C. Dong, Y. Gao, Z. Jin, *ACS Sustain. Chem. Eng.* **2021**, *9*, 6764.
[86] H. Wan, X. Li, L. Zhang, X. Li, P. Liu, Z. Jiang, Z. Z. Yu, *ACS Appl. Mater. Interfaces* **2018**, *10*, 5918.
[87] X. Zhang, R. Xiong, S. Kang, Y. Yang, V. V. Tsukruk, *ACS Nano* **2020**, *14*, 14675.
[88] Z. L. Zhang, X. Dong, Y. N. Fan, L. M. Yang, L. He, F. Song, X. L. Wang, Y. Z. Wang, *ACS Appl. Mater. Interfaces* **2020**, *12*, 46710.
[89] H. Bai, S. Hu, H. Zhu, S. Zhang, W. Wang, W. Dong, *Int. J. Biol. Macromol.* **2023**, *250*, 126132.
[90] Y. Zhang, Z. Tian, Y. Fu, Z. Wang, M. Qin, Z. Yuan, *Carbohydr. Polym.* **2020**, *228*, 115387.
[91] L. Shi, X. Liu, W. Wang, L. Jiang, S. Wang, *Adv. Mater.* **2019**, *31*, 1804187.
[92] Y. Meng, Z. He, C. Dong, Z. Long, *Carbohydr. Polym.* **2022**, *277*, 118756.
[93] G. Ozkoc, S. Kemaloglu, *J. Appl. Polym. Sci.* **2009**, *114*, 2481.
[94] M. He, Y.-I. Hsu, H. Uyama, *J. Hazard. Mater.* **2024**, *474*, 134819.

Concluding Remarks

In this study, functional films based on PEG-PLA multiblock copolymers were comprehensively developed and investigated. This dissertation aims to contribute high-performance biodegradable copolymers with advanced functionality and to explore their potential applications through facile and innovative design approaches.

In Chapter 1, mitigating marine plastic pollution demands superior marine-biodegradable plastics, a critical challenge as commercially available PLA biodegrades slowly in complex marine environments. This study presents an innovative bioplastic design, incorporating a hydrophilic PEG unit into PLA via facile ring-opening and coupling reactions to yield sequence-controlled alternating or random PEG-PLA copolymers. These materials exhibit exceptional freshwater durability, impressive wet and dry mechanical properties, and rapid biodegradation in proteinase K solutions and seawater. PEG-PLA bioplastics show the ability to withstand DIW yet rapidly biodegrade in seawater, making them promising candidates for preventing marine plastic pollution.

In Chapter 2, a versatile SMBS capable of delivering multifunctionalities was proposed. This SMBS, utilizing a PLA-based physically crosslinked network programmed into specific shapes, can be efficiently prepared via a rapid two-step strategy. It exhibits excellent dual-SME triggered by body temperature and water. It allows the potential fabrication of on-demand synchronous shape memory and drug-release functional systems for esophageal stenosis therapy. The results demonstrate that the proposed SMBS holds substantial promise for biomedical applications.

In Chapter 3, sustainable chiral nematic CNC composite materials were fabricated for the first time by incorporating a water-insoluble poly(L-lactide) (PLA)-based biodegradable copolymer into CNCs. To achieve this desirable material, I adopted a directly efficient blending strategy of two separate preprocessed components. The as-prepared films exhibited a significant 1044% improvement in toughness while maintaining robust responses to left-handed CPL, different backgrounds and viewing angles, and varying relative humidity. They also showed rapidly reversible redshift/blueshift with water absorption and evaporation but dissolved in water after 24 h soaking. Notably, they demonstrated that coding arrays store information in

channels with reversible color change responses for encoding/decoding and further translate information using the Caesar cipher for complex yet accessible information transfer. Given the increasing demand for information security and environmental sustainability, the novel (CNC/PLA)-based chiral composite films pave the way for sophisticated, yet convenient, information encryption and decryption applications and offer a valuable contribution to chemical engineering and material science.

List of Publications

1. Superior sequence-controlled poly(L-lactide)-based bioplastic with tunable seawater biodegradation

Manjie He, Yu-I Hsu*, Hiroshi Uyama*

Journal of Hazardous Materials, **2024**, *474*, 134819.

DOI: 10.1016/j.jhazmat.2024.134819

2. Design of Novel Poly(L-lactide)-based Shape Memory Multiblock Copolymers for Biodegradable Esophageal Stent Application

Manjie He, Yu-I Hsu*, Hiroshi Uyama*

Applied Materials Today, **2024**, *36,* 102057.

DOI: 10.1016/j.apmt.2024.102057

3. High-performance Bioinspired Multi-Responsive Chiral Cellulose Nanocrystals-based Flexible Films for Information Encryption

Manjie He, Yu-I Hsu*, Hiroshi Uyama*

Chemical Engineering Journal, **2024**, *495*, 153516.

DOI: 10.1016/j.cej.2024.153516

Acknowledgments

This study was conducted in the Uyama Laboratory, Department of Applied Chemistry, Graduate School of Engineering, Osaka University, from 2021 to 2024. I am grateful to Osaka University and the Japan Science and Technology Agency (JST) for their financial support, which enabled me to pursue my research and studies at Osaka University. Throughout my Ph.D. journey over these three years, I have been fortunate to receive invaluable assistance from numerous individuals, whose guidance and advice were integral to completing this thesis. I express my heartfelt gratitude to all those who supported me unwaveringly.

I would like to extend my deepest gratitude to my supervisor, Prof. Hiroshi Uyama of Osaka University, for his trust in me and for admitting me to his laboratory as a doctoral student from 2021 to 2024. This research would not have been possible without his expertise, constructive criticism, and guidance. His always support and countless opportunities have helped me grow as a researcher.

I am deeply grateful to the rest of my dissertation committee: Prof. Akinori Saeki and Prof. Norimitsu Tohnai, for their insightful comments and valuable time during the preparation and writing of this dissertation.

I sincerely thank Associate Prof. Yu-I Hsu for her invaluable advice and support throughout my research, manuscript, and dissertation writing. Her expertise in experimental design has been instrumental in facilitating my transition into a new experimental environment, thus ensuring the smooth progress of my research.

I am particularly grateful to Assistant Prof. Akihide Sugawara for his insightful suggestions and assistance with my research.

I would like to thank the past and present staff of the Uyama Laboratory: Yoko Uenishi, Tomoko Shimizu, Chiko Abe, Kyoko Tanimura, Erina Katsuragawa, Kyoko Fukuma, and Yagi Rieko for their enthusiastic support in laboratory matters and their kind help in my daily life, allowing me to conduct my research more effectively.

I would like to thank all the students of Uyama Lab. From 2021 and 2024 for hearty support and kind assistance in research and daily life. Exclusively, I would like to thank to: Dr. Naharullah Bin Jamaluddin, Dr. Yankun Jia, Dr. Raghav Soni, Dr. Hanyu Wen, Dr. Yanting

Lyu, Dr. Yan Wang, Dr. Luwei Zhang, Dr. Meng Wei, Dr. Mark Adam Malaluan Ferry, Dr. Roopsung Nontarin, Dr. Yuxiang Jia, Madhurangika Panchabashini Horathal Pedige, Emil Hajili, Kazuki Shibasaki, Yu Cao, Peng Du, Juan Wang, May Myat Noe, Hasinah Binti Mohamed Rafiq, Judit Rebeka Molnár, Guan Wang, Ying Yao, Ruiqi Zhang, Yihan Gao, Atsuki Takagi, Izzah Durrati Binti Haji Abdul, Sooyeon Noh, Yazhou Su, Kai Cheng, Jiahui Dong, Qianying Li, Yi-ho Chen, Yuka Kashihara, Yuji Kiba, Takeshi Hiraoka, Yuki Shioji, Atsushi Koizumi, Motoi Oda, Kaita Kikuchi, Koki Tsujita, Hajime Fujimori, Suzune Miki, Thuy Le Huynh An, , Xinyu Lou, Hiroshi Hasagawa, Shotaro Yano, Kippei Yamamura, Rika Onishi, Hajah Wafiqah Binti Haji Daim, Ziyu Meng, Shafinee Yarnina Hj Md Shafri, Alejandro Adrian Ayala Escamilla, Daniela Yacine Sebastião Bravo Da Costa, Siti Nur Asyifa Nazihan Andey Asmara, Yuka Asai, Yinxiang Shen, Moe Kominami, Akane Odagaki, Rina Kugimiya, Shunya Kubo, Sota Nakagawa, Maoko Hayashi, Shunsuke Kondo, Yudai Ioku, Naoaki Ishihara, Yuta Okuda, Kanoko Sakai, and Takehiro Masuda, Kohnosuke Yoshida, Siaw Thong Chua, Peixuan Shao, Chenxu Zhang, Akari Ito, Yuto Kirihata, Yuyo Shibamto, Taiga Hamabe, Chiho Yamaji.

Finally, I deeply thank my family and friends for their companionship, encouragement and always standing by me.

HE MANJIE

July 2024

Suita, Osaka, Japan